



universität
wien

DISSERTATION

Titel der Dissertation

„Fatigue investigations of miniaturized and bulk Al-Cu
bond interfaces“

Verfasserin

Mag. Alice Lassnig

angestrebter akademischer Grad

Doktorin der Naturwissenschaften (Dr. rer. Nat.)

Wien, 2015

Studienkennzahl lt. Studienblatt: A 791 411

Dissertationsgebiet lt. Studienblatt: Physik

Betreuerin / Betreuer: Ao. Univ.-Prof. Dr. Michael Zehetbauer & Dr. Golta Khatibi

*“An expert is a person who has made all the mistakes that can be made
in a very narrow field.”*

Niels Bohr, Danish Physicist 1885 – 1962

Abstract

In microelectronics, miniaturized Cu-Al ball bonds serve as link between integrated circuits and outside circuitry. During service, these bonds are subjected to mechanical, thermal and electrical stresses. Moreover, such devices are exposed to elevated service temperatures leading to the formation of brittle intermetallic compounds (IMCs) at the interface between Cu and Al layers. Currently, the quality of such bonds is assessed by standardized, static ball shear tests, which do not reveal the bond performance under cyclic loading conditions.

As it was the aim of the present thesis to study the mechanical fatigue behavior of Cu-Al joints in microelectronic devices produced by solid state bonding techniques, a novel fatigue test technique was created to adapt to this miniaturized bond geometry. This allowed not only to obtain reliable fatigue life curves but also to study the influence of different microstructural states of the bond interface. Detailed fracture surface analyses showed the characteristic fracture morphologies to depend on the microstructural evolution of the IMC layers, too. While the standardized static shear tests revealed no significant decrease of the bond shear force with increased formation of the intermetallic phases, the fatigue tests proved a clear degradation in the cyclic strength.

In order to separate the influences of the loading condition and of the IMCs to the resulting fatigue behavior, a complementary study was conducted on bulk, model diffusion pairs. Here a special setup was designed which allowed to apply different well-defined mode I and mode II loading conditions.

In both the microscopic as well as the macroscopic studies the fatigue crack always initiates in the Al layer, as has been also observed with in-situ TEM investigations. When interfacial IMCs are present, the crack is deflected into the most brittle one, leading to early failure and lower fatigue lives. Furthermore, it has been shown that particularly under pronounced shear loading, an early failure of the microelectronic devices has to be expected.

Zusammenfassung

In der Mikroelektronik dienen miniaturisierte Cu-Al Ball-Bond-Verbindungen zur Kontaktierung integrierter Schaltkreise. Diese werden im Betrieb nicht nur mechanischen, thermischen sowie elektrischen Spannungen, sondern auch erhöhten Temperaturen ausgesetzt, welche zur Bildung spröder intermetallischer Phasen an der Grenzfläche zwischen Cu und Al Schichten führen. Zurzeit wird die Qualität dieser Bond-Verbindungen mittels standardisierter statischer Ball-Scher-Tests erfasst, welche aber keine Rückschlüsse auf die zyklische Belastbarkeit dieser Bond-Verbindungen zulassen.

Indem es das Ziel der vorliegenden Dissertation war, das mechanische Ermüdungsverhalten von Cu-Al Bondverbindungen in mikroelektronischen Bauteilen zu untersuchen, wurde eine neue Ermüdungsmethode zum Test derartiger Verbindungen entwickelt. Dadurch war es möglich, nicht nur verlässliche Ermüdungskurven zu gewinnen, sondern auch den Einfluss unterschiedlicher Mikrozustände der Bond-Verbindung zu studieren. Detaillierte Analysen der Ermüdungsbruchflächen zeigten charakteristische Bruchflächen-Morphologien, die ebenfalls von der mikrostrukturellen Entwicklung der intermetallischen Schichten abhängen. Während die standardisierten statischen Schertests keine signifikante Abnahme der Scherkraft mit fortschreitender Ausbildung der intermetallischen Phasen zeigten, bewiesen die Ermüdungsversuche eine eindeutige Abnahme der zyklischen Festigkeit.

Um die Einflüsse des Belastungsmodus und der intermetallischen Phasenbildung auf die Ermüdungsfestigkeit zu separieren, wurden ergänzende Untersuchungen an makroskopischen Modelldiffusionsproben durchgeführt. Hierbei wurde ein spezieller Aufbau gewählt, der es erlaubte, wohldefinierte verschiedene Kombinationen der Belastungsmoden I und II zu realisieren.

Es konnte u.a. auch mittels in-situ TEM-Untersuchungen gezeigt werden, dass die Rissinitiierung in der Al-Schicht erfolgt, gleichgültig ob es sich dabei um die mikroskopischen oder die makroskopischen Proben handelt. Liegen intermetallische Phasen in der Materialverbindung vor, wird der Riss in diese Phase abgelenkt, was zu früherem Bruch bzw. Verminderung der Lebensdauer führt. Außerdem wurde gezeigt, dass insbesondere bei ausgeprägter Scherbelastung mit einem verfrühten Ausfall der Bauteile zu rechnen ist.

Contents

1	Motivation and scope of this work	1
1.1	Presentation of the problem	1
1.2	Aim of the thesis	2
1.3	Structure of this work	3
2	Introduction	5
2.1	Deformation of metals	5
2.1.1	Static deformation of solids – uniaxial tensile test	6
2.1.2	Yielding and fracture under combined stresses	9
2.2	Fatigue of metals	12
2.2.1	Fatigue: definition and early research	12
2.2.2	Basic concepts of fatigue of materials	13
2.2.3	Implications of fracture mechanics on fatigue	16
2.2.4	Overview of fatigue mechanisms	19
2.3	Thermosonic ball bonds in microelectronic devices	21
2.3.1	Thermosonic ball bonding process	22
2.3.2	Mechanisms of thermosonic ball bond process	23
2.3.3	Microstructural evolution of Al-Cu ball bonds	24
2.3.4	State of the art test methods for ball bond interface	26
2.4	Ultrasonic fatigue testing of materials	28
2.4.1	Principles of ultrasonic resonance fatigue testing	29
2.4.2	Ultrasonic fatigue testing of miniaturized bond interfaces	30
3	Mechanical fatigue of miniaturized Cu-based ball bonds	33
3.1	Investigated Cu-Al ball bond specimen	34
3.2	Development of accelerated fatigue tests for miniaturized ball bonds	34
3.2.1	Single bond testing	37
3.2.2	Multiple bond testing	38
3.2.3	Comparison of accelerated fatigue test techniques for Cu-Al ball bonds	45
3.2.4	Finite element (FE) analyses of MR1 –MR4	50
3.3	Growth kinetics of intermetallic compound formation	55
3.4	Effect of microstructural evolution on high cycle fatigue of Al-Cu bonds	57
3.4.1	Microstructural evolution of Al-Cu ball bond	57

Contents

3.4.2	Fatigue results	61
3.4.3	Fatigue fracture morphology	62
3.5	High cycle fatigue behavior of Al-Cu vs. Cu-Cu ball bond interfaces	68
3.6	Summary	69
4	High cycle fatigue of bulk Al-Cu interfaces	73
4.1	Diffusion bonding of bulk Al-Cu couples	73
4.1.1	Influence of process parameters on diffusion bonded specimens	74
4.1.2	Summary of preliminary diffusion bond experiments	84
4.1.3	Characterization of diffusion bonded fatigue specimen	84
4.1.4	Heat treatments of diffusion bond interface	90
4.2	Ultrasonic fatigue testing of bulk Al-Cu interfaces	93
4.3	Influence of loading mode on the fatigue behavior of bulk Al-Cu bonds	96
4.3.1	Fractographic observations	99
4.4	Role of aluminum on the fatigue behavior of bulk Al-Cu bonds . . .	103
4.5	Summary	105
5	In-situ TEM fatigue test of Al-Al ₂ Cu interface	111
5.1	Specimen design	112
5.2	In-situ fatigue experiment	116
5.2.1	Stage i – reversible (elastic) cyclic loading	118
5.2.2	Stage ii-crack initiation and slow crack propagation	120
5.2.3	Stage iii: Slow crack growth	123
5.2.4	Stage iv & Stage v: Rapid crack growth and catastrophic failure	125
5.3	Summary	126
6	General summary and conclusion	131
7	Outlook	135
	Acknowledgments	137
	Bibliography	139

1 Motivation and scope of this work

1.1 Presentation of the problem

Fatigue of materials and engineering components has been of scientific interest for more than a century. While various materials have been investigated systematically in the past decades, it is still crucial to study the fatigue behavior of the material of interest since lifetime is not only dictated by the intrinsic material properties but also by external factors such as the geometry, microstructure, testing setup and environment.

In the present thesis the aim is to study the fatigue behavior of copper–aluminum bond interfaces. Copper and aluminum became a prevailing materials combination in various technological applications due to their lightweight, excellent thermal and electrical properties. Bimetallic joints, however, generally represent weakest sites in technological devices as the bond interface has to compensate the difference of physical properties of the bonded materials. The most illustrative example is the difference of the coefficient of thermal expansion, where external heating induces shear stresses at the interface due to the individual dilatation behavior of both materials.

The above mentioned Al-Cu combination is also deployed in the microelectronics sector. Here, microjoints are primarily made of this materials combination connecting integrated circuits to their outside circuitry. A predominant microjoint type, which is of main interest in this study, are so-called thermosonic ball bonds, which are mainly used in microelectronic devices for high current applications e.g. in the automotive sector. Recently, Al-Cu thermosonic ball bonds have become a standard technology replacing the formerly used Al-Au ball bonds.

Currently, the reliability of such bonds is assessed by standardized, static destructive ball shear and wire pull tests. During service, such interconnects are exposed to thermal fluctuations and mechanical vibrations, leading to cyclic stresses at the bond interface. Above mentioned standard static tests, however, do not reflect

the bond performance under cyclic load conditions and thus, their mechanical fatigue behavior is still unknown. In addition, these interconnects are subjected to elevated service temperatures fostering interdiffusion of both materials into each other, which leads to the formation of intermetallic compounds at the bond interface. These intermetallic compounds (IMC) highly differ in their physical properties from the soft and ductile parent materials leading to an overall bond degradation and decrease of lifetime, because an embrittlement of the bond is expected. Currently, there is a variety of studies, where the static mechanical properties of such intermetallic compounds were characterized. Also, some researchers have been working on the study of the static fracture behavior of Al-Cu interfaces with intermetallic compounds. However, the fatigue behavior of this Al-Cu multilayer material including several intermetallic compounds is yet still unknown.

1.2 Aim of the thesis

The aim of this present thesis is to study the mechanical fatigue properties of the miniaturized Al-Cu interfaces occurring in thermosonic wire bonds in microelectronic devices compared to their well-known static mechanical properties. For this purpose, an industrially applicable accelerated test technique capable to assess the mechanical fatigue properties of such miniaturized bond interfaces is specially developed. Moreover, special emphasis is set on the role of intermetallic compounds evolution to analyze the mechanical properties of the bond interface.

Due to the complex geometry of these miniaturized interconnects a further aim is to study the fatigue behavior of the same material composition on a lengthscale, where the specimens are easy to handle and where well-defined loading conditions can be applied. Therefore, massive Al-Cu diffusion bonds mimicking the microstructure of highly aged miniaturized ball bond interface with the same intermetallic compounds were created allowing to study their fatigue behavior under controlled loading combinations of mode I (tension-compression) and mode II (shear). Here, the aim is to reveal the fatigue behavior as a function of the applied loading condition to further understand, which loads are detrimental for this material combination and to further study the impact of the brittle intermetallic compounds.

As a last step, to understand the crack propagation and deflection processes towards the intermetallic compound a TEM in-situ fatigue study of the Al-Al₂Cu interface,

which has shown a significant importance in the fatigue crack propagation process of previous experiments, is conducted on a pre-notched electrontransparent lamella.

1.3 Structure of this work

To tackle the above described problems, the present work is structured as follows:

The first chapter 2 gives an introductory overview providing a basic theoretical background necessary to understand the work and approach in this thesis.

The experimental work and results of this thesis are presented in the chapters 3, 4 and 5.

Chapter 3 is dedicated to the mechanical properties of the thermosonic Al-Cu ball bond interfaces, where the main focus is set on their high cycle fatigue behavior. After a detailed description of the investigated ball bond specimen in section 3.1, the development of industrially applicable fatigue test techniques to allow further fatigue investigations is presented in section 3.2, where it can be distinguished between single bond and multiple bond test techniques. The proposed test methods are compared and discussed in section 3.2.3. The occurring stress states depending on the chosen fatigue test setup are explained by means of finite element analyses (FEA) in section 3.2.4. In section 3.4 the role of intermetallic compounds formation on the high cycle fatigue behavior of miniaturized Al-Cu ball bond interface is investigated on three selected microstructural states: (i) the as-bonded state, (ii) an intermediately annealed state obtained by a thermal treatment at 200 °C and 200 h and (iii) a highly aged state after 200 °C 2000 h. In the last section 3.5, the fatigue behavior Cu-Cu ball bonds is compared to the previously investigated Al-Cu bonds.

In chapter 4 the high cycle fatigue behavior of bulk Al-Cu bond interfaces is studied, where the aim is to create defined combinations of mode I (tensile) and mode II (in-plane shear) loading modes to reveal the impact of the chosen loading mode on the fatigue performance of the present material combination. In the first part of this chapter a detailed description of the preparation of the bulk diffusion bonds is given.

In section 4.1 the parameters influencing the diffusion bond quality such as surface condition, temperature, applied pressure and process duration are discussed. A de-

tailed characterization of the bond interface used for the fatigue tests is presented in section 4.1.3. In section 4.2 the fatigue testing setup for bulk diffusion-bonded Al-Cu interfaces is explained, followed by a discussion of the obtained results in sections 4.3, 4.3.1, 4.4 .

As a last step a TEM in-situ fatigue study was conducted on a selected material interface, which was found to be responsible for the crack initiation and propagation in the investigated Al-Cu material system in chapter 5. This fatigue study is conducted on the pre-notched Al-Al₂Cu interface and observed in-situ by transmission electron microscopy (TEM) in order to demonstrate the crack initiation and propagation mechanisms in this material system.

Finally, the obtained results and conclusions are summarized and discussed in chapter 6.

2 Introduction

This introductory chapter provides a theoretical framework and builds the basis for the experimental approach described in the following chapters. In section 2.1, a brief overview of the deformation behavior of solids under static loading is given, where primarily metals are discussed. In section 2.2 main emphasis is set on the fatigue of materials, when subjected to cyclic loadings. The second part of this chapter is dedicated to Al–Cu interfaces created by solid-solid joining techniques. Main emphasis is set on miniaturized bond interconnects, occurring in microelectronic devices – so-called thermosonic ball bonds (see section 2.3). Main emphasis is set on the formation and growth of intermetallic compounds (IMC) at their bimetallic interface due to high thermal exposure during service. Their physical properties and impact on the bond reliability are discussed. The last part of this section briefly explains the standard test techniques, which reveal static material properties of the ball-bonded interconnects.

In the last section of this chapter in 2.4 the principles of ultrasonic fatigue testing of materials is explained. Finally, a novel accelerated fatigue test technique adapted to miniaturized interconnects in microelectronic applications is presented to reveal their mechanical fatigue properties in reasonable time.

2.1 Deformation of metals

In the following section basic aspects on the deformation behavior of a solid subjected to external (static) loads are presented. Unlike liquids or gases, an externally loaded solid features an inner resistance towards a change of its initial shape. The deformed solid remains coherent and does not fragment into pieces in the elastic regime. First, the static deformation of a solid are briefly discussed in section 2.1.1. In the second part most widely employed yield criteria for solids subjected to multi-axial loads are presented in 2.1.2. In section 2.2 a more detailed description of the mechanisms occurring in a solid subjected to cyclic loads is presented.

2.1.1 Static deformation of solids – uniaxial tensile test

The static deformation behavior of a solid subjected to an external load is discussed on the basis of the uniaxial tensile test. This test is a standard method [AST, 2015] to assess the mechanical properties of a solid subjected to a tensile force. Typically, the obtained data is plotted as a stress-strain curve as shown in Fig. 2.1, which reflects the mechanical properties of the investigated material. Usually, the nominal stress (see equation 2.1, that is the stress relative to the original specimen dimensions) is used in lieu of the real stress, which takes into account the geometric changes of the specimen. Here, only the nominal (engineering) stress – strain curve will be discussed. With σ being the stress acting on the specimen and ϵ describing the resulting deformation (strain) the material undergoes during the test.

$$\sigma = \frac{F}{A_0} \quad (2.1)$$

with F denoting the tensile force acting on the specimen and A_0 being the initial cross section of the tensile test specimen, measured prior the tensile experiment. The resulting strain ϵ describes the tensile deformation of the specimen (see equation 2.2).

$$\epsilon = \frac{l}{l_0} \cdot 100\% \quad (2.2)$$

where l is the elongated dimension and l_0 is the initial length of the specimen. The stress–strain curve in Fig. 2.1 can be roughly subdivided into two regions: In the first segment, stress and strain are likewise proportional to each other, which is denoted as the linear elastic, reversible regime. Beyond the yield stress denoting the onset of yielding, irreversible deformation is expected, is called the plastic regime. An important property resulting from the tensile test is the ultimate tensile stress σ_{UTS} , which is the highest stress amount reached prior to fracture corresponding to the maximum of the engineering stress–strain curve. In brittle materials this value coincides with the point of fracture.

Elastic deformation

The elastic deformation is typically associated with reversible “spring-like” stretching of the atomic bonds and is a reversible deformation mode. Thus, a stress relaxation leads to the original shape of the solid. The proportionality between

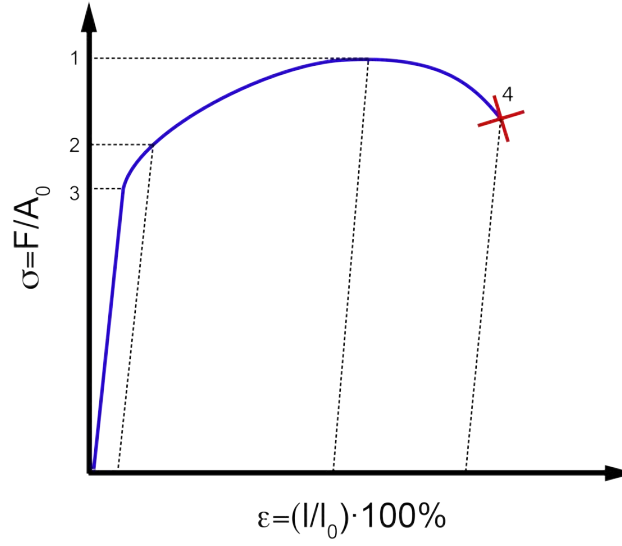


Figure 2.1: Tensile test curve: nominal stress $\sigma = F/a_0$ as a function of the strain $\epsilon = \frac{l}{l_0} \cdot 100\%$: 1: ultimate tensile stress σ_{UTS} , 2: yield stress at a plastic strain of 0.2%, 3: proportional limit stress, 4: fracture of the specimen.

stress and strain is described by Hooke's law in the following equation equ:Hooke (see e.g. Ref. [Gottstein, 2014], [Dowling, 1999] for further details).

$$\text{tensile loading: } \frac{F_{\perp}}{A_0} = E \frac{\Delta l}{l_0} \text{ or } \sigma = E \cdot \epsilon \quad (2.3)$$

where F_{\perp} is a tensile force perpendicular to the cross section A_0 of the sample and equals the tensile stress σ . The applied load leads to a change of the length of the specimen $l = l_0 + \Delta l$; the ratio between the length of the specimen which is described as resulting strain ϵ . The proportionality constant E is the Young's modulus or the elastic modulus. Its value depends on the mechanical properties of the material. In practice, it is sometimes not straightforward to determine the sharp transition between the elastic and plastic transition. Thus, by default the yield strength σ_y defining the onset of yielding is defined as the stress amount resulting in 0.2% strain, beyond which plasticity occurs. In the case of shear loading, where the applied force acts parallel to the solid's cross section F_{\parallel} an analogous relationship between shear stress τ and shear strain γ exists, where the shear modulus G is the

proportionality constant according to the following equation:

$$\text{shear loading: } \frac{F_{\parallel}}{A_0} = G \frac{\Delta x}{d} \text{ or } \tau = G \cdot \gamma \quad (2.4)$$

Typical values for the Young's and shear moduli for aluminum are $E_{Al} = 70GPa$ and $G_{Al} = 25.5GPa$, respectively. For copper the values are $E_{Cu} = 120GPa$ and $G_{Cu} = 44.7GPa$, [Crandall et al., 1978]. As a general rule of thumb, it can be considered for metals that the value of the shear modulus roughly corresponds to one third of the value of the Young's modulus.

Plastic deformation

When the solid is loaded at stresses beyond the yield stress the resulting strain is composed of an elastic, reversible and an irreversible, plastic amount. After unloading the material, the elastic strain vanishes and the plastic strain remains permanently. This irreversible deformation called plasticity can be described as gliding of atomic planes against each other, whilst the original crystal structure is maintained. Whereas elastic deformation is a homogeneous process across the solid leading to simultaneous stretching of the bonds, plastic deformation is associated to an inhomogeneous process, where atomic gliding occurs stepwise. Linear defects of the crystal lattice called dislocations are responsible for the motion of atomic planes. Dislocations can be subdivided into two main dislocation types: edge dislocations and screw dislocations. The edge dislocation can be imagined as a half inserted plane, which moves across the lattice. Its Burgers vector \vec{b} is perpendicular to the dislocation line (i.e. parallel to the propagation direction) and the resulting deformation is a so-called slip-step. The screw dislocation can be visualized as a crystal cut along a plane followed by a distortion of both detached parts against each other. Here a helical path can be drawn around this defect. The Burgers vector \vec{b} of this dislocation type points perpendicular to the dislocation line. Furthermore, mixed dislocation types and partial dislocations shall be mentioned but will not be treated further in this thesis. For further reading about dislocations the reader is advised to consult e.g. [Hull et al., 2011]. The most basic aspects of plastic deformation are elucidated hereafter according to [Gottstein, 2014] and [Dowling, 1999]: To maintain the crystal structure of a crystal while external deformation of its shape occurs, shape changes are solely possible by shearing entire

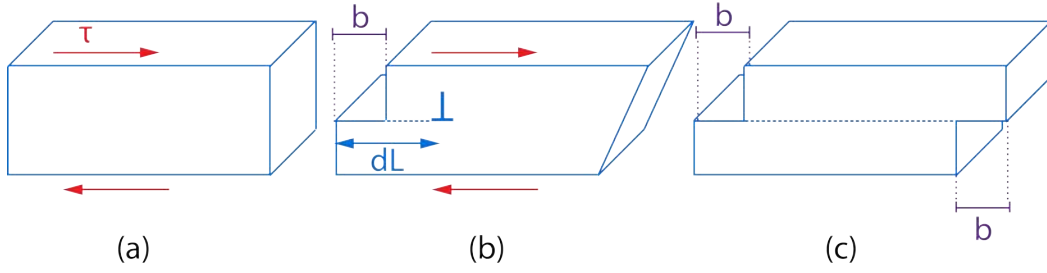


Figure 2.2: Schematic representation of plastic deformation in a crystal due to dislocation motion resulting in subsequent slip step (c). Redrawn and slightly modified after [Gottstein, 2014].

atomic planes. Therefore a theoretical critical shear stress τ_{th} necessary to shear two atomic planes against each other is required, which needs to overcome the atomic bonds:

$$\tau_{th} = \tau_{max} \cdot \sin \frac{2\pi x}{b} \simeq \tau_{max} \cdot \frac{2\pi x}{b} \quad (2.5)$$

where the value of the shear stress depends on the actual position x relative to the bond. τ_{max} corresponds to the maximum shear stress, which needs to be overcome when the atomic planes are approximately shifted one half atomic distance against each other. Since small displacements occur τ_{th} in equation 2.5 shall be in agreement with Hooke's law for shear deformation in equation 2.4. For metals the theoretical critical shear strength using characteristic inter-atomic potentials results τ_{th} reaches values around 1.4 GPa, whereas the experimentally obtained yield stress of copper single crystals are around 0.5 GPa. In the case of aluminum the ratio between τ_{exp}/τ_{th} is approximately $8.7 \cdot 10^{-4}$ [Gottstein, 2014]. To explain this discrepancy between theory and experiment, above mentioned linear defects were introduced to explain why plasticity is facilitated. Plastic deformation can be visualized by stepwise movement of the atomic planes, compared to the motion of a caterpillar, where only few parts are moved at a time. In Fig. 2.2 the deformation of a crystal due to dislocation motion is depicted. A shear stress results in gliding of two atomic planes – usually the highest packed plane – leading to irreversible slip step once the dislocation has passed the crystal [Dowling, 1999].

2.1.2 Yielding and fracture under combined stresses

Above described uniaxial tensile test is a standard laboratory test procedure and usually does not reflect the complex stress states a solid undergoes in real life e.g. as a component in engineering applications. Typically, load conditions such as tension, compression, bending, torsion, pressure, or a combination of these may act on a structural component. Therefore, it is useful to introduce a multiaxial failure criterion, which allows to calculate an equivalent tensile stress ρ [Pook, 2007]. Thus, these criteria simplify the complex stress state problem and replace it by a well-known loading scenario (e.g. the uniaxial tensile test).

While for ductile materials it is useful to introduce a condition defining its onset of yielding, which is the transition from purely elastic to plastic behavior, one has to bear in mind that for a perfectly brittle material catastrophic fracture may occur without yielding i.e. without permanent plastic deformation.

The most implemented theories employed for ductile engineering materials are the theories of Tresca and von Mises, which were first published in [Tresca, 1864] and [von Mises, 1913], respectively. For brittle materials it was found that the Rankine criterion is more successful (see Ref. [Rankine, 1857]). These three criteria are briefly explained in the following section. It should be noted, however, that almost infinite failure criteria can be defined.

Tresca criterion – Maximum shear stress yield theory

The Tresca criterion states that yielding of a material takes place when the difference of two principal stresses σ_1 and σ_3 acting on a piece of material equals a stress amount leading to yield of the material. (Annotation: General stresses acting on a solid are typically expressed by Cauchy's stress tensor σ_{ij} . By means of a coordinate transformation, this tensor can be diagonalized, revealing the principal stresses in the trace of the tensor. For further informations see introductory fracture mechanics literature e. g. Ref. [Anderson, 2005]).

Therefore the equivalent stress equals the yield stress of the material and can be expressed by the following equation:

$$\sigma_1 - \sigma_3 = \sigma_y = \sigma_{eq_Tresca} \quad (2.6)$$

where σ_y corresponds to the yield stress and $\sigma_{eq-Tresca}$ is the equivalent stress expressed.

Von Mises criterion – Maximum distortional energy yield theory

The von Mises criterion states that yield will occur when the maximum distortional energy is reached. In terms of principle stresses σ_1 , σ_2 , σ_3 the von Mises yield criterion can be expressed as:

$$\sigma_y = \sqrt{(\sigma_1^2 + \sigma_2^2 + \sigma_3^2 - \sigma_1\sigma_2 - \sigma_2\sigma_3 - \sigma_1\sigma_3)} \quad (2.7)$$

The von Mises yield criterion in Cartesian coordinates is expressed by equation 2.8.

$$\sigma_{eq-vonMises} = \sqrt{\frac{(\sigma_x - \sigma_y)^2 + (\sigma_y - \sigma_z)^2 + (\sigma_z - \sigma_x)^2}{2} + 3 \cdot (\tau_{xy}^2 + \tau_{yz}^2 + \tau_{xz}^2)} \quad (2.8)$$

where σ_i denote the normal stresses and τ_{ij} are the shear stresses acting on the planes of a material element, respectively. In a biaxial stress state several stress components equal zero, leading to the simplified von Mises equivalent stress, where only one tensile (normal) stress component and one shear component occur:

$$\sigma_{eq} = \sqrt{\sigma_y^2 + 3 \cdot \tau_{xy}^2} \quad (2.9)$$

(for plane stress, where σ_z is zero).

It has to be noted however, that the von Mises yield criterion is mainly valid for ductile, isotropic materials, featuring similar behavior under tension and under compression.

The Tresca and the von Mises criteria only slightly differ from each other, since their approaches both base on critical shear stresses acting on a body. However, the Tresca criterion is more conservative than the von Mises criterion.

Rankine criterion - Maximum normal stress criterion

In the case of brittle materials yielding does not necessarily occur. A perfectly brittle material is characterized by immediate fracture in the linear-elastic regime. For this class of materials, the most reasonable predictions for “yield” (in this case: fracture) are given by the maximum normal stress criterion, also known as Rankine criterion [Fenner, 1999]. The model of the fracture behavior of brittle materials assumes that they contain randomly oriented microscopic cracks. Hence, applied stresses normal to those flaws cause them to grow. In compression, these flaws are held together leading to a retardation of the crack growth and subsequently these materials are less sensitive to compression than to tension. For the two dimensional state, the Rankine criterion expressed in Cartesian coordinates is:

$$\sigma_{eq-Rankine} = \frac{1}{2}(\sigma_x - \sigma_y) + \frac{1}{2}\sqrt{(\sigma_x - \sigma_y)^2 + 4\tau_{xy}^2} \quad (2.10)$$

This yield criterion is widely used in applied geomechanics, where for example the fracture of rocks is studied (see e.g. Ref. [Saksala, 2010]).

2.2 Fatigue of metals

2.2.1 Fatigue: definition and early research

Fatigue in materials science and akin disciplines refers to the weakening and degradation of a solid exposed to cyclic loads. The nominal, maximum stress values causing such damage may be much less than the (static) strength of the material i.e. below the ultimate tensile stress limit or even below the yield stress limit.

Historically, this phenomenon is well-known since the mid of the 19th century. As a consequence of the Industrial Revolution, metal working became more adapted and structural engineering evolved rapidly in the Western world. Engineering disasters such as the rail accident in Versailles in 1842 became key events associated to material failure due to cyclic loading of engineering components, which initiated the systematic research into fatigue of metals and materials in general [Suresh, 1991]. Some pioneers in early fatigue research were the metallurgists Wilhelm Albert and Jean-Victor Poncelet. Albert is known as the first engineer who conducted systematic fatigue studies on engineering structures studying the fatigue behavior of conveyor chains employed in the Clausthal mines (1837) [Albert, 1838]. Pon-

celet already mentions “tiring” metals in his lecture at the military school in Metz [Pook, 2007]. Among many other pioneers, which recognized the phenomenon of fatigue as well as the importance of stress concentration during loading of a material, a particular milestone for systematic studies was set by August Woehler (1860). He summarized his work on railroad axles and concluded that the cyclic stress range is more important than peak stresses. His results were later published in Ref. [Woehler, 1870].

In the beginning of the 20th century Ewing and Humfrey investigated the first metallographic micrographs revealing the evolution of surface cracks as the material is further cycled (see Ref. [Ewing and Humfrey, 1903]). In Ref. [Basquin, 1910] a double-logarithmic relationship of Woehler’s S-N data is proposed. Coffin and Manson explain fatigue crack growth in terms of plastic strain in the tip of cracks and Paris proposes methods for predicting the crack growth of individual fatigue cracks in 1961, see section 2.2.3.

Even if more than a century has elapsed on the study of the fatigue of materials it is still one of the most challenging phenomena in engineering applications since the estimation of failure subsequent to repeated loads of an engineering structure is not straightforward to predict. In the following section the most important aspects on metal fatigue are summarized, according to e.g. [Pook, 2007], [Suresh, 1991], [Dowling, 1999], [Anderson, 2005], [Gross, 1996] and [Ellyin, 1997].

2.2.2 Basic concepts of fatigue of materials

Conventionally, the fatigue behavior of a material or structure is experimentally assessed by cyclically applying a defined stress range $\Delta\sigma = \sigma_{max} - \sigma_{min}$, that is, a defined applied stress amplitude σ_a

$$\sigma_a = \frac{\sigma_{max} - \sigma_{min}}{2} \quad (2.11)$$

leading to subsequent failure after a certain number of cycles to failure, N_f . Usually the load ratio R plays an important role on the fatigue behavior and is taken into account in the experiment:

$$R = \frac{\sigma_{min}}{\sigma_{max}} \quad (2.12)$$

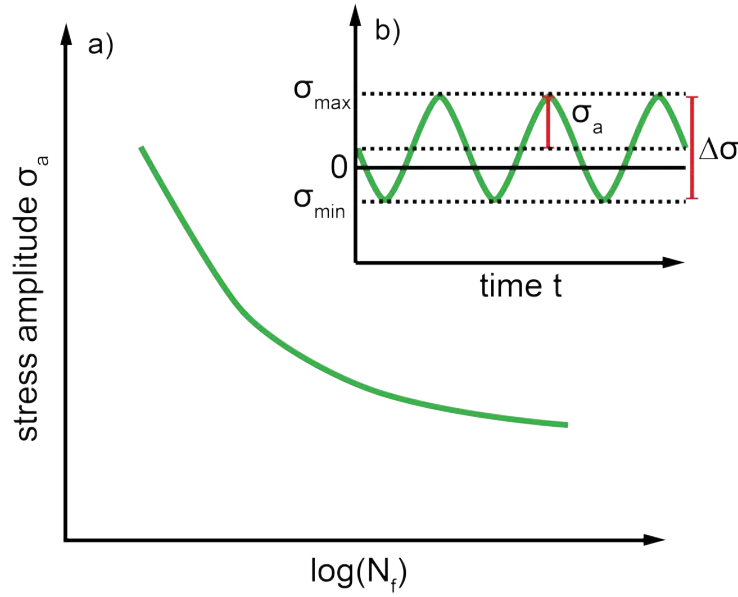


Figure 2.3: Schematic Woehler curve showing the applied stress amplitude σ_a at the ordinate and the corresponding cycles to failure N_f (log plot) at the abscissae.

where $R = -1$ corresponds to fully reversed loading and zero mean stress.

The obtained experimental data is usually visualized by a so-called Woehler curve, where the stress amplitude σ_a is plotted as against the number of cycles to failure N_f . Usually, a semi-logarithmical representation of the data is chosen. Fig. 2.3 shows a typical Woehler curve, also often called S-N curve.

Woehler curves reflect the total fatigue life of an investigated component encompassing different stages ranging from damage nucleation until ultimate failure. According to e.g. [Suresh, 1991] the progression of damage can be classified into the following regimes: 1. nucleation of permanent damage, 2. creation of microscopic cracks, 3. growth and coalescence of microscopic flaws, 4. stable crack propagation of a macroscopic crack, 5. structural instability of catastrophic failure. Thus, the described steps can be roughly subdivided into crack initiation (stage 1 & 2) and crack propagation (stage 3 & 4), followed by ultimate fracture or catastrophic failure (stage 5).

Low cycle fatigue (LCF) vs. high cycle fatigue (HCF)

In general, one can distinguish between low cycle fatigue (LCF) and high cycle fatigue (HCF). Typically, a Woehler plot where the total strain amplitude $\Delta\epsilon_t/2$ is

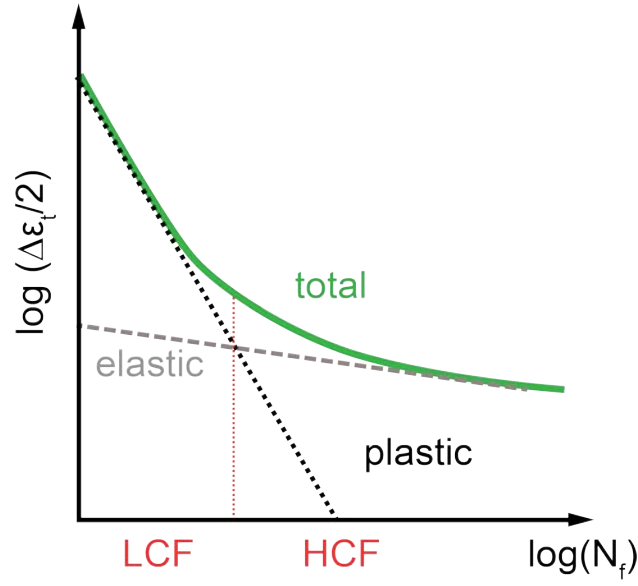


Figure 2.4: Double logarithmic Woehler plot expressed in the total strain amplitude $\Delta\epsilon_t/2$ vs. N_f showing the linear dependency of the elastic and plastic strain contributions: The cross-over separates the LCF and HCF regimes.

plotted over N_f is used to illustrate the difference between LCF and HCF. Here, $\Delta\epsilon_t/2$ is the total strain amplitude and corresponds to the sum of the elastic $\Delta\epsilon_e/2$ and the plastic $\Delta\epsilon_p/2$ amount. As can be seen in the double-logarithmic Woehler curve expressed in total strain vs. cycles to failure as shown Fig. 2.4 both – elastic and plastic – strains have a linear contribution to failure. In the LCF regime the plastic strain amount dominates, in HCF the elastic strain amount. The cross-over of both linear regimes relations defines the limit between low cycle fatigue and high cycle fatigue.

In the HCF-regime the plastic strain contribution is negligibly small compared to the elastic strain contribution and it follows that $\Delta\epsilon_t/2 \approx \Delta\epsilon_e/2$. In this regime the fatigue data can be described by the Basquin equation [Basquin, 1910], where the (elastic) strain amplitude is correlated to the number of cycles to failure by equation 2.13.

$$\frac{\Delta\epsilon_e}{2} = \frac{\sigma'_f}{E} (2N_f)^{-b} \quad (2.13)$$

where σ'_f is a coefficient, which is correlated by the static yield strength and ultimate tensile strength of the material and the exponent b is empirically obtained by a fit of

the fatigue data. In this regime microelastic mechanisms contribute to the fatigue degradation of the material.

In the LCF regime the plastic strain amount dominates. Typically these cyclic loadings occur at amplitudes above the yield strength of the material. The obtained fatigue data in this regime can be approximated by the Coffin-Manson equation, first proposed in Ref. [Coffin, 1954] and [Manson, 1954].

$$\frac{\Delta\epsilon_p}{2} = \epsilon'_{\text{f}} (2N_f)^{-c} \quad (2.14)$$

The coefficient ϵ'_{f} is related by the ultimate tensile strain obtained from the static tensile test [Christ, 1991]. The exponent c gives an information on the cyclic hardening/softening behavior of the material. The combination of equations 2.13 and 2.14 correlating the total strain amplitude $\frac{\Delta\epsilon_t}{2}$ with the number of cycles to failure N_f leads to the following relationship:

$$\frac{\Delta\epsilon_t}{2} = \frac{\sigma'_f}{E} (2N_f)^{-b} + \epsilon'_{\text{f}} (2N_f)^{-c} \quad (2.15)$$

2.2.3 Implications of fracture mechanics on fatigue

Concepts of linear elastic fracture mechanics (LEFM) are widely used in fatigue analyses. This “defect tolerant” approach recognizes the fact that the investigated structures are usually flawed. Thus, the growth of an initially introduced defect is investigated under cyclic loading to estimate when crack growth is “subcritical” up to “catastrophic” in the investigated structure [Johnson and Paris, 1968].

In the following section basic aspects of LEFM are introduced followed by the discussion of fatigue crack propagation.

Griffith fracture theory

In the early 20th century Griffith formulated the crack growth behavior of an ideally brittle material [Griffith, 1920]. He assumed that the formation or growth of a crack corresponds to a decrease of the total energy of the system, balancing the surface energy it costs to create the crack and the work energy reduction of the system. Basing on the stress analysis by Inglis in [Inglis, 1913] for an elliptical hole in an infinite elastic plate (see Fig. 2.5), Griffith formulated the following energy balance

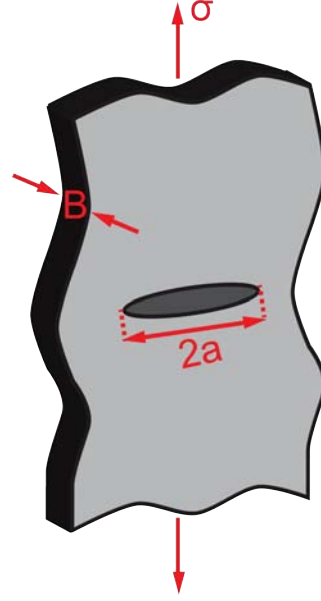


Figure 2.5: A through-thickness elliptical crack in an infinitely wide plate with thickness B subjected to a remote tensile stress (mode I) σ .

for an incremental increase of the crack area dA :

$$\frac{dE}{dA} = \frac{d\Pi}{dA} + \frac{dW_s}{dA} = 0 \quad (2.16)$$

with E denoting the total energy of the system, Π the potential energy of the system, which is dictated by the internal strain energy and the external forces, W_s the work required to create a new surface [Anderson, 2005]. Basing on Griffith's ansatz, Irwin later proposed an Energy Release Rate (ERR) approach [Irwin, 1956], which was found to be more practically applicable for engineers.

Above described theories, however do not take into account plasticity and are only applicable to materials featuring linear elastic behavior, which is the case for perfectly brittle materials. Moreover, Griffith's theory is insensitive to the curvature of the crack tip, which highly influences the resulting stress field and propagation behavior, as will be discussed below.

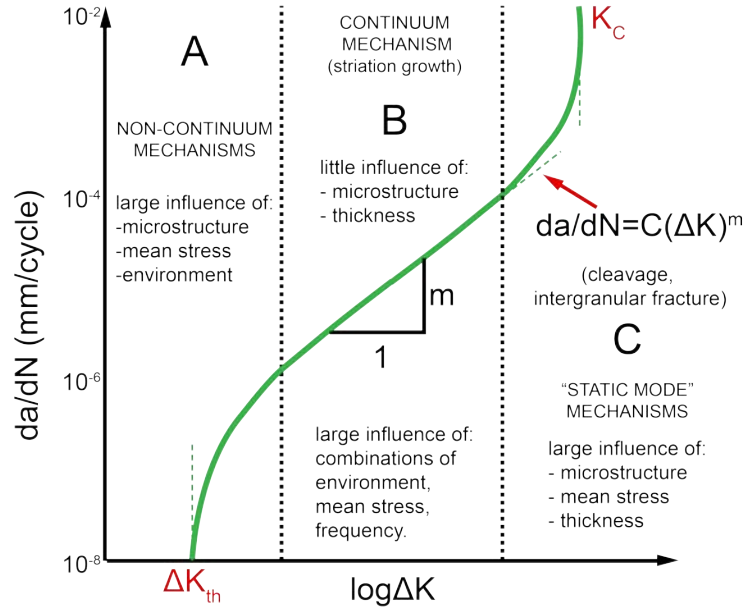


Figure 2.6: Illustration of R-curve for metallic materials showing the variation in cyclic crack growth rates da/dN , as a function of the applied stress-intensity range ΔK (redrawn after [Ritchie, 1977]).

Fatigue crack propagation

Above mentioned fracture mechanistic aspects have been further extended and successfully applied to study the crack propagation of a notched material subjected to constant cyclic load amplitudes. This approach is important since, especially in engineering applications, materials are never flawless. Thus, crack propagation investigations allow to design in a damage tolerant way. Crack propagation investigations under laboratory conditions consist in introducing a notch with defined geometry, similar to Fig. 2.5 and to apply several loading cycles causing the crack to grow. The obtained data is plotted in a so-called R-curve or crack growth resistance curve, as shown in Fig. 2.6. The R-curve illustrates the crack growth behavior da/dN , the change in the crack length as a function of the number of applied loading cycles, vs. the change of the stress intensity factor range ΔK . The stress intensity factor K depends on the applied loading mode and thus typically has an index I, II, or III referring to the loading mode. According to [Suresh, 1991] the stress intensity factor is defined as:

$$\Delta K = f(a) \Delta \sigma \sqrt{\pi a} \quad (2.17)$$

where ΔK is the difference of the stress intensity factor depending on the load maximum and minimum, σ is the applied stress range, a is the measured crack length and $f(a)$ depends on the loading mode, the sample geometry (thickness, width) as well as on the notch geometry. Peterson has summarized different stress intensity factors for given sample and load geometries and can now be found in e.g. [Pilkey and Pilkey, 2008]. As shown in Fig. 2.6, a typical R-curve for a ductile material can be subdivided into three characteristic regimes:

Stage A, near threshold regime: In this regime subcritical crack growth occurs.

Stage B, Paris(-Erdogan)-regime: Intermediate region for crack velocities in the order of 10^{-9} to 10^{-6} m/cycle: Steady crack growth occurs, following the Paris law (see equation 2.18, [Paris and Erdogan, 1963]).

Stage C, catastrophic failure: In this part, the crack grows catastrophically until it reaches a critical value for the stress intensity factor K_C .

$$\frac{da}{dN} = C(\Delta K)^m \quad (2.18)$$

where C and m , also called the Paris exponent, depend on the material properties. For metals, typical values for m range between 2 and 4 [Ritchie, 1999], [Pippan et al., 2011]. For brittle materials a very high stress intensity factor sensitivity of the crack growth rate is expected. For ceramics the Paris exponent m can reach values as high as approximately 15 to 50 and above [Ritchie and Dauskardt, 1991]. Thus, the fatigue crack propagation behavior is vastly distinct between ductile materials such as metals compared to brittle materials like ceramics or intermetallics. Fig. 2.7¹ juxtaposes characteristic crack propagation curves (R-curves) of ceramics, intermetallics and metals.

2.2.4 Overview of fatigue mechanisms

Ritchie first categorized the mechanisms promoting plasticity with crack advances into *intrinsic* and *extrinsic* mechanisms (see Ref. [Ritchie, 1977], [Ritchie, 1988], [Ritchie et al., 2000]). Since then, this classification has been widely adapted in the fatigue community see e.g. Ref [Pippan et al., 2011], [Foulk, III et al., 2008], [Wegst et al., 2015]. Fig. 2.8²

¹Reused under License Agreement between A. Lassnig and Elsevier Publishing Group provided by Copyright Clearance Center (License Nr: 3655370185698)

²Reused under License Agreement between A. Lassnig and Nature Publishing Group provided by Copyright Clearance Center (License Nr: 3655300699738)

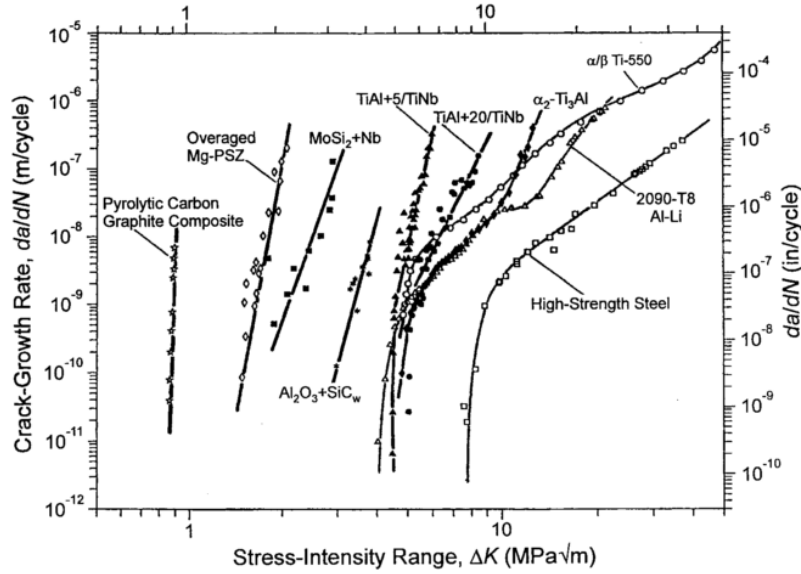


Figure 2.7: Representative R-curves for ceramics, intermetallics and metals ([Ritchie et al., 2000]).

summarized and illustrates those mechanisms occurring ahead of the crack tip (intrinsic) and in the crack wake (extrinsic). Roughly, it can be said that the intrinsic mechanisms influence the crack propagation behavior ahead of the crack tip and are governed by the inherent material properties. Therefore, they are insensitive to the geometry of the crack. Intrinsic mechanisms are mainly responsible for the crack initiation process.

In contrast, extrinsic mechanisms have little effect on the initiation processes and are associated to shielding mechanisms inhibiting further crack propagation such as zone shielding (creation of inelastic zones in the crack wake) or contact shielding (crack bridging, corrosion debris, asperities leading to crack closure in metal fatigue).

In ductile materials the shielding mechanisms are mainly intrinsic (dislocation activity, crack tip plasticity). In the case of brittle materials intrinsic mechanisms are purely associated to damage and extrinsic mechanisms allow to toughen the material.

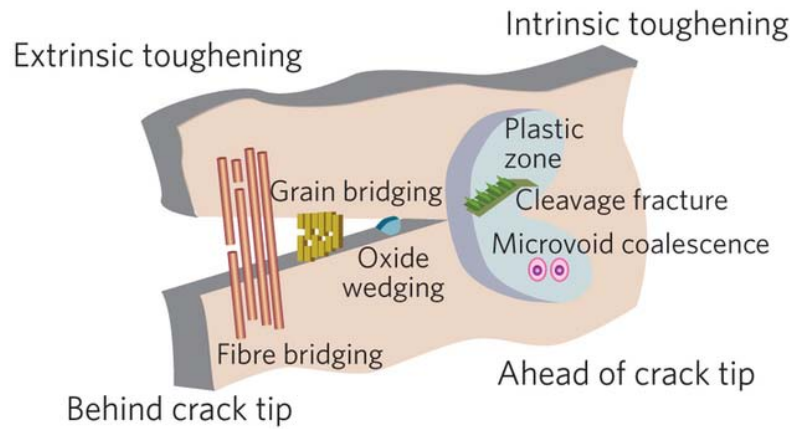


Figure 2.8: Schematic representation of the extrinsic and intrinsic toughening mechanisms occurring in a material [Wegst et al., 2015].

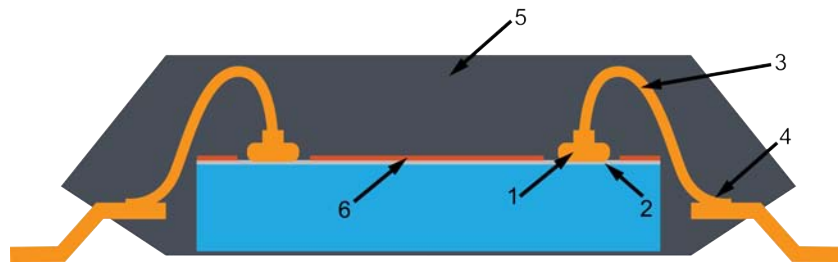


Figure 2.9: Schematic representation of microelectronic package: (1) Cu ball bond (1st level interconnect, (2) Al metallization layer, (3) Cu wire connecting package to outside circuitry, (4) wedge bond (2nd level interconnect), (5) mold compound protecting the entire chip package, (6) imid layer covering and protecting pad metallization from mold compound.

2.3 Thermosonic ball bonds in microelectronic devices

The following section is dedicated to thermosonic ball bonding, a commonly used technology to create miniaturized interconnects in microelectronic devices. This technology was first introduced in the 1970s and is a solid – solid joining technology for first level interconnects, where a strong connection between a thin wire (typically in the order of 25 μm to 75 μm diameter) and a thin pad metallization, which covers the microchip, is created. A schematic cross section of a typical microelectronic device is illustrated in Fig. 2.9 highlighting the ball bond interconnect.

Various materials combinations are eligible for this interconnection type. Previ-

ously, the standard material combination were gold wires bonded on aluminum pads (see e.g. [Wulff et al., 2007], [Wulff et al., 2007], [Wulff et al., 2007]). In the case of Au-Cu ball bonds, various problems were encountered such as Kirkendall void formation (see e.g. Ref. [Murali et al., 2004], [Li et al., 2006]) and detrimental intermetallic formation known as “purple plague” ([Philofsky, 1970], [Xu et al., 2010]) subsequent to high temperature exposure.

Nowadays, due to economic reasons, the ball bonding process has been adapted to replace formerly employed gold wires by copper wires. In this present work the focus is mainly set on Al-Cu ball bonds. First, the thermosonic ball bonding procedure including the involved mechanisms are discussed in 2.3.1. During service, microelectronic devices are subjected to elevated operating temperatures leading to microstructural changes at the Al-Cu interface due to marked interdiffusion. The microstructural evolution leads to the formation of intermetallic compounds, which are discussed in section 2.3.3. Standard test techniques, currently employed to assess the reliability of the bond interface, are summarized in 2.3.4, followed by a brief literature overview on the shear test results as a function of intermetallic compound evolution in Al-Cu ball bonds. Finally, a novel fatigue testing method specially designed for wire-bond interconnects utilizing an ultrasonic resonance fatigue system is presented in 2.4.2.

2.3.1 Thermosonic ball bonding process

The key process steps of thermosonic ball bonding are elucidated hereafter. A miniaturized interconnect between a thin metallic wire (typically from 25 μm to 75 μm diameter) and a metallization “skin” (thickness of few μm) is created by employing a compressive force, ultrasonic energy and heat.

During the bonding process both materials are in solid condition [Harman, 2010]. In Fig. 2.10 the ball bonding process is sketched. The thin wire to be bonded is clamped and manipulated by a small capillary tool. As a first step the wire tip is melted by an electric flame off (EFO) technique and subsequently solidified to a free air ball (FAB) due to surface tension. Then, the FAB is brought closely to the pad surface, where a compressive force is applied (around 140 MPa) ensuring a strong contact between both materials to be bonded. Finally, ultrasound is applied between 120 – 140 kHz to soften the Cu ball and the Cu ball is rubbed into the pad metallization, which creates the thermosonic ball bond. To facilitate the creation of a sound bond interface and to spare the chip material, elevated tem-

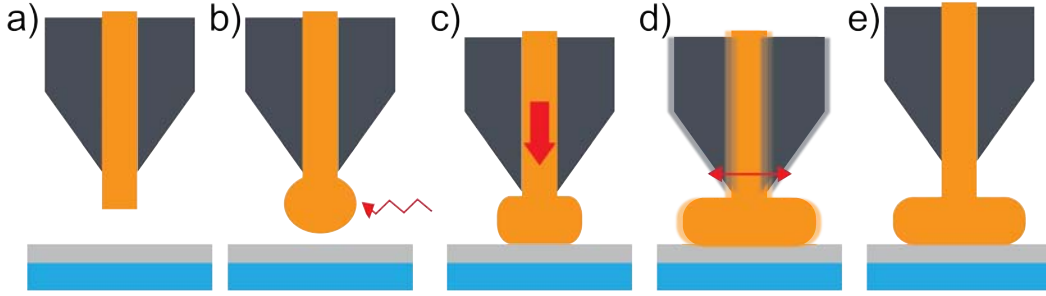


Figure 2.10: Schematic of ball bonding process: The wire to be bonded is clamped by capillary tool (a), followed by electric flame off to soften the wire tip resulting in the creation of a free air ball due to surface tension (b). Then the wire tip is lowered to the bonding pad, where an additional normal force is applied to ensure a close contact of both bonding surfaces (c). A frictional motion induced by ultrasonic energy results in the creation (d) of a thermosonic ball bond, where high plastic deformation occurred (e). Redrawn and modified after e.g.[Harman, 2010].

peratures between 125 °C and 250 °C are applied during the ball bonding procedure [Harman, 2010], [Breach and Wulff, 2010], [Schneider-Ramelow et al., 2013], [Xu et al., 2010].

Thus, it can be concluded that the following process steps and primary condition of the bonding materials highly determine the quality of the future bond interface:

Initial pad condition: Pad roughness and absence of oxides and debris are crucial to ensure a flat and parallel interface across the bonds. In [Pelzer et al., 2012] a preliminary pad cleaning procedure ensuring optimum bond conditions is mentioned.

Flame-off melting and creation of FAB: Usually, it is aimed at obtaining a perfectly spherical free air ball as it dictates stability throughout the bonding process and ensures a homogeneous transmission of the bond forces through the capillary. A study by Hang et al. discusses the optimum parameters to reduce the weak heat affected zone (HAZ) and to create a homogeneous, spherical FAB [Hang et al., 2009] by means of an electric sparking process according to the previous studies in [Huang et al., 1995], [Cohen et al., 1995]. During flame off elongated coarse grains occur in the FAB, followed by the heat affected zone (HAZ), as illustrated in Fig. 2.11.

Bond process parameters: Applied thermosonic energy, compressive force, substrate temperature and bonding duration need to be optimized to ensure a strong,

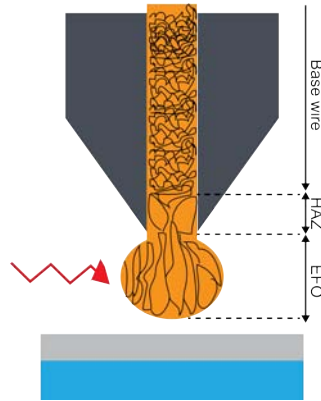


Figure 2.11: Schematic grain size distribution subsequent to free air ball (FAB) formation, showing elongated coarse grains in the FAB, a transition coarse grained area called the heat affected zone (HAZ) and the small grained base wire material. Redrawn after e.g. [Hang et al., 2009].

throughout bond interface. Xu et al. found in [Xu et al., 2011a] that the increase of the bonding duration leads to an increase of the ball shear strength but also to an increase in the formation of interfacial intermetallic compounds. The same authors also found that an increase of the substrate temperature leads to an increase of the ball shear strength, which is attributed to an acceleration of the bonding process since diffusion is facilitated at elevated temperatures. Qin et al. stated in [Qin et al., 2011] that the ball shear strength should not be considered as the only quality criterion but also minimal pad damage subsequent to the bonding process. In-situ pad stress tests were conducted to monitor the bonding process parameters i. a. the ultrasonic energy and applied bonding force. It was found that both need to be kept minimal to minimize pad stress damage.

2.3.2 Mechanisms of thermosonic ball bond process

Various mechanisms contribute to the formation of the thermosonic bond interface such as the frictional motion, elevated substrate temperature and the addition of ultrasound. While it is intuitive that the frictional motion serves as plastic deformation process and furthermore removes inhibiting debris of both bonding partners, the effect of ultrasound on the metal deformation and phase formation still remains unclear [Breach and Wulff, 2010]. Some studies claim that intermetallic phase formation during the bonding process is responsible for the creation of the

bond. However, in the case of Al-Cu bonds the presence of nucleated intermetallic compounds (IMCs) in the as-bonded state different statements could be found in literature. E.g. in [Drozdov et al., 2008a] nucleated IMC were found, while in more recent studies e.g. in [Pelzer et al., 2012] their presence could not be confirmed in the as-bonded state.

2.3.3 Microstructural evolution of Al-Cu ball bonds

Thermosonic wirebonds are subjected to elevated service temperatures and thermal fluctuations due to increased operating temperatures and Joule heating. It is well-known that elevated temperatures (typically up to 150 °C) foster interdiffusion of both materials into each other at the bond interface, which leads to the formation of intermetallic compounds (see e.g. Ref. [Drozdov et al., 2008b]). In previous studies ([Xu et al., 2011b], [Pelzer et al., 2012]) it was found that the growth of the total intermetallic stack as a function of annealing time obeys a parabolic law described by the following equations:

$$x(t) = (D \cdot t)^{\frac{1}{2}} \quad (2.19)$$

where x denotes the total thickness of the interfacial intermetallic compounds as a function of time t and D is the diffusion coefficient (m^2s^{-1}) depending on the (absolute) temperature T :

$$D = D_0 \cdot \exp\left(\frac{-Q}{RT}\right) \quad (2.20)$$

where D_0 is the diffusion constant depending on the material properties. Typically, this constant depends on the atomic distance, the number of point defects (vacancies, interstitial sites allowing to “host” an atom) occurring in a lattice, Q is the activation energy in Joule, R is the molar gas constant $8.3144621 \frac{\text{J}}{\text{mol} \cdot \text{K}}$, and T is the absolute temperature in Kelvin. For the growth behavior of Al-Cu intermetallics in thermosonic Al-Cu bonds Xu and co-authors reported in Ref.[Xu et al., 2011b] that at 200 °C the growth rate constants for Al_2Cu and Al_4Cu_9 are $7.80 \cdot 10^{-19} \text{m}^2 \text{s}^{-1}$ and $2.10 \cdot 10^{-19} \text{m}^2 \text{s}^{-1}$, respectively. In the same study activation energies for Al_2Cu and Al_4Cu_9 were found to be 60.66kJ/mol and 75.61kJ/mol at temperatures be-

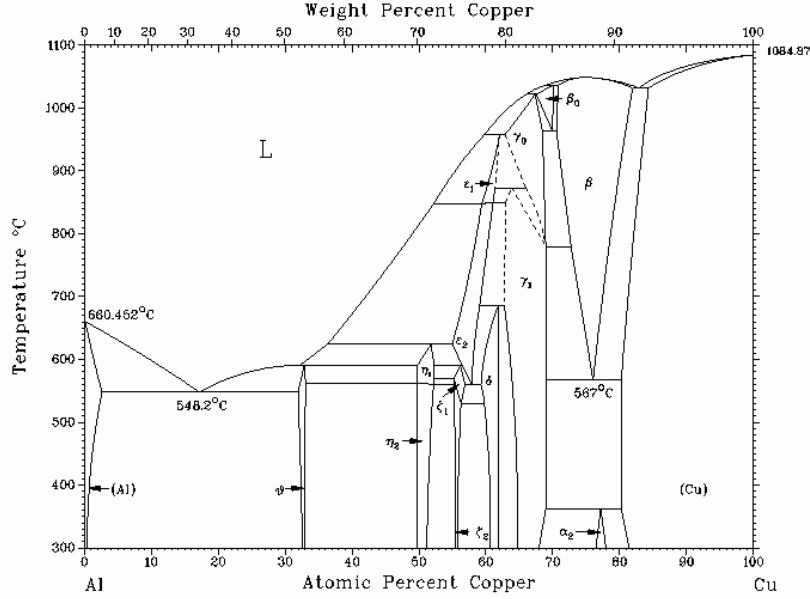


Figure 2.12: Binary Al-Cu phase diagram ([Murray, 1985]).

tween 175 °C and 250 °C, respectively. The growth thickness x of the total stack of intermetallic compounds obeys a parabolic law during thermal aging, which is indicative that the main diffusion mechanism is bulk solid state diffusion.

Al-Cu intermetallic formation and their physical properties

When looking at the binary Al-Cu phase diagram in Fig. 2.12 the possible intermetallic phases that are stable below 300 °C are Al₂Cu (ϑ), AlCu (η_2), Al₃Cu₄ (ζ_2), Al₂Cu₃ (δ) and Al₄Cu₉ (γ_2), which also appear in this order across the interface, where the phase containing the highest aluminum concentration is closest to the aluminum side and the phase with highest Cu amount is adjacent to the Cu side.

Intermetallic compounds are well-known to feature disparate physical properties compared to their metallic parent materials. There exists a preponderance of studies concerning the static characterization of the physical properties of above mentioned intermetallic compounds mainly motivated by electronic applications: E.g. in the following studies [Kouters et al., 2011], [Kouters et al., 2013], [Braunovic et al., 2010], [Rabkin et al., 1970] various physical properties such as hardness, density but also electrical properties of these materials are compared. In a study conducted by

Table 2.1: Physical properties of Al-Cu intermetallic compounds [Kouters et al., 2013] are summarized hereafter, where at.% Cu refers to the atomic concentration of Cu in the investigated IMC, E is the Young's modulus, ρ is the mass density, K_{IC} is the fracture toughness, form. E is the energy of formation required to build such IMCs, CTE is the coefficient of thermal expansion.

Material	at.%Cu	E (GPa)	ρ g/cm ³	K_{IC} MPam ^{1/2}	H _V MPa	form. E eV/atom	CTE ppm	Crystal structure
Al	0-2.84	70	2.7	14-28	20-50		23.5	fcc
Al ₂ Cu	32-33	124 ± 7	4.38	0.27 ± 0.06	324	-0.1553	16.1	tetragonal
AlCu	50-52	180 ± 13	5,36	0.20 ± 0.03	628	-0.2134	11.9	monoclinic
Al ₃ Cu ₄	55-56	na	na	0.21 ± 0.05	616		16.1	monoclinic
Al ₂ Cu ₃	59-62	na	na	0.68 ± 0.15	558		15.1	trigonal
Al ₄ Cu ₉	63-69	187 ± 9	6.85	0.67 ± 0.10	549	-0.2105	17.6	cubic
Cu	80-100	120	8.93	12-22	60-100		17.3	fcc

Lee et al. ([Lee et al., 2005]) a drastic increase of the electrical resistivity with increased intermetallic compound evolution could be proved. The main findings of the mechanical properties of the intermetallic compounds are summarized in table 2.1 proving that an increased hardness, increased brittleness (i.e. reduced indentation toughness) compared to the parent materials could be found. This may be attributed to their stronger atomic bonding type (while the parent materials have metallic bonds, intermetallics typically have a more covalent bond) as well as to their lower symmetries hindering plastic deformation.

2.3.4 State of the art test methods for ball bond interface

The standardized test techniques to assess the bond quality are the destructive wire pull and ball shear tests, as illustrated in Fig. 2.13. Both tests are static test methods and have been widely discussed by e.g. [Bisschop, 2007], [Harman, 2010]. The wire pull test consists in pulling the loop between ball bond and 2nd level interconnect (usually of wedge bond type) until the weakest link fails, where the force necessary to rupture the loop is recorded. If both interconnects are intact, the wire loop is prone to fail at its weakest site, which is at the heat affected zone due to the free air ball formation process. It follows that this test procedure only indirectly tests the ball bond interface: a rupture of the bond would account for an extremely weak bond. As opposed to the wire pull test, the ball shear test allows to determine the reliability of the ball bonded interface. This method follows the industrial JEDEC standard [JEDEC, 2009]. Here, a miniaturized chisel-shaped

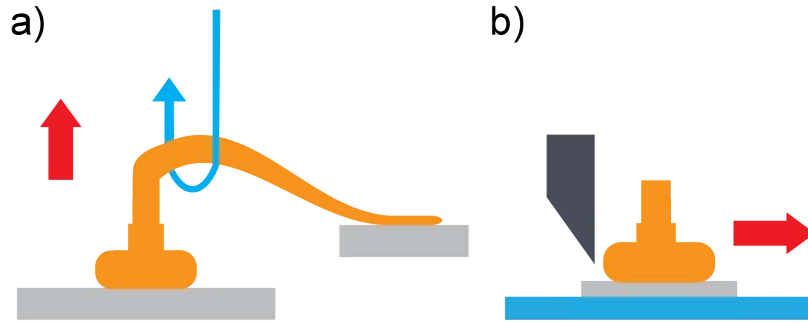


Figure 2.13: Schematic of wire pull (a) and ball shear (b) tests.

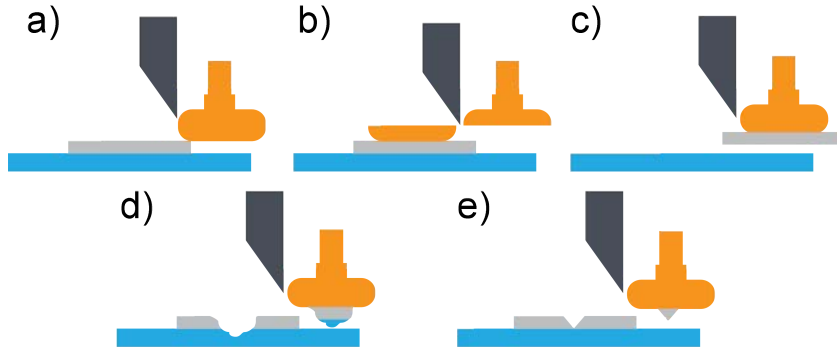


Figure 2.14: Typical failure modes during ball shear testing (a) ball lift off, (b) ball shear, (c) pad metallization lift off, (d) chip cratering and (e) metallization cracking.

tool is placed at a defined height above the bond interface and shears the ball off the bond pad. The force required to rupture the entire bond is recorded, followed by a subsequent visual inspection of the fractured area.

Effect of microstructural evolution on ball shear test results for Al-Cu bond interface

In various studies the effect of intermetallic compound evolution on the static shear strength of thermosonic Al-Cu ball bonds has been widely investigated. The results though are not necessarily consistent:

E.g. Pelzer et al. have thoroughly characterized Cu-Al ball bond shear strengths as a function of heat treatments in [Pelzer et al., 2012]: It was found that the activation energy for the entire intermetallic stack is 1.26 eV. Static shear values were compared to the annealing matrix but significant changes in the shear force

values with increased IMC formation was not observed. In another study, Amistoso et al. found a slight decrease of ball shear strength as a function of time and temperature [Amistoso and Amorsolo, 2010]. Bond degradation due to intermetallics formation has usually been associated to the formation of cracks and voids subsequent to interdiffusion and not to the intrinsic physical properties of the intermetallics [Hang et al., 2008].

2.4 Ultrasonic fatigue testing of materials

The usage of ultrasonic resonance systems for fatigue testing purposes originates in 1950, where Mason built the first piezoelectric fatigue testing machine translating electrical voltage signals into mechanical displacements operating at 20 kHz. The main benefit lies in an extreme time reduction such that the high cycle fatigue (HCF) and ultra high cycle fatigue (UHCF) regimes up to a total of 10^{10} loading cycles can be tested in reasonable time. In this section the functional principle of ultrasonic fatigue testing is briefly explained (see 2.4.1). Finally, a modification of ultrasonic fatigue testing specially designed to test miniaturized interconnects and bond interfaces occurring in microelectronic components is presented in 2.4.2.

2.4.1 Principles of ultrasonic resonance fatigue testing

The usage of ultrasound for fatigue testing dates back to the 1950s (see Ref. [Mason, 1956]). The working principles of ultrasonic fatigue testing is explained hereafter, according to e.g. [Roth, 1985],[Stickler and Weiss, 1982].

In ultrasonic fatigue testing a sufficiently high strain amplitude in the specimen is cyclically induced leading to subsequent fatigue failure of the specimen. Typically the testing setup is comprised of a converter generating ultrasonic displacement waves, an acoustic horn which transmits and amplifies the signal followed by an extension horn and the specimen itself. Consequently, an acoustic signal leading to mechanical strains travels through the entire setup. The velocity c of this signal depends on the material properties of each component and can be described by the following equation 2.21.

$$c = \left(\frac{E}{\rho} \right)^{\left(\frac{1}{2} \right)} \quad (2.21)$$

with E denoting the dynamic Young's modulus of the material and ρ its mass density. c is usually referred to as the velocity of sound. Once the sound wave has reached the end of the setup it is reflected by the front wall and travels back to its origin. If the reflected soundwaves are exactly in phase with incoming soundwaves a standing wave condition is fulfilled and the setup is in resonance. In this case the displacement amplitude $u(x, t)$ as a function of location x along the one dimensional setup can be expressed by equation 2.22

$$u(x, t) = u_0 \cdot \cos\left(\frac{\pi x}{L}\right) \cdot \sin(\omega t) \quad (2.22)$$

u_0 is the maximum displacement amplitude at the end of the bar, L the length of the setup, λ the wave length at resonance frequency and ω ist the angular frequency:

$$\omega = \frac{2\pi}{\lambda} \cdot c = \frac{2\pi}{\lambda} \cdot \sqrt{\frac{E}{\rho}} \quad (2.23)$$

The corresponding strain distribution $\epsilon(x, t)$ is obtained by the first derivative of above mentioned displacement distribution.

$$\epsilon(x, t) = \frac{\partial u(x, t)}{\partial x} = -\frac{\pi}{L} \cdot u_0 \cdot \sin\left(\frac{\pi x}{L}\right) \cdot \sin(\omega t) \quad (2.24)$$

Thus, strain and displacement distribution along the resonating ultrasonic fatigue setup follow a sinusoidal distribution and are $\pi/2$ -phase shifted. Fig. 2.15 shows a schematic ultrasonic resonance fatigue setup where the strain and displacement distribution are illustrated. Thus, if the specimen is adequately designed maximum strain occurs in the center - i.e. at $\lambda/4$ -, whereas maximum displacement occurs at the end i.e. at $\lambda/2$ of the specimen. Assuming that the stresses induced in the specimen are - mainly- purely elastic, Hooke's law can be assumed, see equation 2.3.

2.4.2 Ultrasonic fatigue testing of miniaturized bond interfaces

A novel test technique as an alternative to conventional mechanical test methods assessing the reliability of microelectronics bond interfaces utilizing an ultrasonic resonance fatigue system 2.4.1 was first introduced by [Khatibi et al., 2008], where

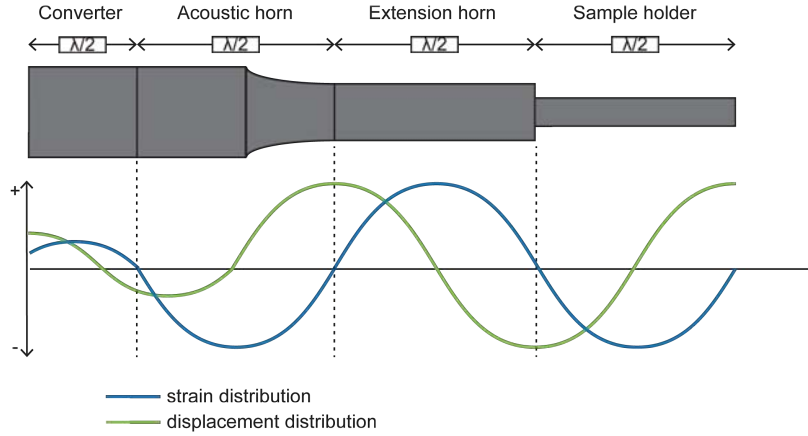


Figure 2.15: Scheme of ultrasonic fatigue resonance system, redrawn and slightly modified after [Roth, 1985].

the first mechanical fatigue measurements were conducted on 400 μm thick Al wedge bonds occurring in IGBT (insulated gate bipolar transistor) modules. Recently this test technique has been widely applied to assess the reliability of different wire bond interconnect types (see e.g. Ref. [Khatibi et al., 2010], [Magnien and Khatibi, 2014], [Walter et al., 2015]). The working principles of this novel technique are briefly elucidated in the following section.

Specially designed to tackle the lifetime performance of miniaturized wire bond interfaces, this method bases on the induction of cyclic -mechanical- shear stresses in the targeted bonding interconnect utilizing an ultrasonic resonance fatigue system operating at 20 kHz. Each part of this set-up including the sample holder fulfill the resonance condition. Thus, strain and displacement signals follow a $-\pi/2$ -phase shifted- sine-shaped standing wave along the set-up respectively. The test device is mounted at the end of the specimen holder (i.e. where maximum acceleration node is located) such that the tested interface acts as a coupling between two differently inert masses: The bulk sample holder- part of the ultrasonic fatigue setup- and the miniaturized active mass above the bond. Differently inert masses lead to a slightly phase shifted motion resulting in cyclic shear stresses at the bond interface. The subsequent fatigue failure type is a so-called bond lift-off, where the micro component is detached at the bond interface, revealing the weakest link of the bond. The average cyclic shear stress τ acting on the bond during the experiment can be

estimated by equation 2.25.

$$\tau = \frac{m \cdot a}{A} \quad (2.25)$$

where m denotes the active mass above the bond, a the acceleration and A the bonding area respectively. Both, active mass m and bonding area A are measured post-mortem. In the case of thick Al wire bonds an upside down sample position was chosen, where the wire was directly attached to the sample holder, which is part of the ultrasonic resonance fatigue system. From equation 2.25 it follows that the shear stress amount leading to fatigue lift off in the bond is proportional to the mass-to-area ratio determined by the sample geometry. The acceleration can be varied either by tuning the power amplitude of the ultrasonic fatigue setup or by choosing a suitable acoustic horn, which amplifies (attenuates) the signal proportional to the ratio of the cross-sectional areas. A schematic of the functional principle of ultrasonic fatigue testing of miniaturized joints in microelectronic devices is illustrated in Fig. 2.16.

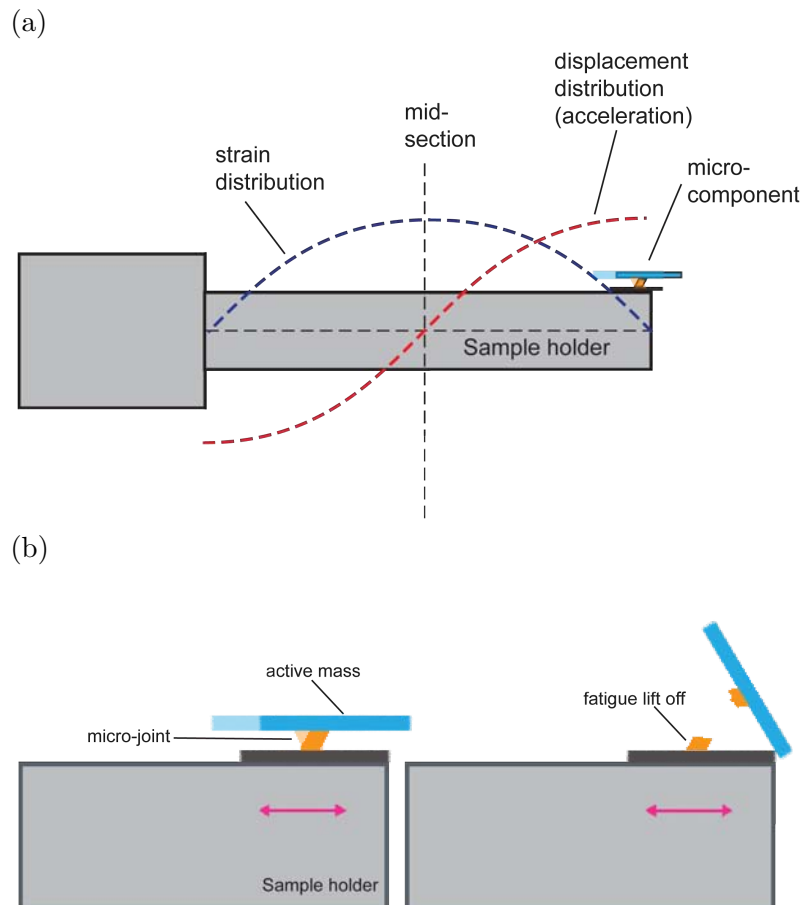


Figure 2.16: (a) Overview of ultrasonic resonance fatigue system for fatigue tests of bonded interconnects (b) Schematic close up: Shear stress at the bond leading to fatigue lift off at the weakest site of the bond.

3 Mechanical fatigue of miniaturized Cu-based ball bonds

In this chapter high cycle fatigue (HCF) properties of copper-based ball bond interfaces occurring in standard microelectronic components are studied. Special emphasis is set on thermosonic ball bonds, which are utilized in various technological applications such as automotive industry. Therefore a tailored fatigue test technique was designed utilizing an ultrasonic resonance fatigue system in combination with special sample preparation techniques to induce cyclic mechanical stresses in the investigated bond interface. A main question in the context of bond reliability is how the fatigue response of the bond interface is affected due to intermetallic compound formation subsequent to thermal exposure.

Finally, two measurement series are conducted to tackle the following questions:

1. How does intermetallic compound formation as a consequence of high temperature exposure influence the high cycle fatigue properties of miniaturized Cu-Al interfaces? How does it compare to the standardized static shear tests?
2. How does the variation of pad metallization material influence the fatigue properties of Cu-based thermosonic ball bonds?

In 3.1 the investigated ball bond specimen is briefly described. The fatigue testing methods specially designed for miniaturized ball bonds are presented in 3.2 and can be subdivided into single bond and multiple bond testing. Single bond testing allows to test each ball bond individually, whereas multiple bond testing allows to test several ball bonds belonging to one chip simultaneously.

In section 3.4 the role of intermetallics formation on the fatigue behavior of Al-Cu bond interfaces is investigated including a detailed microstructural characterization of selected interfacial conditions by means of electron microscopy techniques. Therefore, fatigue tests were conducted on three microstructural states by means of the above mentioned single bond test technique followed by a detailed analysis

of the microstructure dependent fatigue fracture morphology in 3.4.3. The main results presented in these sections were published in [Lassnig et al., 2015]. In the last section 3.5 the fatigue behavior of Cu-Cu ball bonds is compared to the previously studied Al-Cu ball bonds by means of multiple bond testing, to prove the applicability of the proposed test methods to several metallization materials.

3.1 Investigated Cu-Al ball bond specimen

The investigated specimens are from the same technology as in [Lassnig et al., 2012], [Pelzer et al., 2012] and are typical thermosonic Al-Cu ball bonds in microelectronic devices for automotive applications. They were provided in unmolded condition by Infineon Villach. A 50 μm thin Cu wire of 99.99 % purity was thermosonically bonded on a 5 μm thin Al (0.5 % Cu) metallization, which results in a final bonding area of approximately 135 μm diameter and a Cu ball of about 30 μm height. The sputter deposition of the metallization occurred in a Trikon SIGMA-FXP chamber. Prior to bonding a pad cleaning process was conducted to allow optimum bonding conditions by the reduction of debris. For the actual ball bond process an ASM iHawk Xtreme bonder was utilized in combination with a standard reducing atmosphere nozzle kit to avoid oxidation and debris of the Cu wire during free air ball sparking.

In Fig. 3.1a a SEM cross section of a typical loaf-shaped ball bond is shown, where a pronounced splash of the soft Al pad is visible. Metallization splashing parallel to the bonding direction occurs due to high plastic deformation of the soft pad material during the bonding process. In Fig. 3.1b a close up of the as-bonded Al-Cu interface is depicted: A flat, plane interface is shown revealing no visible interdiffusion zones or nucleation of intermetallic compounds.

3.2 Development of accelerated fatigue tests for miniaturized ball bonds

As described in 2.4.2 microelectronic components can be tested by means of an ultrasonic fatigue resonance system. The component to be tested is mounted at the end of the sample holder, which is part of the load train of the resonating setup and thus the microcomponent is excited to longitudinal push-pull motion following the excitation of the bulk sample holder. By additional usage of an “ac-

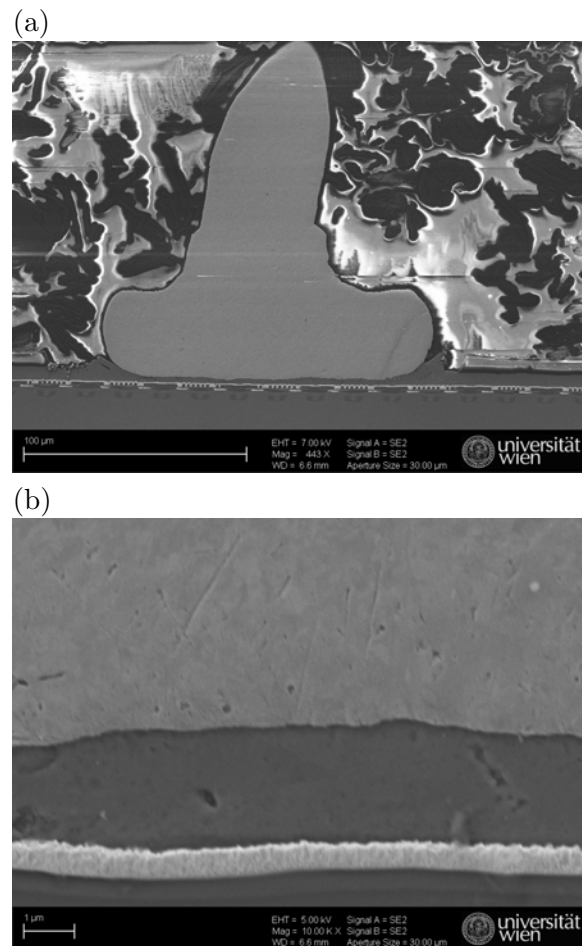


Figure 3.1: (a) SEM cross section of unmolded Cu ball bonded on Al. A pronounced Al splash parallel to the bonding direction is visible. (b) High magnification of Al-Cu interface showing no traces of IMC formation in the as-bonded state.

tive” mass, which is located above the bond the longitudinal excitation leads to a slightly phase shifted motion between two differently inert masses – the mass of the specimen holder and the mass above the tested bond. Consequently, the bond acts as coupling between both parts and is therefore subjected to cyclic shear stresses, which lead to subsequent fatigue lift off. According to equation 2.25 estimating the shear stress amount acting on the bond, this can only be achieved by a suitable (active)mass-to-(bond)area-ratio, which can only be realized by a suitable specimen setup. To check if sufficiently high stresses can be induced in the miniaturized loaf shaped ball bonds, a rough estimate of the shear stresses is made hereafter.

The shape of a typical Cu ball as shown in Fig. 3.1 can be approximated by a flat cylinder assuming a diameter of 135 μm and a height of 35 μm . This corresponds to a bonding area of about 14300 μm^2 and a volume of about 500000 μm^3 (i.e. $5 \cdot 10^{-7} \text{ cm}^3$). With the mass density of copper being 8.92 gcm^{-3} this leads to an active mass of approximately 4.5 μg . In ultrasonic fatigue testing accelerations in the order of 100 km/s^2 are typically achieved. Thus it follows from equation 2.25 that shear stresses are in the order of $3 \cdot 10^{-8} \text{ MPa}$; however it is expected that stresses leading to fatigue failure of bond interfaces shall be in the order of MPa or tens of MPa. Consequently, a successful application of the fatigue test to miniaturized, loaf-shaped ball bonds can only be realized by means of a sample modification, where the mass of the Cu ball is artificially increased without wetting the underlying metallization.

Thus, improved sample preparation techniques basing on previously developed prototypes [Lassnig et al., 2012],[Lassnig et al., 2013] are presented resulting in two distinct ball bond test approaches, where soldering builds the basis of the proposed sample modifications:

Single bond testing This test technique allows to evaluate each bond individually.

A special soldering technique called ”solder jetting” is employed to increase the mass of each Cu ball individually. Here each fatigue data point can be correlated to a specific bond. Furthermore, this technique is layout independent and thus easily adaptable for different technologies.

Multiple bond testing Several bonds are simultaneously tested, where a sandwich-type sample setup is chosen. A specially designed template allows a precise application of the solder paste such that every bond is covered with solder.

For the fatigue test an upside down geometry is used, where the Cu balls strongly adhere to the solder and where the mass of the chip serves as active mass during fatigue tests. Here each obtained data point is representative for an average bond quality per device.

A more detailed description of the sample preparation techniques will be given below.

3.2.1 Single bond testing

For single bond testing each ball bond is prepared individually. This allows a precise determination of the fatigue life of selected ball bonds. Therefore a soldering technique, conventionally used in ball grid array (BGA) mounting called "solder jetting" is employed to artificially increase the mass of the Cu ball. Solder jetting allows to reflow solder spheres between 40 μm and 760 μm diameters to a desired assembly, where a capillary tool manipulates the solder ball and places it to the desired position. Finally, a laser beam instantly reflows the solder ball. Besides from being an ultra fast soldering procedure the main benefit lies therein that the components are soldered without mechanical contact nor with additional chemical treatments. Potential stresses (chemical, thermal or mechanical) originating from the preparation are kept minimal and therefore it can be assumed that the bond quality is not impaired by this manipulation. Key steps of single bond solder jetting are briefly sketched in Fig. 3.2 and explained below:

First, the wire is carefully removed by smooth wobbling leading to natural fracture at the transition between the heat affected zone (HAZ) and the fine grained area of the wire. Then, the bare Cu ball is soldered promptly after a cleaning procedure with ethanol to ascertain a strong solder-Cu-adhesion. Several ball bonds on a chip can be tested independently regardless of the design and arrangement of the ball bonds. Fig. 3.3 shows the SB²-M-Jet Solder Jetting assembly used for the specimen preparation.

Two measurement series were conducted by means of single bond testing. For both series eutectic Pb₃₇Sn₆₃ (low melting point at 183 °C) solder balls were utilized. In the first measurement series -"MR1"- solder balls with a diameter of 600 μm were utilized resulting in an active mass of 0.57 mg. Fig. 3.4a shows a cross section of the prepared specimen. As can be seen, the flat solder ball touches the underlying metallization showing a hint of wetting and thus it is assumed that the chosen solder balls were too big for this purpose. Thus a second, improved measurement series

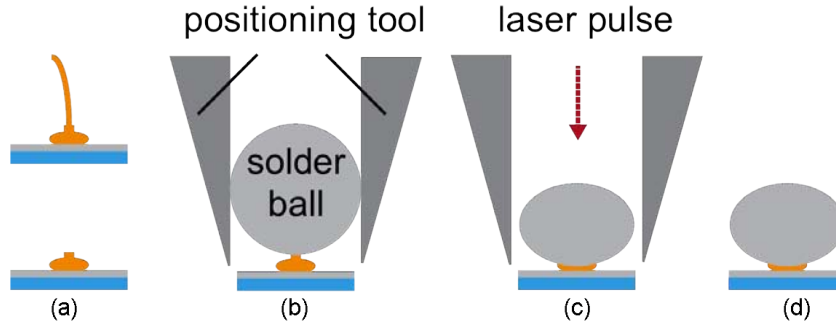


Figure 3.2: Key steps for solder jetting of fatigue specimen: (a) Removal of bond wire and degreasing ball bond surface with ethanol (b) a capillary tool clamping the solder sphere is positioned above the ball bond to be soldered. (c) Finally, a laser pulse is emitted leading to fast reflowing of the solder ball and the Cu ball. (d) shows a sketch of the prepared ball bond for fatigue testing.

-“MR2”- was performed, where solder spheres of a diameter of 400 μm resulting in an active mass of 0.29 mg were chosen. Fig. 3.4b shows a cross section of the improved specimen, where a small solder bump is precisely reflowed to the Cu ball bond revealing a clear gap between the solder sphere and the bond metallization and imid layer. Both fatigue tests were conducted on Al-Cu ball bonds of the same technology. The obtained fatigue data of both MR1 and MR2 is summarized in section 3.2.3.

3.2.2 Multiple bond testing

The multiple bond test technique presented in an earlier work [Lassnig et al., 2013] consisted in covering several ball bonds with solder paste topped with a thin copper plate to ensure uniform soldering of the ball bonds. During reflow however it was found that solder contracted non-uniformly leading to an uneven coverage of the bonds. Thus, to improve this test technique such that uniform soldering of each ball bond is ensured, the previously employed sandwich type soldering technique should be improved by introducing a dedicated template acting as a solder fixture, where each Cu ball can be equally soldered. Therefore, the soldering template should meet the following requirements:

- Precise positioning of the sample during soldering
- Uniform and reproducible soldering of each ball bond

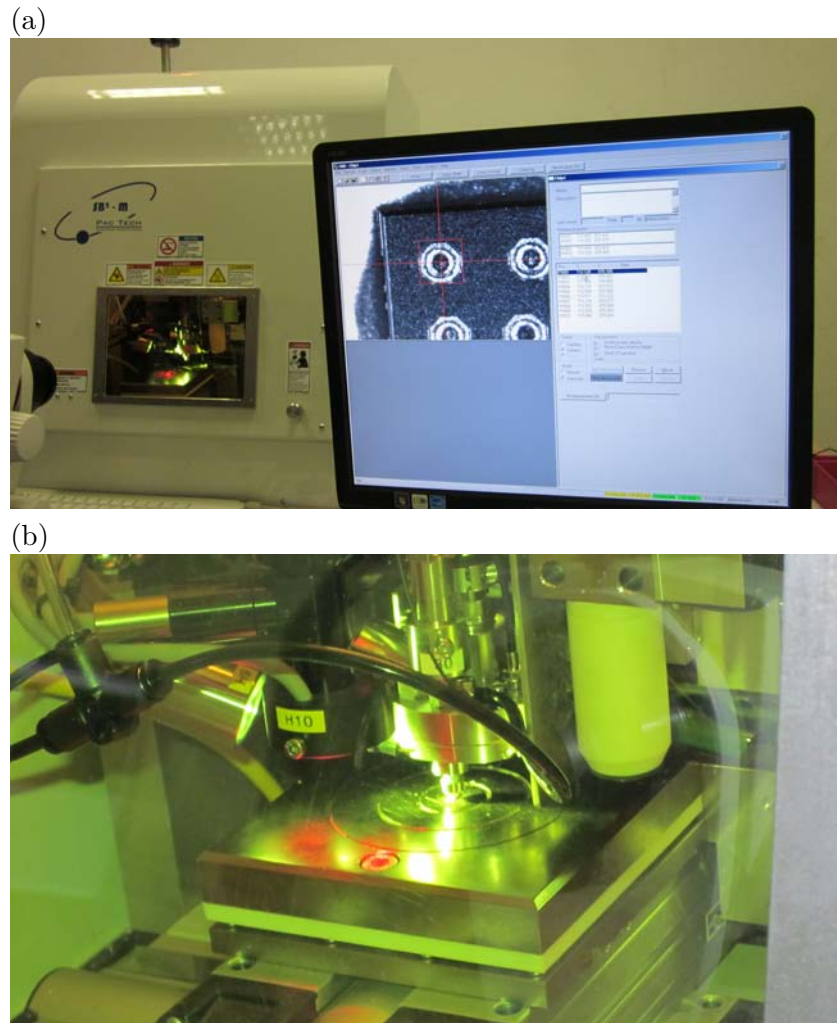


Figure 3.3: (a) Overview of SB²-M-Jet Solder Jetting assembly. The PC screen shows positioning of the selected ball bonds (top view) to be jetted (b) Close-up of the laser jetting system when operating.

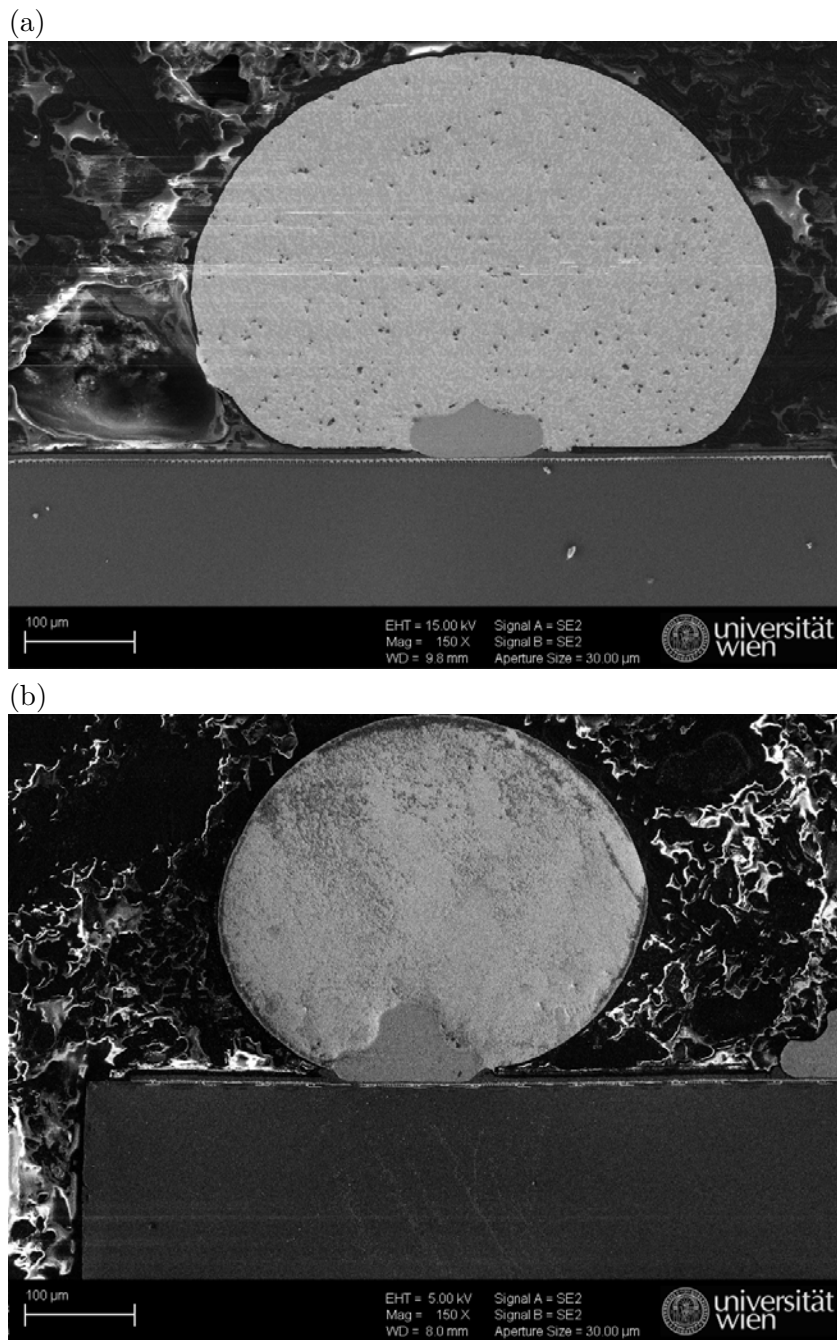


Figure 3.4: SEM cross section of solder jetted ball bond (a) 600 µm diameter (active mass 0.57 mg) (b) 400 µm diameter (active mass of 0.29 mg).

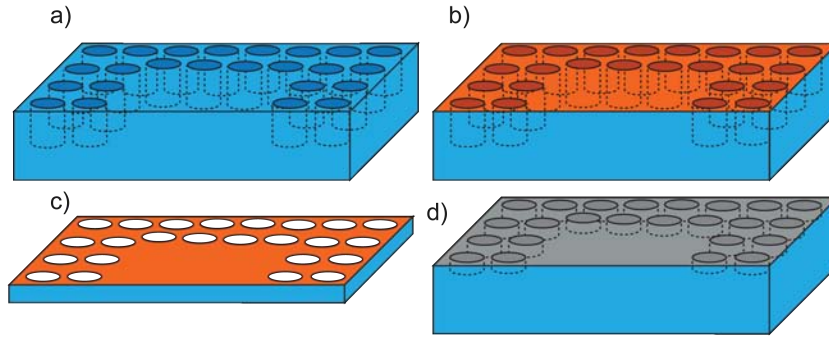


Figure 3.5: Overview of templates for multiple bond testing: (a) Si die with Bosch-etched pad-location layout serves as basis for further template designs (b) Template 1: template coated with solderable Cu surface (c) Template 2: template thinned to have through holes (d) Template 3: Si template with shallow holes coated with SnAg diffusion solder.

- Ideally, a layout – independent template should be designed (i.e. should be flexible for ball bond position/technology)

Three template types are presented, where a 600 μm thick Si wafer builds the base material. Adapted in-line lithography technologies are used to pattern the Si template to a desired layout. 100 μm deep holes are Bosch-etched into the Si template ensuring that each ball bond can be threaded in a corresponding hole, such that each nailhead is isolated from its counterparts and soldering can occur separately. Therefore the imid mask layout is used, resulting in octagonal holes of a diameter of 100 μm , equivalent to the dimension and location of the bonding pad. It can be distinguished between three templates, which are depicted in Fig. 3.5.

The template designs and presumable usage are described hereafter:

Template 1

100 μm deep holes are Bosch etched into the 600 μm thick Si template. To ensure a strong adhesion between the prospectively applied solder paste and walls of the template, a Cu layer, which is easy to solder, is sputter deposited to coat the walls of the etched holes. A tungsten interlayer establishes a strong adhesion between silicon and copper. The deposited Cu layer serves as a guide and fixture of the solder paste, which will be applied to grip the Cu ball bonds and supposedly enhances uniform soldering of each ball bond. Due to manufacturing reasons the top side of the template is also coated with copper and can be easily removed by manually

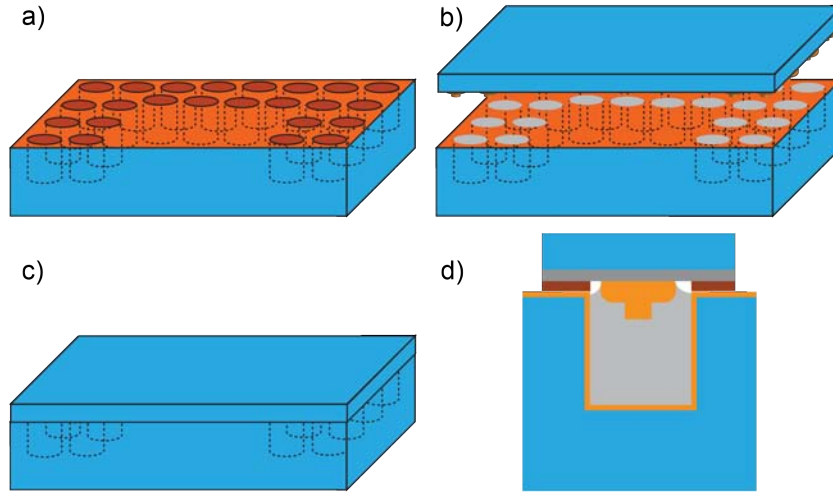


Figure 3.6: Usage of Template 1: (a) overview of bare template; (b) template filled with solder paste and chip facing setup upside down; (c) soldered template-chip-sandwich; (d) cross section of soldered ball bond.

polishing the top face of the template. The holes are filled with a $\text{Pb}_{37}\text{Sn}_{63}$ solder paste. A flat and equal amount of solder per hole is ensured by striping off residual paste with a miniaturized spatula tool. Prior to reflow soldering the chip-template combination, the ball bonds are cleaned and prepared analogously to section 3.2.1. Finally, the chip is mounted to the solder template such that the ball bonds face the holes filled with $\text{Pb}_{37}\text{Sn}_{63}$ solder. Reflow soldering of the template-chip-sandwich is realized on a hot plate, where the setup is heated from the bottom leading to a fast (i.e. less than a minute) reflow soldering procedure. Finally, the soldered specimen is cleaned with ethanol and blow dried to remove potential flux residuals. The main steps of this template application are sketched in Fig. 3.6.

Template 2

Similar to the sample preparation procedure for multiple ball bond testing described in 3.2.2 the perforated holes of the thin template 2 serve as guide for a prospectively applied solder paste to connect the Cu ball bonds without wetting the underlying pad metallization. Template 2 is a derivative of template 1 but thinned down to a total thickness of $80\text{ }\mu\text{m}$ such that the holes are through.

In this setup the template is placed on top of the chip such that the ball bonds are threaded through each hole. Then the solder paste is applied from above and covered with a copper plate to ensure uniform and throughout soldering along the

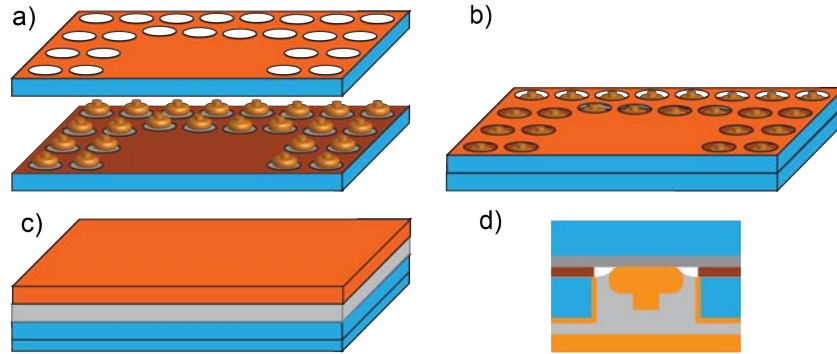


Figure 3.7: Usage of template 2: position template above chip such that Cu side faces upwards (a and b); add solder paste layer and copper plate (c); cross section of soldered chip (d).

Cu coated walls of the template up to the Cu ball bond surface. The soldering and post-soldering procedures are the same as in section 3.2.2. The main steps of the sample preparation with this template are illustrated in Fig. 3.7.

Template 3

Here, a 600 μm Si template with shallow holes is utilized, where its surface is coated with a low melting SnAg diffusion solder layer. After a preparation and cleaning procedure as mentioned in 3.2.2 the chip is positioned upside down on top of the template, where each ball bond is located in a shallow hole. The soldering occurs similarly to previously described sample preparations (see 3.2.2) except that once the solder layer melts, the chip is carefully pressed into the molten solder layer such that capillary effects force the solder to rise and to strongly embed the Cu ball. Afterwards the sample is immediately removed from the hot plate allowing the solder to solidify; a subsequent cleaning procedure is conducted to remove redundant flux (see 3.2.2). A schematic of this solution is shown in Fig. 3.8.

The realization of the above mentioned sample preparation techniques turned out to be tedious and difficult to perform manually. The most promising method was found to be the soldering method with template 3 as described in 3.2.2. The main advantage is the already present diffusion solder layer. Furthermore, upside down positioning of the chip such that each nailhead faces the shallow hole of the template can be easily and rapidly performed manually. In Fig. 3.9 the cross section of a prepared specimen is depicted, where a strong soldering of several ball bonds to the template can be shown. A third fatigue measurement series “MR3” was conducted

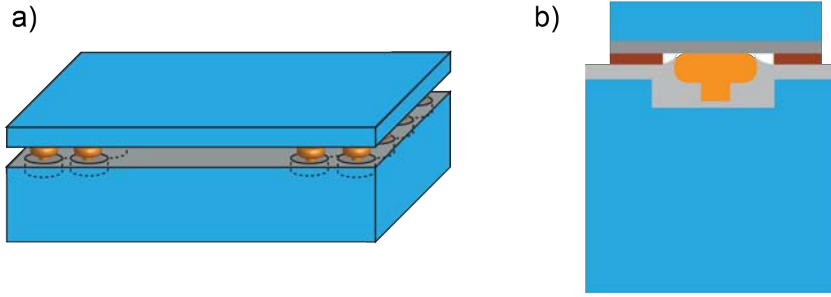


Figure 3.8: Usage of template 3: (a) Position chip on template with ball bonds facing shallow holes; cross section of soldered ball bond (b).

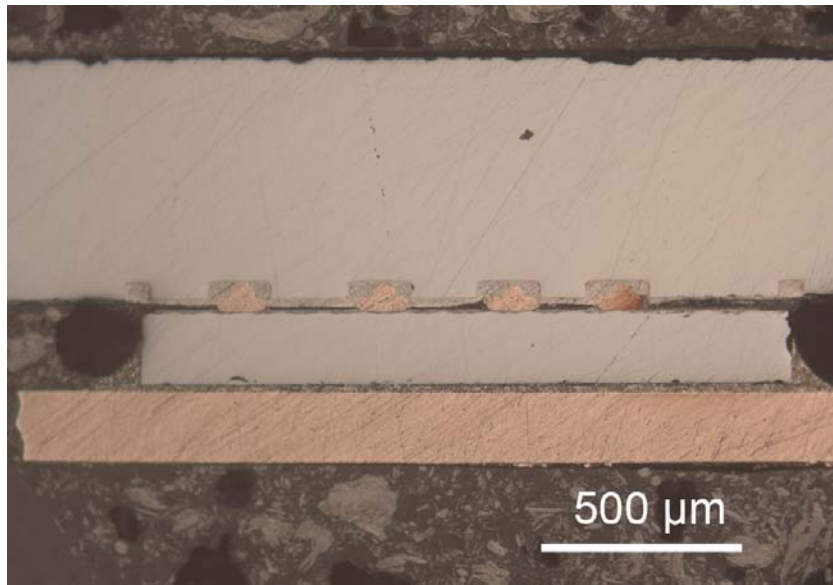


Figure 3.9: Cross section of ball bond sample soldered to Template 3.

with this sample preparation technique. The fatigue data is presented in 3.2.3.

Layout independent template

The main limitation of above described soldering templates is the layout dependency: The designed templates can only be applied to a specific technology. Furthermore, since the imid mask pattern cannot be flipped the holes are etched on the same locations as the pad layout, which means that template 1 and template 3 can only be applied to symmetrical chip layouts—outlying nailheads need to be removed or excluded from the sample preparation.

Thus, a more versatile, layout independent template, which can be applied to sev-

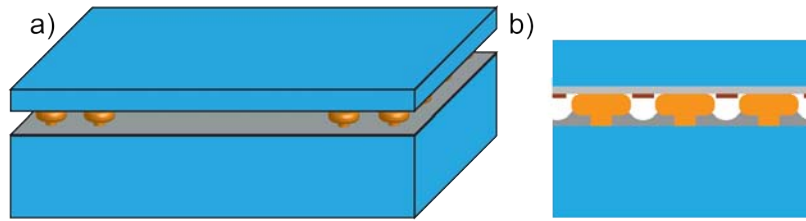


Figure 3.10: Usage of the layout independent template: (a) (Easy) positioning of the chip with nailheads facing SnAg solder (b) Cross section: The solidified meniscus grips each Cu nailhead without covering the pad material.

eral technologies is additionally proposed hereafter. The layout independent template solely consists of a small, flat plate coated with a thin diffusion solder layer. Soldering of the nailheads occurs by positioning the chip upside down such that the nailheads are in intimate contact with the solder layer. During reflow surface tension of the liquefied solder causes creeping of the solder upwards along the Cu nailhead yet not reaching the pad metallization. Hence, the solder solidifies in a meniscus shape surrounding the Cu nailhead and ensuring a strong adhesion between copper and solder. The principle of the specimen preparation with the layout independent template is schematically sketched in Fig. 3.10. Here, a Si wafer material similar to above mentioned templates was employed without previously patterning its surface. A $6\text{ }\mu\text{m}$ thin AuSn layer is deposited on one side of the template. Prior to soldering the chip to the template, the Cu ball bonds are prepared and cleaned analogously to the previously described sample preparation techniques. The fatigue samples are created by means of upside down positioning of the chip such that the nailheads face the solder side of the template. For the reflowing process the chip-template setup is inserted into an industrial diffusion solder furnace, where the temperature and atmosphere program is illustrated in Fig. 3.11. The entire run starting at room temperature back to room temperature only takes about 12 minutes, where the reflowing phase including heating and cooling lasts about 6 min. The peak temperature of $310\text{ }^{\circ}\text{C}$ is only held for one minute. During the reflowing phase formic acid is employed as gentle reducing atmosphere inhibiting oxidation and debris during the soldering process. A cross section of the result is shown in Fig. 3.12.

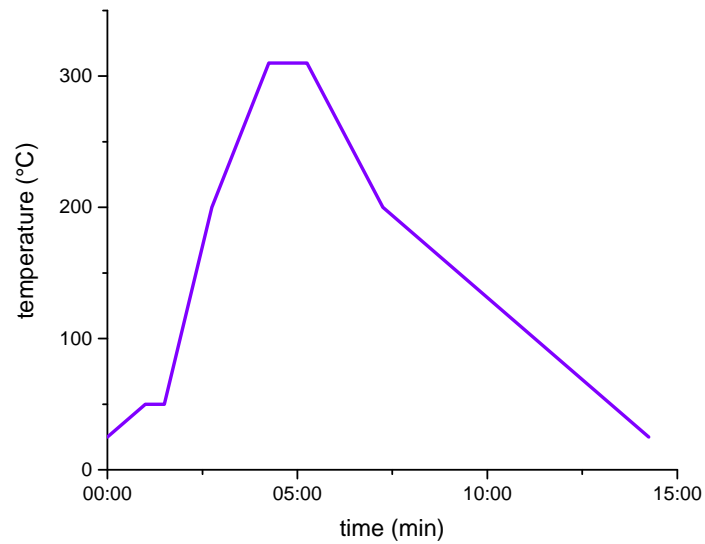


Figure 3.11: Temperature and atmosphere profile for industrial soldering of chip-template pair.

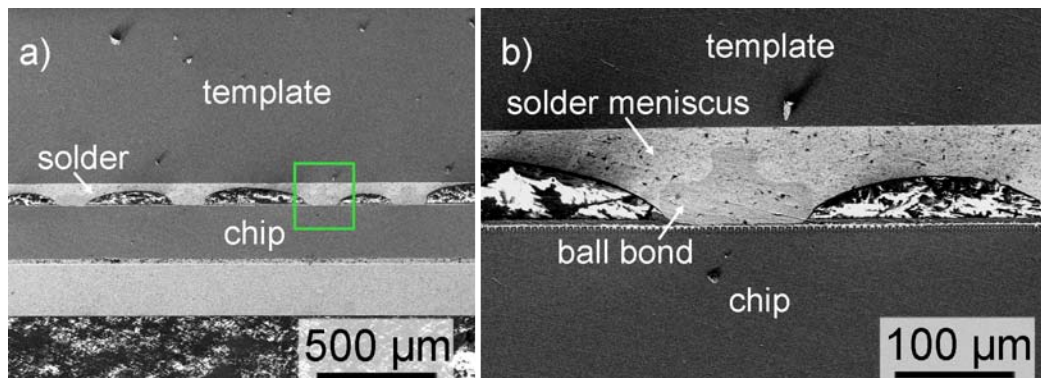


Figure 3.12: Cross section of flat solder template: (a) Overview of several ball bonds soldered in AuSn (b) close up of a soldered ball bond revealing a clear gap between pad metallization and solder.

3.2.3 Comparison of accelerated fatigue test techniques for Cu-Al ball bonds

Fatigue results obtained by the presented fatigue test techniques are compared and discussed hereafter. In total four fatigue measurements series using the four presented sample preparation techniques were conducted on the same Al – Cu ball bond technology in the as-bonded state, where similar fatigue behavior is expected. In total, two generations of single bond test techniques, MR1 and the improved MR2, and two alternative multiple bond test techniques, MR3 and MR4, are suggested.

In the first generation of single bond testing solder balls with a diameter of 600 μm were utilized to increase the active mass of the ball bonds to prepare the ball bonds for fatigue testing for measurement series MR1. Due to encountered difficulties from too big solder bumps, an improved sample preparation technique using smaller solder spheres of a diameter of 400 μm was successfully employed to carry out an improved single bond fatigue measurement series MR2.

Typical fractographs resulting from the single bond fatigue experiments are shown in Fig. 3.13. Regardless whether MR 1 or MR 2 were used, the fracture morphologies in Fig. 3.13a (MR1) and Fig. 3.13b (MR2) are almost identical. In both scenarios, the bond direction is parallel to the loading direction. Thus, due to the aluminum splash in the bond periphery caused by the bonding process, a natural notch is expected forcing crack initiation, followed by crack propagation towards the center of the bond. The crack propagation regime is denoted by a flat morphology with pronounced shear features parallel to the loading direction. Once the crack advances to a critical point, final fracture occurs, as indicated by the elliptical, dimple like morphology in the center of the bond. To confirm that this morphology is purely caused by the loading condition and not by the thermosonic bonding process, one fatigue experiment was carried out with the bond direction perpendicular to the loading direction. The resulting fatigue fracture surface of the pad is depicted in Fig. 3.13c. The elliptical feature attributed to the final fracture and corresponding crack evolution regimes are now rotated by 90° compared to its previous counterparts. Thus, it may be excluded that these fracture morphologies arise from the thermosonic bonding process and can be entirely associated to the loading mode acting on the bond during cycling. This specific fracture evolution may be associated to a pronounced tilting mode due to the high point of gravity in the single bond testing setup. To confirm this assumption, finite element analyses (FEA) were conducted and will be treated in 3.2.4.

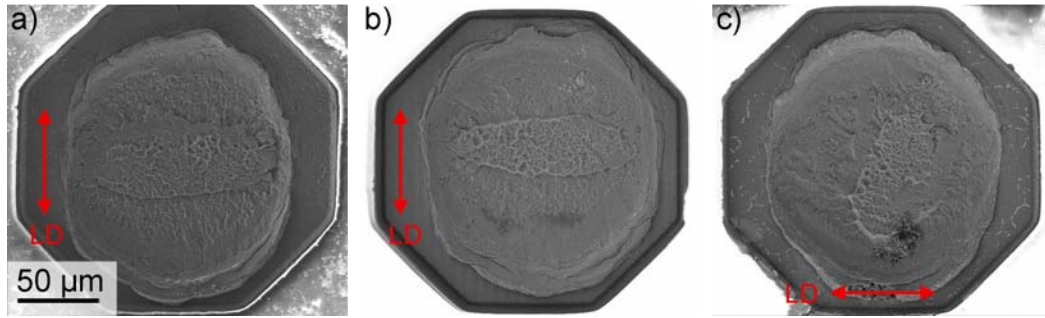


Figure 3.13: Typical fractographs of the fatigued bond pad in dependence of the single bond testing method (a) MR1; (b) MR2; (c) fatigued pad with MR1 with perpendicular loading direction. All images are oriented parallel to the original bond direction, the loading directions (LD) in each image are indicated by the arrow.

For the multiple bond test series the most suitable soldering templates presented in section 3.2.2 were chosen. In MR3 a layout dependent SnAg template (see template 3 in 3.2.2) was used and in MR4 the layout independent flat AuSn template was utilized.

The fatigue measurement series were conducted on as-bonded Al-Cu bonds of the same technology featuring similar bond quality. Fig. 3.14 and Fig. 3.15 show the typical fatigue fractographs obtained by method MR3 and MR4, respectively. The fatigue fracture morphologies obtained by multiple bond testing slightly differ from the typical morphologies from single bond testing: The elliptical feature in the center of the bond as observed for single bond testing is absent. Here, the obtained fracture surface is denoted by a homogeneously smeared, shearing morphology of the aluminum pad. The shear features are oriented parallel to the loading direction. On the corresponding copper wire side, where the copper ball is still strongly attached to the soldered templates, complementary aluminum residuals are located on the bottom of the bond.

The fatigue data of the four measurement series is summarized in Fig. 3.16, where the average shear stress τ estimated by equation 2.25 is plotted against the number of loading cycles to failure N_f . The dashed lines in the plot serves as guide for the eye.

As can be seen, the obtained fatigue data highly differs among the corresponding test techniques even though the bond quality should be identical. In the case of single bond test techniques a data shift of about 40 % is observed. In MR1 the average stresses range from 25 MPa to 15 MPa between 10^5 and 10^9 loading cycles, whereas

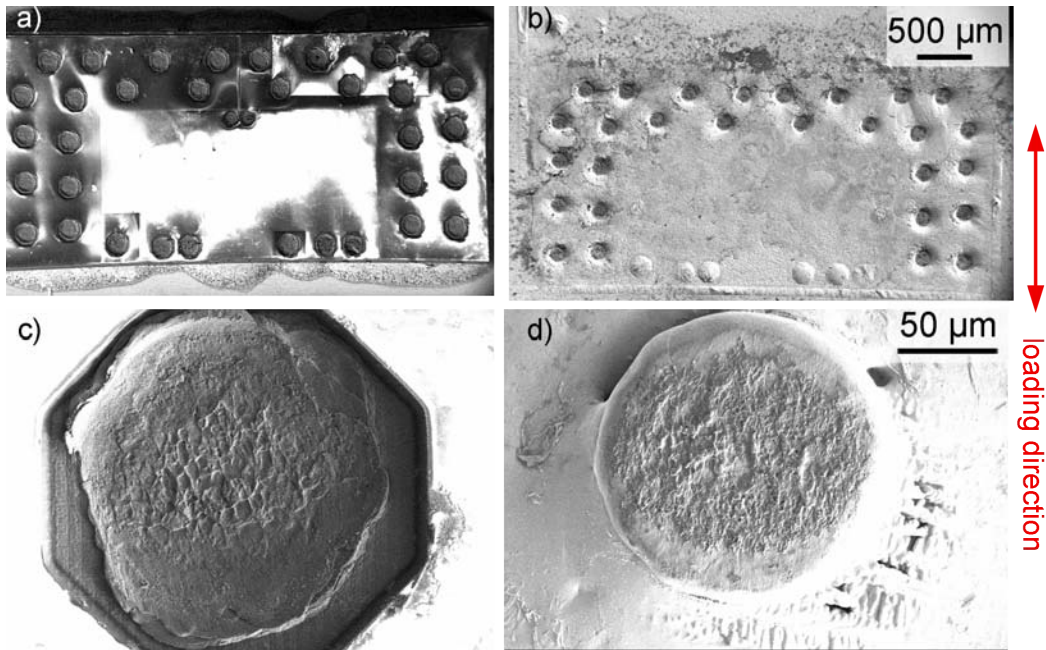


Figure 3.14: Fatigued specimen with method MR3: (a) chip side showing removed ball bonds (b) template side: all ball bonds are embedded in solder template (c) close up of fatigued aluminum pad (d) corresponding fatigued copper ball.

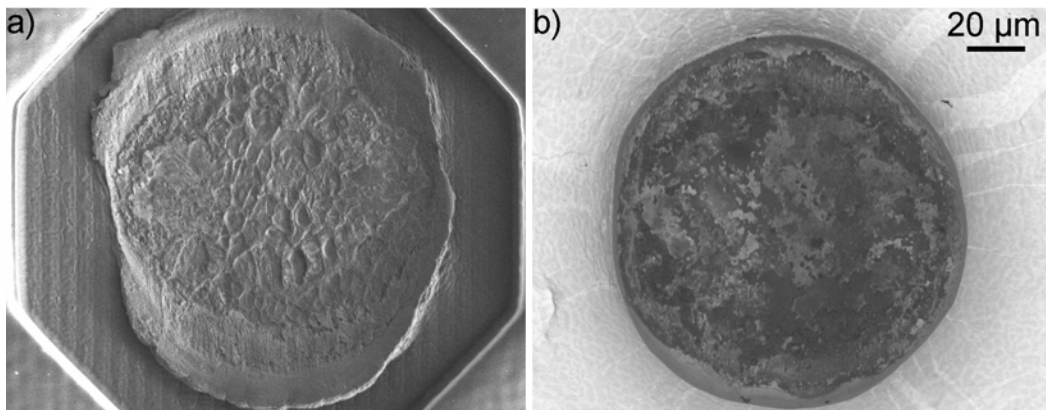


Figure 3.15: Fatigued specimen with method MR4: (a) close up of fatigued aluminum pad and (b) corresponding fatigued copper ball.

in MR2 average stress values between 14 MPa and 11 MPa already lead to fatigue lift-off in the same range of applied loading cycles. A higher scatter of the data in MR1 can be observed compared to the data in MR2, which may be explained by the fact that in MR1 the bigger solder ball may slightly adhere to the underlying pad metallization. Therefore, the fatigue results may be falsified (due to an artificial increase of the bond area) and moreover not be reproducible. Fig. 3.4 compares the cross sections of the single bond fatigue test specimens, where Fig. 3.4a shows the solder-jetted sample with solder ball diameter of 600 μm employed in MR1. Fig. 3.4b shows its improved counterpart with a smaller solder bump of 400 μm diameter. It can be seen that due to the flat geometry in Fig. 3.4a, where the solder bump almost reaches the pad metallization and the chip, whereas in Fig. 3.4b the solder ball is clearly does not contact the chip nor the metallization. This also leads to a higher location of the center of gravity resulting in an increased tilting mode during the to and fro excitation of the ultrasonic resonance setup. In this case, the solder ball acts as a lever on the bond interface, which explains the lower stress amount necessary to rupture the bond. In contrast, the flat, loaf-shaped solder bump-ball bond-geometry in MR1 leads to an elevated shear loading mode, which explains the higher stress values required for bond fatigue fracture.

The multiple bond test techniques reveal an even higher data offset relative to each other: In MR3 the fatigue data ranges from 35 MPa to 25 MPa, whereas in MR4 the fatigue data lies between 11 MPa and 5 MPa. The discrepancy of both datasets may be explained by the difference of the employed solder material. In MR3 a SnAg diffusion solder with a melting point of 220 $^{\circ}\text{C}$ was employed. The soldering procedure only lasts less than one minute whereas in MR4 AuSn with a melting point of 280 $^{\circ}\text{C}$ was used. Furthermore, during the soldering procedure the samples are exposed to elevated temperatures above 200 $^{\circ}\text{C}$ during 4.5 minutes, whereof 1 minute is held at 310 $^{\circ}\text{C}$. This leads to thermo-mechanically induced stresses and may cause pre-straining of the sample weakening the bond prior to fatigue testing.

3.2.4 Finite element (FE) analyses of MR1 –MR4

To gain a deeper understanding on the presented fatigue test techniques and fatigue life results of the investigated Al-Cu bonds, additional finite element (FE) calculations were conducted to elucidate the following questions:

- How does solidification of the soldered template-chip sandwich affect the bond

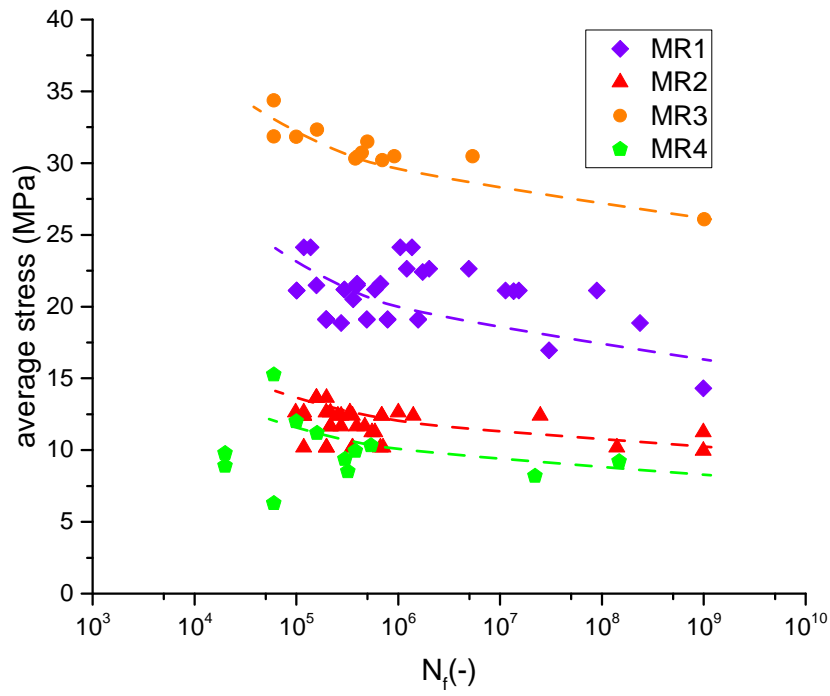


Figure 3.16: Comparison of fatigue data obtained by different measuring techniques, the dashed lines serve as guide for the eye: MR1: single bond testing (solder ball 0.57 mg); MR2: single bond testing (solder ball 0.29 mg), MR3: multiple bond testing (template 3, AgSn diffusion solder); MR: multiple bond testing (Si plate covered with 6 μm thin AuSn diffusion solder).

interface?

- What are the predominant loading modes resulting from the proposed specimen setups in the measurement series MR1 – MR4?

Complementary finite element analyses (FEA) were conducted by Dr. Martin Lederer using the ANSYS code to answer the above mentioned questions. The main findings presented in [Lederer et al., 2015] are briefly summarized in the following section.

Effect of soldering process on the bond interface

Both multiple bond test techniques presented in MR3 and MR4 lead to a similar loading mode. However, a huge discrepancy of the obtained fatigue life curves is observed, although samples of comparable bond qualities were measured. This discrepancy may be attributed to the different solder materials employed, which cause interfacial stresses during the solidification, depending upon the melting point of the used solder material. While SnAg, used in MR3, has a melting point of 220 °C, AuSn melts at 280 °C. Finite element computations were conducted to quantify the permanent stresses at the Al-Cu bond interface caused by the cooling process from the corresponding reflow temperature to room temperature. Thus, the difference of the melting points of both solder materials is taken into account. Additionally, AuSn solder is known as high quality solder, which shows very little to no creep. This implies that stress relaxation of the solder is almost impossible after solidification. This means that soldering with SnAg leads to a very stiff specimen causing plastic strain in the bond interface. The computed plastic strain values after the solidification process are up to 16.7% at the interface, when AuSn was employed. In the case of SnAg solder the residual plastic strain is around 7.1%. Fig. 3.17 illustrates both solidification scenarios, where Fig. 3.17a and b show the permanent plastic strain for the setup soldered with AgSn and AuSn, respectively. Fig. 3.17c and d show a cross section of the soldered templates revealing the von Mises stress distribution in the SnAg template and AuSn template, respectively.

Comparison of FE-computed von Mises stress: analysis of single vs. multiple bond test setup

In Fig. 3.16 the fatigue data is expressed by the analytically obtained average stress, which is only a rough estimate, but the only possibility to determine the

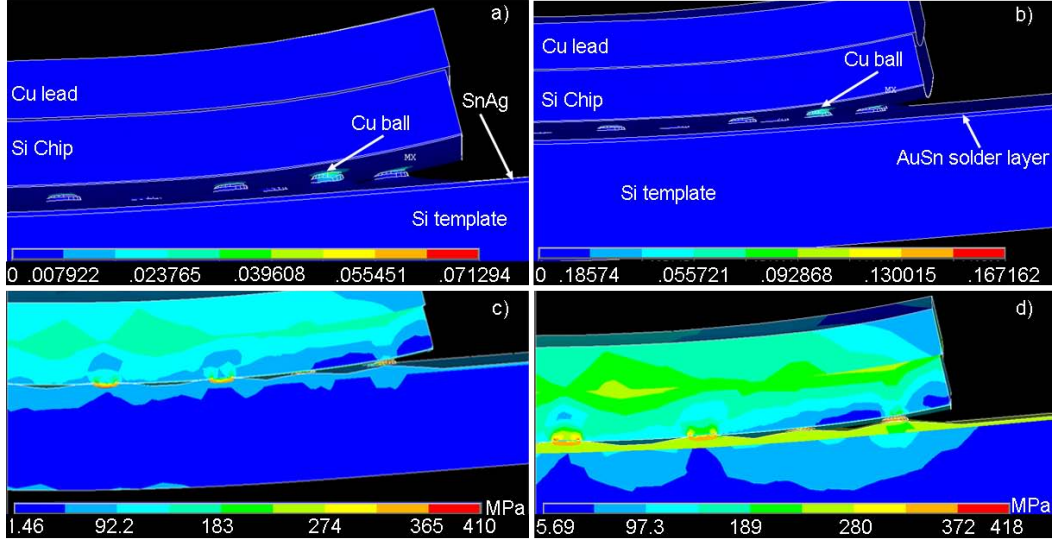


Figure 3.17: FE simulation of induced plastic strains resulting from the solidification of the template-chip assembly for (a) SnAg ($T_{m,SnAg}=220\text{ }^{\circ}\text{C}$) and (b) AuSn ($T_{m,AuSn}=280\text{ }^{\circ}\text{C}$). The von Mises stress distribution is shown in the cross sectional plots, where (c) is for SnAg template and (d) for AuSn.

stresses experimentally. The dashed lines for each data set serve as guide for the eye. However, the different loading modes, which have a different impact on the bond interface, are neglected in this representation of the data. Complementary FE computations are necessary to express these complex stress states by an equivalent stress to directly compare both fatigue testing scenarios. Here, the von Mises stress is computed to compare the improved single bond test method (MR2) with the multiple bond test technique using SnAg solder (MR3), where a loading condition extracted from the experimental data in Fig. 3.16 corresponding to the fatigue life of 10^6 cycles for both setups are chosen. A time dependent transient analysis with elasto-plastic material models was computed by means of FE methods. Fig. 3.18 shows the resulting von Mises stress distribution for single (Fig. 3.18a) and multiple bond (Fig. 3.18b), where the time step corresponding to the maximum load is depicted, respectively. The fatigue fracture surfaces reveal in either case – single or multiple bond testing – that the crack evolution solely occurs in the aluminum, which is the softest material compared to copper. Therefore, the von Mises stresses occurring in the aluminum at loading conditions leading to final fracture after 10^6 and 10^8 were computed for the single and multiple bond test setup, basing on the experimental data. The modelled fatigue life curves for both setups are shown

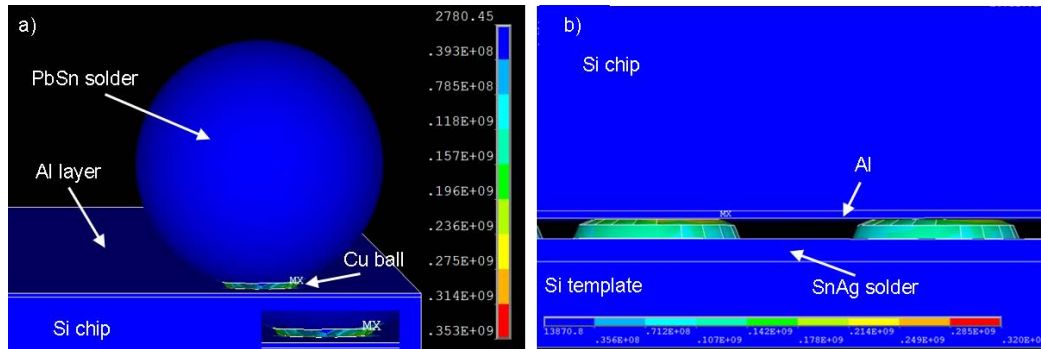


Figure 3.18: FE simulation of von Mises stress distribution of the single bond testing method (a) and multiple bond (b).

in Fig. 3.19. It can be seen that here the equivalent von Mises stress occurring in both bonds with improved fatigue setups are in good agreement. Consequently, the choice of fatigue testing needs to be constant during a measurement series, where several material bond parameters need to be compared.

3.3 Growth kinetics of intermetallic compound formation

In the following section, basing on a study presented in [Pelzer et al., 2012], the aim is to quantify the intermetallic compound growth kinetics of the Al-Cu bond interface of the investigated ball bond technology. The manufacturer has to ascertain reliable bonds corresponding to a heat treatment at 150 °C up to 10 000h. Therefore, accelerated annealing treatments were conducted under inert N₂ atmosphere at elevated temperatures. The as-bonded samples were annealed after a 2 h purging step to ensure a clean atmosphere prior to ramping up the furnace to a desired temperature. After the desired heat treatment the furnace chamber was cooled below 50 °C under inert atmosphere. To ensure a comparable bond quality of the as-bonded step all the samples were taken from one wafer and the same assembly. It is aimed at conducting accelerated heat treatments corresponding to the maximum value at 150 °C during 10 000 h in reasonable time at increased temperatures. Therefore the following annealing treatments were chosen:

- at 175 °C for the annealing times: 50, 100, 200, 300, 500 and 1000 h.
- at 200 °C for the annealing times: 50, 100, 200, 300, 500 and 1000 h.
- at 225 °C for the annealing times: 25, 50, 100, 200, 500 and 1000 h.

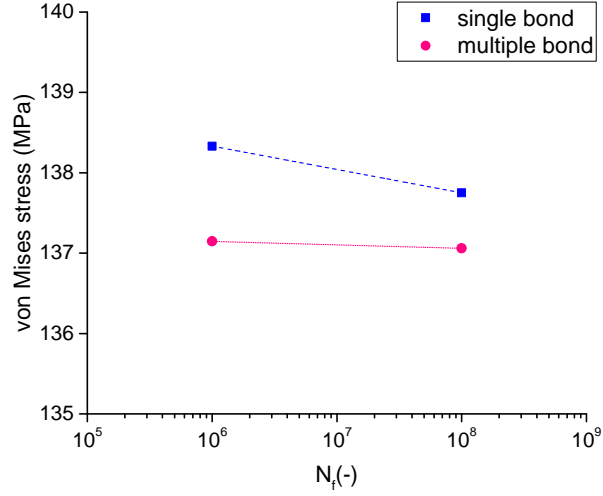


Figure 3.19: Lifetime models of single bond vs. multiple bond fatigue testing expressed by the von Mises stress occurring in aluminum, where fracture occurs.

- at 250 °C for the annealing times: 100, 200, 300, 500 and 1000 h.
- at 300 °C for the annealing times: 50 h.

To measure the total intermetallic stack evolution after the heat treatments the samples were sectioned at the full radius of the bond by means of FIB. Then the evolved intermetallic stack thickness is measured at 10 positions across the bond for each annealing condition. In Fig. 3.20 a bi-logarithmic graph of the experimentally obtained median of the IMC thickness values as a function of the annealing duration at a given temperature is plotted.

An empirical relationship between the IMC growth thickness Δx and annealing time t at a given temperature T can be described by the following equation 3.1:

$$\Delta x = \sqrt{D_0 \cdot \exp\left(\frac{-E_a}{RT}\right) \cdot t} \quad (3.1)$$

where E_a is the activation energy in J/mol, R is the gas constant and D_0 is the diffusion constant. In the bi-logarithmic representation of the data equation 3.1 can be expressed by a linear equation of the type $z = a + bx + cy$ leading to the

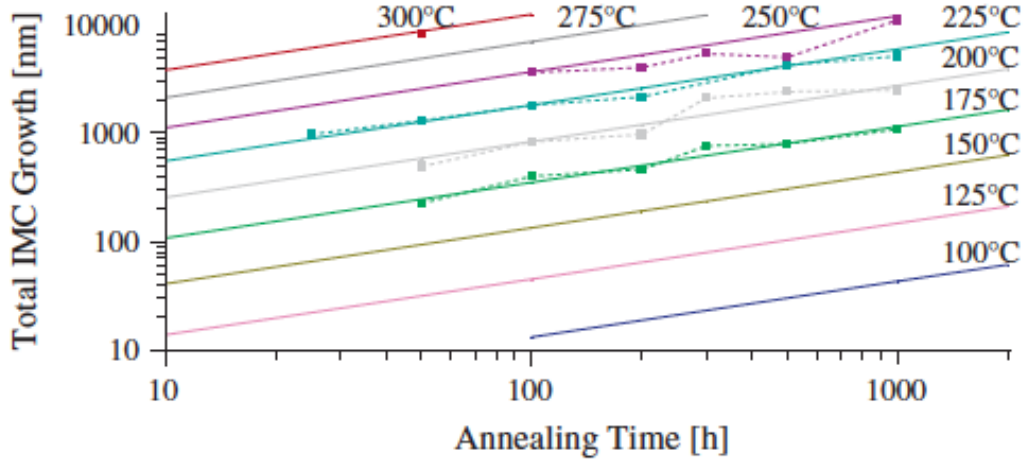


Figure 3.20: Double-logarithmic graph of experimentally obtained IMC thickness vs. annealing duration at different temperatures. Obtained data using the empirical expression in equation 3.3 [Pelzer et al., 2012].

following expression:

$$2 \ln(\Delta x) = \ln(D_0) + \ln(t) - \frac{E_a}{R} \cdot \frac{1}{T} \quad (3.2)$$

With equation 3.2 and the experimentally obtained data summarized in Fig. 3.20 the following fit equation could be calculated for the investigated samples annealed at temperatures between 175 °C and 300 °C:

$$2 \ln(\Delta x) = -10.2[\pm 0.8] + 1.03[\pm 0.04] \cdot \ln(t) - 14650[\pm 400] \cdot \frac{1}{T} \quad (3.3)$$

resulting in an activation energy E_a 1.26 kV (i.e. 121.8 kJ/mol) and a diffusion constant $D_0 = 3.7 \cdot 10^{-5} m^2/s$. Basing on the fit equation in 3.3 the following acceleration with respect to the reference stress temperature T_{ref} of 150 °C can be achieved:

- 175 °C: 7 times
- 200 °C: 39 times
- 225 °C: 180 times
- 250 °C: 750 times

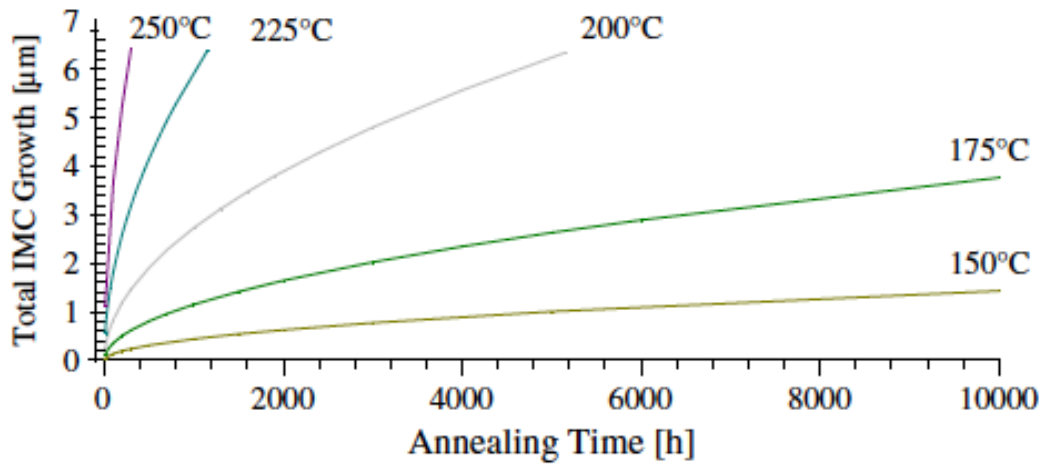


Figure 3.21: Extrapolation of IMC growth according to Arrhenius regression beyond the 1000 h time range basing on the experimental matrix using equation 3.3.

3.4 Effect of microstructural evolution on high cycle fatigue of Al-Cu bonds

One of the main objectives of this study is to reveal the effect of intermetallics formation on the fatigue behavior of the miniaturized Al-Cu interfaces. Therefore the investigated specimens were subjected to isothermal heat treatments to force intermetallics formation at the bond interface. High cycle fatigue tests were conducted by means of the improved single bond test technique (see 3.2.1). Three microstructural states of Al-Cu ball bonds were chosen. This section is structured as follows:

In the first part the microstructural evolution subsequent to high temperature exposure is characterized by electron microscopy (see 3.4.1), where scanning and transmission electron microscopy is employed. Then in 3.4.2 the fatigue data are presented followed by a detailed investigation of the crack path to reveal the involved mechanisms during the fatigue experiment (see 3.4.3).

3.4.1 Microstructural evolution of Al-Cu ball bond

During service microelectronic devices are subjected to elevated temperatures leading to microstructural changes at the bond interface. In the case of bimetallic Cu-Al bonds marked interdiffusion among the parent materials occurs leading to the formation of intermetallic compounds. Heat treatments were conducted to study the

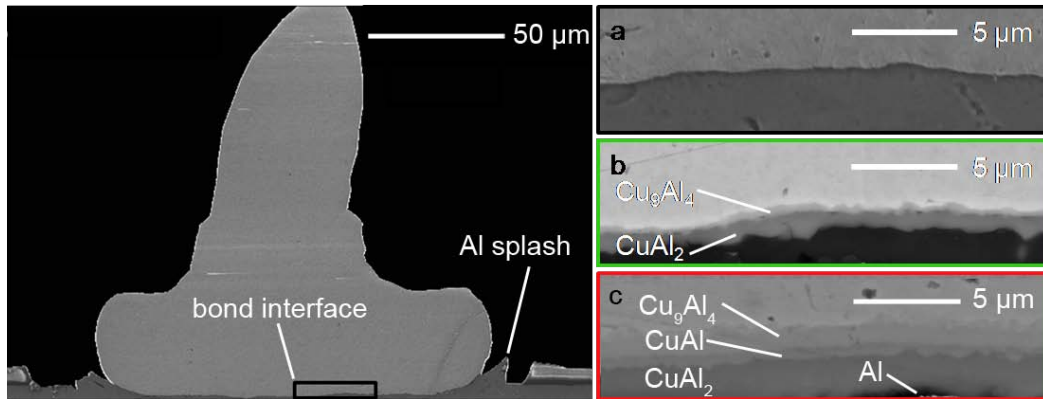


Figure 3.22: SEM Cross section of investigated ball bond specimen with close-up of interfacial evolution of three investigated states (a) as-bonded state, (b) 200 °C 200 h, (c) 200 °C 2000 h.[Lassnig et al., 2015].

microstructural evolution of Cu-Al bonds, which are representative for intermediate and highly aged conditions compared to the end of life state after 10000 service hours at 150 °C. The following interfacial states were chosen and will be discussed hereafter:

1. as-bonded
2. intermediately aged: high temperature storage at 200 °C for 200 h (under vacuum)
3. highly aged: high temperature storage at 200 °C for 2000 h (under vacuum)

An overview of the evolved interface corresponding to above mentioned states is shown in Fig. 3.22.

In the intermediately aged state (200 °C 200 h) two thin intermetallic compound layers evolved whereas in the highly aged state (200 °C 2000 h) three intermetallics are present. The total stack thickness as a function of storage time at given temperature are in agreement with a previous study about the intermetallic compound formation kinetics of annealed Cu-Al ball bonds in [Pelzer et al., 2012]. A total IMC stack of approximately 1.4 µm after 200 h and 3.9 µm after 2000 h at 200 °C are measured. To avoid oxidation during the isothermal heat treatments, the specimens were annealed in evacuated quartz tubes. The intermetallic compounds were measured via SEM EDX and could be identified as Al_2Cu and Al_4Cu_9 present in the intermediately aged state. Additionally, the third intermetallic formed between both adjacent intermetallics in the highly aged state was identified as AlCu .

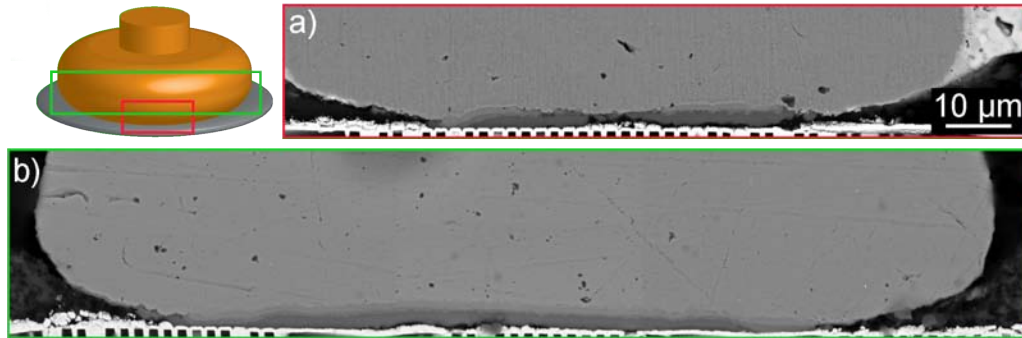


Figure 3.23: SEM Cross section of intermetallic compound evolution in highly aged state after 200 °C 2000 h (a) section from bond periphery (b) section from bond center (same magnification in both micrographs).

While some studies claim that interfacial evolution subsequent to high temperature storage occurs uniformly across the entire bonding area in intermediately aged conditions (e.g. [Pelzer et al., 2012]), a comparison of cross sections at several locations in the highly aged state revealed heterogeneous microstructural evolution: In the center of the bond a throughout interfacial evolution occurs, whereas in the bond periphery inhomogeneous intermetallics formation is observed (see Fig. 3.23): The cross section taken at the bond periphery is characterized by an undulating interface with non-uniform Al consumption (see Fig. 3.23a) as opposed to a transverse cross section taken at the center of the bond revealing uniform, parallel IMC layers and an entire consumption of the aluminum metallization (see Fig. 3.23b).

(S)TEM study of highly aged (200 °C 2000 h) Cu-Al ball bond interface

A more detailed characterization of the highly aged interface was conducted by means of (scanning) transmission electron microscopy ((S)TEM) to determine the formed intermetallic phases and to study the presence of potential voids or microcracks at high resolution. Three TEM lamellae – called lamella 1, 2 and 3 hereafter – were cut by means of focused ion beam (FIB) and taken from the same ball bond aged at 200 °C for 2000 h. Lamella 1 was extracted in the bond periphery, lamellae 2 and 3 were taken from the center of the bond interface. In Fig. 3.24 STEM images of the three lamellae are shown, where Fig. 3.24a-c are high angle annular dark field (HAADF) and Fig. 3.24d-f are the corresponding annular dark field (ADF) images. HAADF gives phase sensitive contrast, where the intensity is directly proportional to the square of the atomic number, thus the brightest region

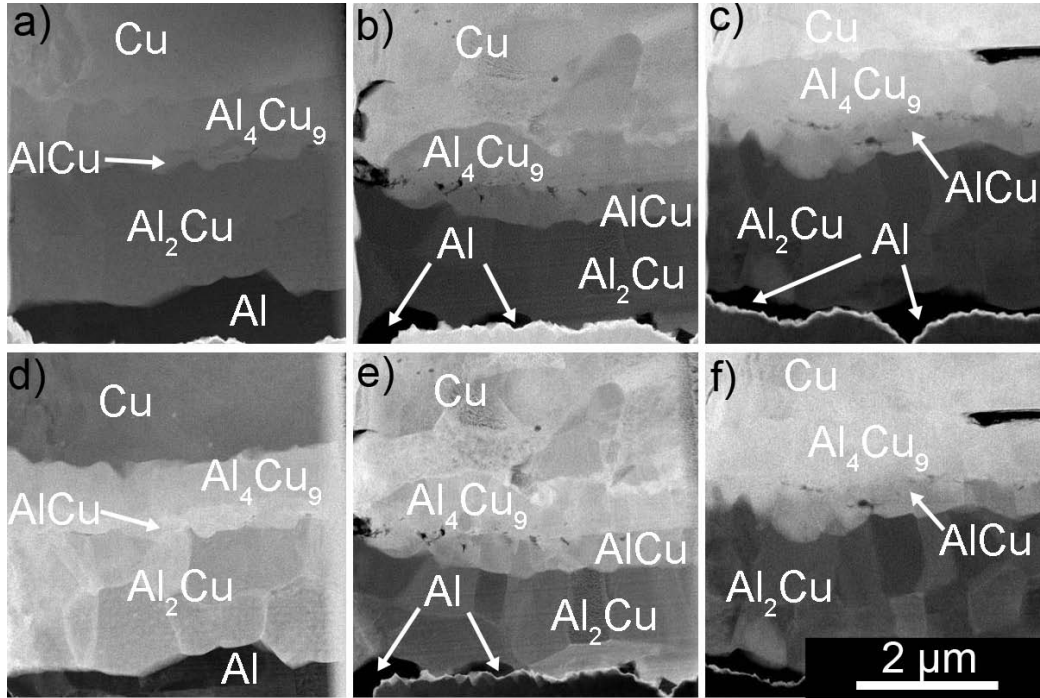


Figure 3.24: STEM images of three FIB lamellae of the highly aged interface (200 °C 2000 h) comparing phase contrast (HAADF) with diffraction contrast (ADF): (a+d) HAADF and corresponding ADF image of lamella 1. (b+e) HAADF and ADF image of lamella 2, (c+f) HAADF and ADF image of lamella 3. [Lassnig et al., 2015].

corresponds to pure copper, whereas the darkest region corresponds to aluminum and the intermetallics are in according greyscales depending on their composition.

A comparison of the three lamellae taken from the same ball bond interface reveals inhomogeneities in void formation and aluminum consumption:

Whereas the aluminum pad metallization is still present in lamella 1, it is almost entirely consumed in lamella 2 and 3. On the other hand, void formation is clearly visible in the latter whereas no voids could be detected in lamella 1. Especially lamella 2 is denoted of marked void agglomeration between two intermetallic compound layers. To identify the intermetallic compound layers quantitative elemental maps were recorded followed by diffraction patterns to reveal their corresponding crystal structure.

In Fig. 3.25 an EDX (energy dispersive X-ray spectroscopy) elemental map of lamella 1 reveals 5 different material layers along the bond interface aged at 200 °C for 2000 h, the results from the 5 material layers are shown in Tab. 3.2,

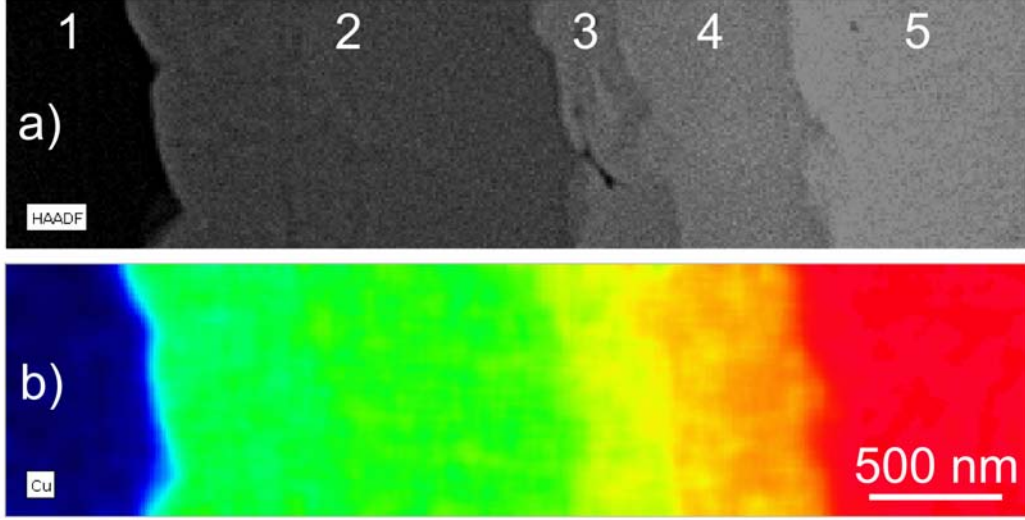


Figure 3.25: Elemental map of highly aged (200 °C 2000 h) Cu-Al ball bond interface: a) HAADF image b) Al distribution c) Cu distribution revealing 5 distinct materials: aluminum (1), Al-Cu intermetallic compounds (2-4) and Cu (5); see Tab. 3.1 for detailed analyses.[Lassnig et al., 2015].

where the measured values are mass percent of the corresponding materials. It has to be noted that further materials have been omitted in this study and thus the atomic percent are restricted to copper and aluminum. Atomic percent of the material i of the EDX results were obtained by means of the following equation 3.4:

$$x_i = \frac{\frac{w_i}{a_i}}{\frac{w_{Al}}{a_{Al}} + \frac{w_{Cu}}{a_{Cu}}} \quad (3.4)$$

where x_i denotes the atomic percent of material i , w_i denotes the mass percent and a_i its atomic weight, where i can be either aluminum or copper. The atomic mass for aluminum a_{Al} is 26.98 u and for copper a_{Cu} is 63.54 u.

3.4.2 Fatigue results

The S-N data is summarized in Fig. 3.26 and is expressed by the experimentally obtained average shear stress amplitude (according to equation 2.25) as a function of loading cycles to failure N_f , where fatigue lift off occurs. In the as-bonded state the fatigue data ranges from about 14 MPa to 11 MPa along 10^5 to 10^8 loading

Table 3.1: Quantitative EDX map results of highly aged (200 °C 2000 h) Cu-Al bond interface. For the corresponding region compare with lamella in Fig. 3.25.

region	Al measured mass %	Cu measured mass %	Al calculated at. %	Cu calculated at. %	comp. lit. [Kouters et al., 2013] Cu at. %	material
1	94	6	97	3	0-2.84	aluminum
2	45	55	65	35	32-33	Al ₂ Cu
3	29	71	50	50	50-52	AlCu
4	17	83	33	67	63-69	Al ₄ Cu ₉
5	2	98	4	96	80-100	copper

cycles. Runouts, that is, bond specimens without fatigue failure up to 10^9 loading cycles- were observed at 9 MPa. In the as-bonded state, the fatigue limit is reached at stress amplitudes below 10 MPa, whereas in the intermediately aged state at 200 °C 200 h a slight downward shift of the fatigue data is observed, ranging from 12 MPa to 8 MPa. It has to be noted that in this state no run outs were measured. In the highly aged condition (200 °C 2000 h) significantly lower fatigue resistance is shown. Here, the data ranges from 10 MPa to 6 MPa at loading cycles to failure ranging again from 10^5 to 10^8 , respectively. It can be shown that the fatigue life drastically decreases when compared to the as-bonded counterpart. In each scenario fatigue tests were conducted such that the loading direction coincides with the direction of the thermosonic bonding process, which is denoted by the orientation of the aluminum splash.

3.4.3 Fatigue fracture morphology

An overview of the characteristic, microstructure dependent fracture surfaces observed after the high cycle fatigue tests of the miniaturized Cu-Al bond interfaces are depicted in Fig. 3.27. The fractographs juxtapose the fracture surfaces of the fatigued pad and corresponding Cu bond bottom revealing typical fracture morphologies and crack orientation, which occurred in the as-bonded, the slightly aged and highly aged states. In all three conditions two different fracture morphologies can be identified and related to characteristic failure which are: (i) crack propagation and (ii) final fracture:

The given bond geometry forces crack initiation at the bond periphery as the notch shaped gap between the Al splash and the Cu ball acts as a stress concentrator (see Fig. 3.22). During cycling, the crack propagates symmetrically from the bond periphery inwards until only a small area remains bonded. Consequently, the resulting stresses according to equation 2.25 become significantly high due to area

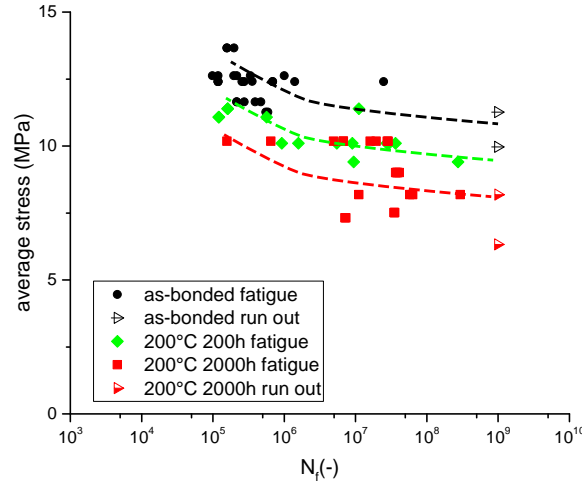


Figure 3.26: Fatigue life curves of Cu-Al ball bonds: applied shear stress $\Delta\tau$ vs. loading cycles to failure N_f . The dashed lines serve as guide for the eye for the fatigue data of each microstructural state.

reduction leading to ultimate –abrupt– fracture. The ultimate fracture regime is characterized by the elliptical feature in the center of the bond, where the short dimension of the ellipse is parallel to the load direction. This regime highly differs in its morphology compared to the crack propagation regime. In the case of intermetallic compound formation, final fracture occurs in a different material than the crack propagation regime.

Both fracture morphologies were observed in the three investigated conditions however the crack path differed depending on the formed intermetallic compounds as well as on the thickness of residual aluminum pad. In the as-bonded state, where the soft and ductile parent materials constitute the bonding interface, crack propagation occurs within the soft Al metallization, whereas final fracture occurs at the bond interface as confirmed by the fractographs of the separated bonding surface in Fig. 3.27a, d since no traces of aluminum are shown on the Cu bottom and no traces of Cu remained on the pad metallization. While the crack propagation regime, going from the bond periphery (aluminum splash) inward (towards the elliptic feature in the center of the bond), is characterized by marked striations parallel to the loading and crack propagation direction, final fracture is characterized by ductile dimples perpendicular to the bond interface and load direction.

Table 3.2: Summary of EDX results of crack path: (ia) crack propagation (ib) crack deflection (ii) final fracture

	200 °C200h	200 °C2000h
	Material (at.% Cu)	Material (at.% Cu)
stage (ia)	Al (1 at.% Cu)	Al (1 at.% Cu)
stage (ib)	-	Al ₄ Cu ₉ (56 at.% Cu)
stage (ii)	Al ₂ Cu (24 at.% Cu)	AlCu (46 at.% Cu)

For the aged specimens SEM-EDX maps of representative fatigued pads were obtained to identify the phases involved in the fracture path, see Fig. 3.28. The data is summarized in table 3.2. A discrepancy between the measured at. % of Cu compared to literature values in 2.1 can be explained by the underlying aluminum-rich material layers leading to an underestimation of the Cu at.%. In the case of intermediately annealed samples (200 °C 200 h) the crack propagation stage occurs in the soft Al pad, since this is the softest material, which is easiest to deform. Crack path deflection in both – as-bonded and slightly annealed states – is similar and is mainly enhanced due to a tilting component during the fatigue test (as previously described in [Lassnig et al., 2013]). It can be assumed that since sufficient Al metallization remains in both conditions, a similar fatigue performance depending on the selected method can be explained. Final fracture however could be identified at the interface between Al and Cu in the as-bonded state, whereas in the intermediately annealed state final fracture occurred In the highly aged state, however, crack propagation occurred in two different materials due to irregular aluminum consumption. Thus, if Al metallization is still present, crack growth occurs through the soft material – analogously to the previous microstructural states. In regions, where Al has been entirely consumed and intermetallics are fully developed, crack is kinked towards Cu for further crack growth. Ultimate fracture could be identified in the third formed intermetallic AlCu, which is hardest but also the least tough material present in this multimaterial system. Since the crack propagation in the highly aged state cannot be predicted in a straightforward way, it follows that the underlying microstructure needs to be taken into account to understand possible crack deflections. Therefore FIB cross sections were realized parallel to the loading direction along the fatigued pad to correlate the EDX measurements and the underlying microstructural evolution with the fracture surface morphologies of the fatigued specimens. Fig. 3.29 confirms previously gained assumptions about the preferential crack paths. Fatigue fracture paths as a function of the microstructural evolution are sketched and summarized in Fig. 3.30.

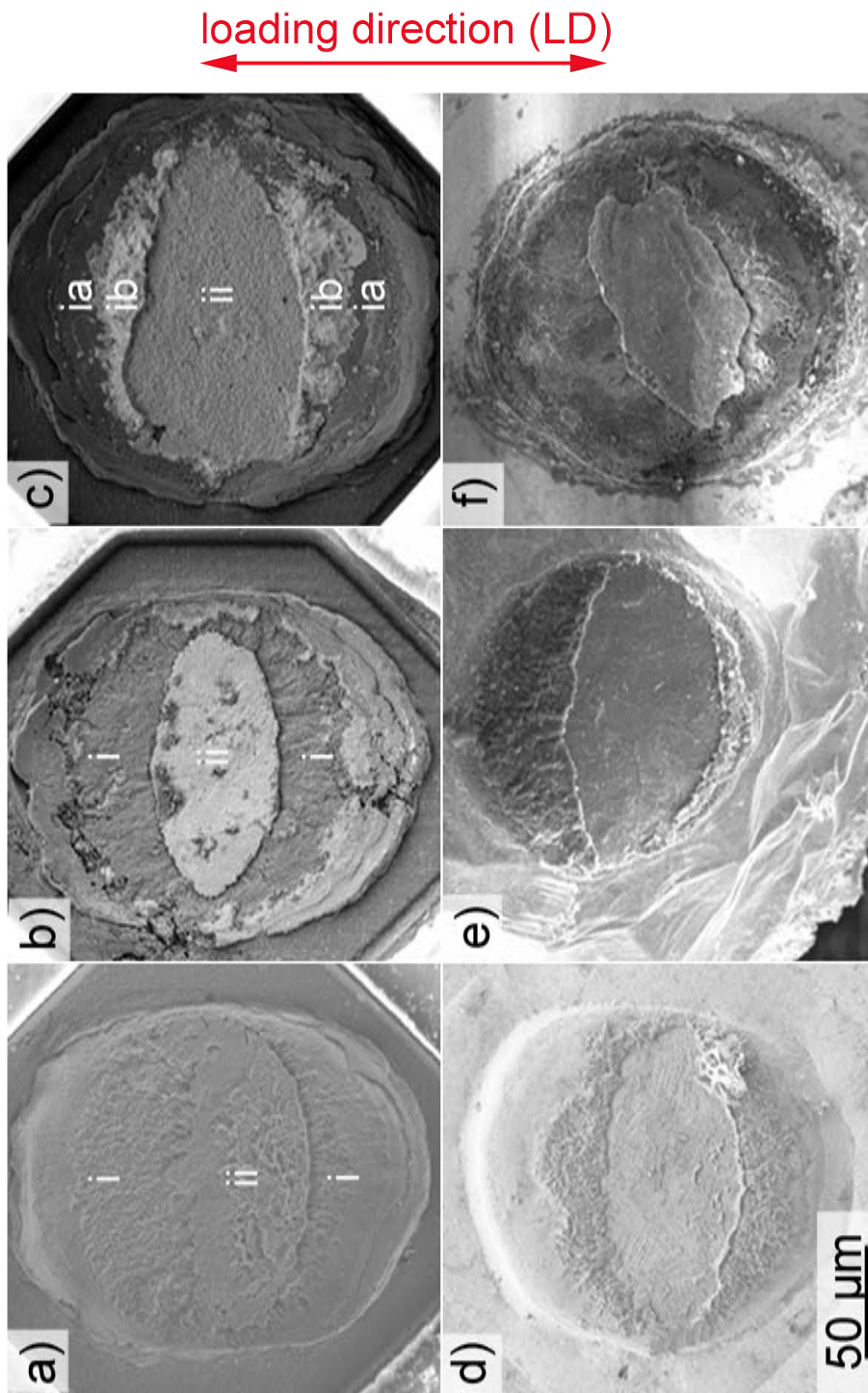


Figure 3.27: Overview of fatigue fractographs for each corresponding microstructure: as-bonded pad (a) with as-bonded Cu bond (d), 200 °C 200 h pad (b) with Cu bond (e), 200 °C 2000 h: pad (c) and Cu bottom (f). [Lassnig et al., 2015].

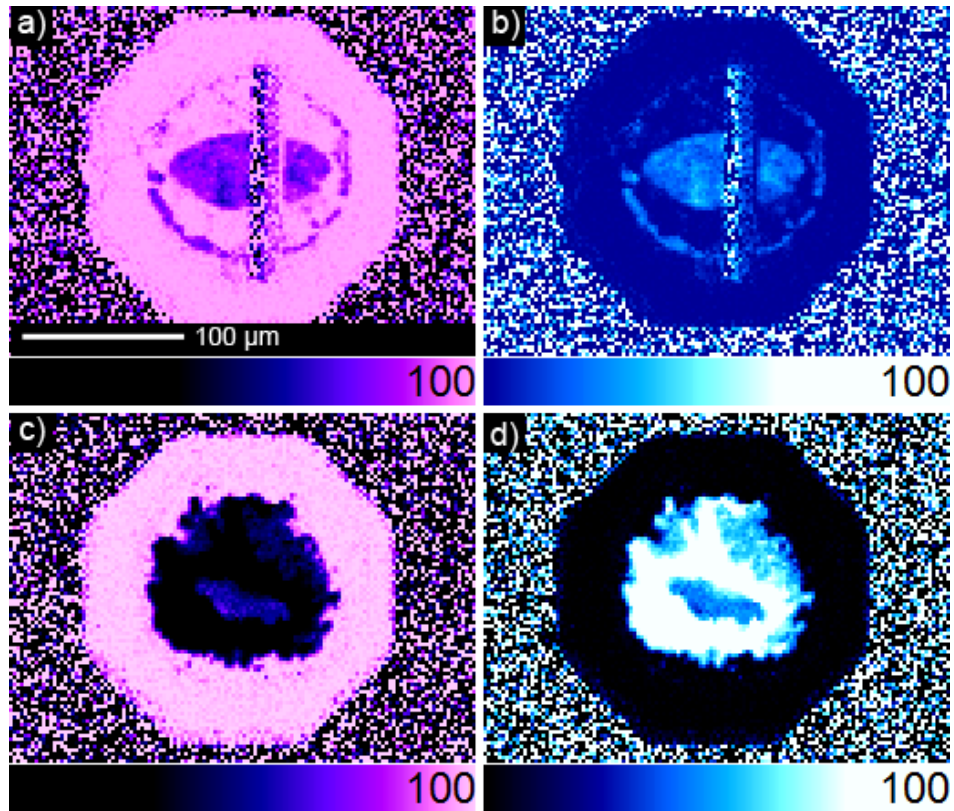


Figure 3.28: EDX maps of fatigued pads in the annealed states: (a-b) correspond to 200 °C / 200 h and (c-d) correspond to 200 °C / 2000 h. Left at. % Al and right at. % Cu. [Lassnig et al., 2015].

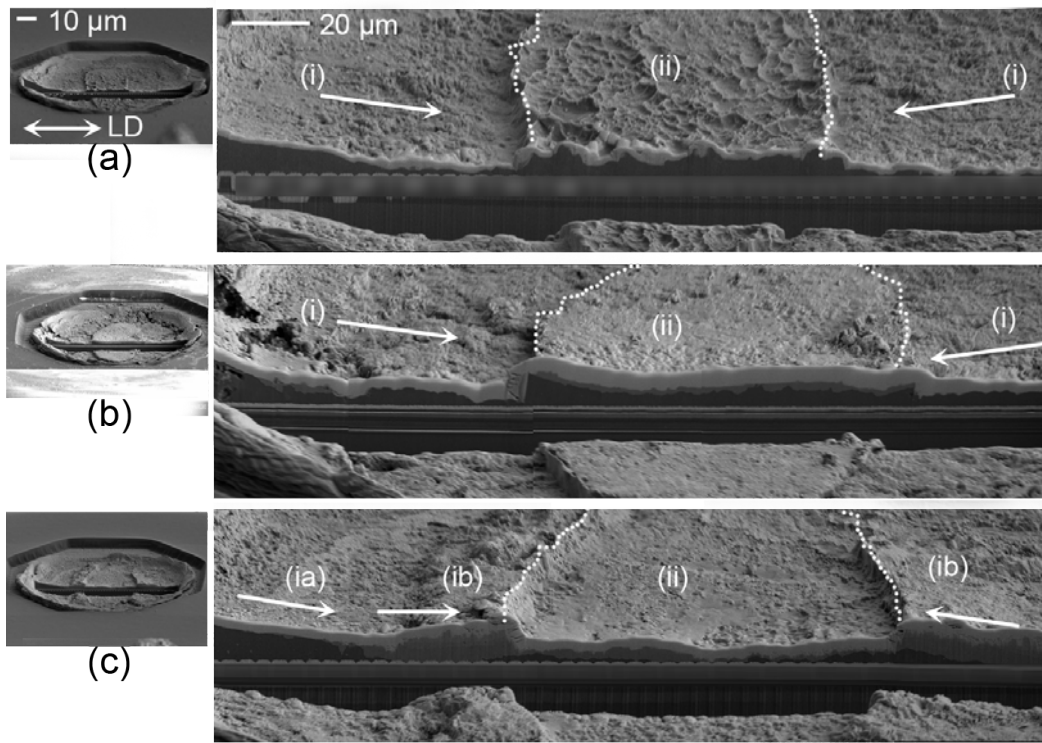


Figure 3.29: FIB cross sections parallel to the bond and load direction (LD) revealing the two states (i) crack propagation (ii) final fracture characteristic for each microstructural state. (a) as-bonded: (i) in Al and (ii) at Al-Cu interface; (b) 200 °C 200 h: (i) in Al and (ii) at the interface between Cu and Al_4Cu_9 ; (c): (ia) in Al followed by crack deflection (ib) at the the interface between Cu and Al_4Cu_9 (ii) AlCu. Note: the three fractographs are coated with Pt! [Lassnig et al., 2015].

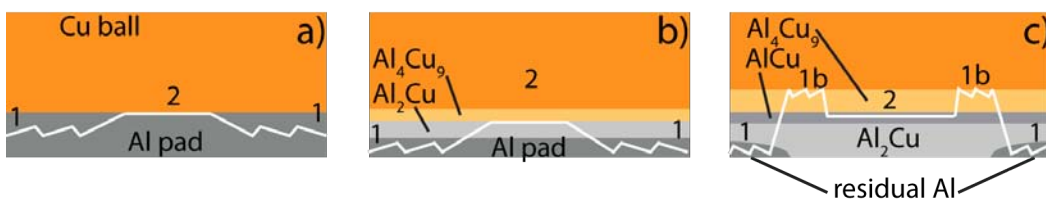


Figure 3.30: Typical fracture of (a) as-bonded (b) 200 °C 200 h (c) 200 °C 2000 h state. In (a) crack propagation (i) occurs in the soft Al until final fracture (ii) occurs at the original Al-Cu bond interface. (b) crack propagation (i) occurs in the Al pad final fracture occurs (ii) at the interface between both intermetallics Al_2Cu and Al_4Cu_9 in (c) crack propagation occurs in Al (ia) once Al is entirely consumed it is deflected into the interface between Cu and Al_4Cu_9 (ib) final fracture occurs in AlCu. [Lassnig et al., 2015].

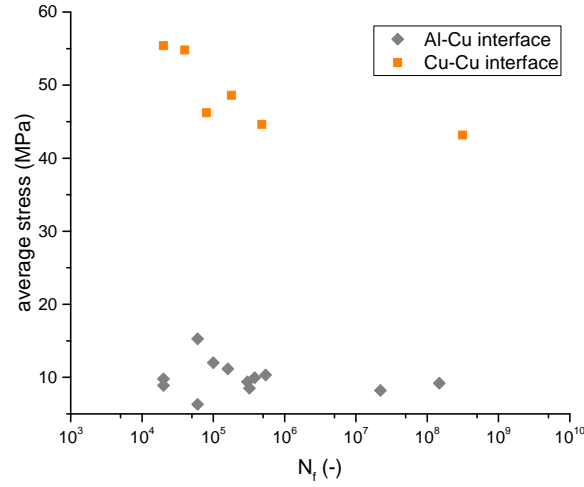


Figure 3.31: Fatigue data of Cu-Cu interface and Al-Cu interface

3.5 High cycle fatigue behavior of Al-Cu vs. Cu-Cu ball bond interfaces

Since the material combination in thermosonic ball bonding is not limited to Cu-Al bonds, novel ball bond technologies with different material combinations are envisioned for future technologies. Recently, ball bonding procedures were adapted to harder material metallizations compared to the relatively soft aluminum pad material. Thus, it is aimed at proving the applicability of above mentioned fatigue test techniques to an arbitrary, solderable metallization material. The fatigue data of two different ball bond techniques, namely Cu-Al and Cu-Cu ball bonds are juxtaposed. Here the layout independent multiple bond specimen preparation technique described in 3.2.2 was utilized. It has to be noted that both ball bond types, Al-Cu and Cu-Cu, are made of the same wire dimensions, resulting in comparable bond dimensions. Thus, both Cu balls were soldered to a layout independent Si template coated with 6 μm AuSn diffusion solder, following the previously described working steps including copper wire removal prior to reflow soldering. The obtained lifetime curves comparing the fatigue of Al-Cu and Cu-Cu bonds are summarized in Fig.3.31, which prove a higher fatigue performance in the case of the novel technology of Cu-Cu bonds.

Typical fatigue fractographs are illustrated in Fig. 3.32 showing that no sol-

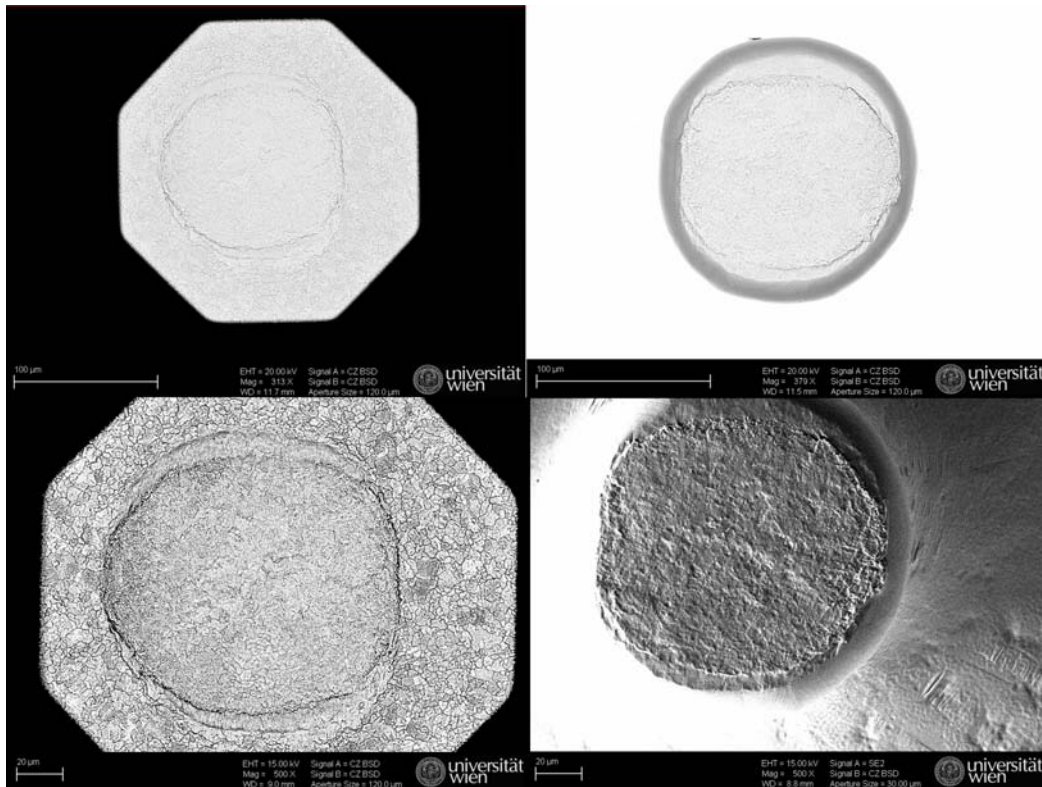


Figure 3.32: Fatigue fractographs of Cu-Cu bond interfaces

der traces were present on the small grained Cu pad. Cu ball bottom reveals pronounced shear features below the Cu ball, which indicates that the fracture occurred along the bond interface.

3.6 Summary

In this chapter the high cycle fatigue properties of miniaturized ball bond interfaces have been discussed, where a novel accelerated mechanical test technique has been introduced. A combination of an ultrasonic resonance fatigue testing system and a specially developed specimen design is employed to obtain lifetime curves of ball bond interfaces when subjected to cyclic shear loading. This test technique is especially designed for miniaturized ball bond specimens and is based on the cyclic induction of shear stresses at the bond interface due to inertia of the setup. In contrast to standardized static test techniques this method is particularly sensitive to interfacial changes like intermetallic compound formation can reveal the weakest

link in a bonding interface.

Two sample setups for accelerated fatigue testing of miniaturized copper-based ball bonds were proposed: single bond and multiple bond testing. Single bond testing allows to assess the fatigue life of each bond individually and is realized by increasing the copper ball with a reflow jetted solder bump without wetting the underlying metallization. Thus, the active mass results in the mass of the solder bump including the mass of the copper nailhead. In the case of multiple bond testing several ball bonds located on one device are tested simultaneously. Here, an upside-down specimen setup is chosen to load the bonding interfaces. Consequently, the chip device is used as an active mass i.e. everything belonging to the chip below the bonding interface. To attach the Cu nailheads to the specimen holder of the ultrasonic resonance system a Si-based template coated with diffusion solder was designed. The Cu balls are directly reflow soldered to the solder side of the template such that a strong adhesion between template and Cu bonds occurs resulting in a template-chip-sandwich setup, where the template is mounted to the sample holder.

The comparability of both specimen setups was demonstrated by means of finite element computations of the von Mises equivalent stress, which occur at the bonding interfaces during the fatigue tests. Whereas experimentally approximated stress ranges differ in both setups where comparable bond qualities were tested, the lifetime curves expressed by the von Mises stress nicely coincide for comparable bond qualities, regardless of the chosen testing setup.

A main aspect of this chapter was to study the interfacial evolution of the Al-Cu bond interface due to high temperature exposure. Selected isothermal heat treatments were conducted to induce interfacial intermetallic compound formation at the Al-Cu interface. Electron microscopic methods confirmed the presence of three intermetallic compounds in the highly aged state (which was obtained at a high temperature exposure at 200 °C for 2000 h) and could be identified as Al_2Cu , AlCu and Al_4Cu_9 . In the intermediately aged state (200 °C for 200 h) only two intermetallic compounds could be found: Al_2Cu and Al_4Cu_9 . While in the case of ball shear tests little conclusion can be drawn from the impact of interfacial evolution on the reliability of the bond interface, the fatigue tests proved a clear degradation with increased intermetallics formation. Characteristic fracture morphologies revealed that two stages occur during the fatigue experiment conducted via the single bond test method: (i) crack propagation followed by (ii) final fracture. The crack

path highly depends on the microstructural evolution of the bond. It is shown that the crack propagates easily through the softest material, final fracture however occurs at the most brittle site.

Finally, the fatigue life of Al-Cu ball bonds was compared to Cu-Cu ball bonds, where it is shown that Cu-Cu interfaces feature a higher fatigue life. While in the as-bonded state in the case of Al-Cu ball bonds the crack initiates and propagates in the soft aluminum metallization, in the case of a copper metallization, the fatigue fracture occurs along the bond interface.

4 High cycle fatigue of bulk Al-Cu interfaces

In the following chapter high cycle fatigue properties of bulk Al-Cu interfaces created by diffusion bonding are studied to compare the fracture behavior with previously investigated miniaturized ball bond specimens. The aim is to obtain the same materials combination including the same intermetallic compounds to mimic the interface of highly aged Al-Cu ball bonds in a bulk testing setup allowing defined loading conditions.

The focus is set on the effect of interface orientation relative to the loading direction to investigate the effect of load mixity on the fatigue behavior of such bond interfaces. Therefore three fatigue measurement series were conducted, where the amount of tensile and shear components are varied. This is achieved by inclining the bonding interface at a predefined angle with respect to the loading direction.

Diffusion bonded specimens are created with optimized bonding parameters to obtain sound diffusion couples, specially designed for ultrasonic fatigue tests. Thus, bonding conditions were optimized (see 4.1) to obtain sound interfaces featuring the same intermetallics occurring in highly aged ball bonds i. e. Al_2Cu , AlCu and Al_4Cu_9 . The obtained microstructure of the fatigue specimens is discussed in 4.1.3 by means of electron microscopical methods in conjunction with nanoindentation measurements to characterize the microstructure and mechanical properties of each present intermetallic compound.

In section 4.2 the fatigue testing setup with emphasis on the specimen design is presented. In the last sections, 4.3 and 4.4 the main results of the conducted fatigue tests including detailed fractographic analyses are presented.

4.1 Diffusion bonding of bulk Al-Cu couples

Specimen preparation of bulk Al-Cu diffusion couples created by diffusion bonding is discussed, where a rationale of the selected bonding parameters is given. Special emphasis is set on the evolved microstructure and morphology of the created Al-Cu interface as a function of the variation of the bonding parameters. Hence,

this section is subdivided into two main parts: In the first part in 4.1.1 preliminary diffusion bond experiments were conducted to assess optimized bonding conditions for the prospective fatigue specimen. The variation of the employed process parameters is juxtaposed in combination with a detailed discussion of the resulting diffusion bonding interface morphologies. In the second part in 4.1.3 a detailed microstructural characterization of the fatigue interface is given. Finally, isothermal heat treatments were conducted to entirely consume aluminum and to conduct a second fatigue series to study the fatigue initiation when aluminum is entirely consumed.

4.1.1 Influence of process parameters on diffusion bonded specimens

According to e.g. [Kazakov, 1985] or [Bauer and Lessmann, 1976] the quality of a diffusion bond depends on the following process parameters:

The applied pressure should ensure a tight contact between the faying surfaces aiding the deformation of surface asperities. Additionally, the applied load should be high enough to avoid unbonded regions within the bond [Kazakov, 1985].

The process temperature should typically correspond to a homologous temperature of 50% to 70% of the melting point of the most fusible material. In a study by Lee and co-authors Cu-Al bonds created by vacuum hot pressing was conducted at temperatures ranging from 623 K to 923 K [Lee and Kwon, 2013]. In the current investigation higher temperatures are chosen.

The duration of the bonding process should typically be kept minimal to inhibit the extensive formation of brittle intermetallic compounds. On the other hand the bonding duration should be long enough to allow diffusion processes to occur. In this study, however, we want to achieve a microstructural state, where bulk intermetallics are fully developed.

An excellent surface condition of the faying surfaces is crucial for a high quality of the bond. First, the surfaces must be degreased and in clean condition. Another important parameter is the surface roughness, which highly dictates the progression of the bonding process. Orhan et al. claim in [Orhan et al., 1999] that an increased surface roughness necessitates an increased diffusion bonding process duration. In [Zuruzi et al., 1999], however, it is shown that an increased surface roughness is beneficial to obtain a sound bond interface.

Preliminary experiments were conducted on aluminum copper pairs to find the optimum process parameters, followed by a metallographic inspection of the resulting bond. Diffusion bonding occurs by joining two small cylindric specimens machined from high purity aluminum (99.999%) and copper (99.99%).

For the diffusion bonding process a “mini hot press”-furnace equipped with a load ram is used in combination with a constraining device specially designed to prevent both bonding materials from early creeping during the process. The “mini hot press”-furnace and the constraining device are depicted in Fig. 4.1a, where the functional principle of the device is illustrated in Fig. 4.1b. The device contains a thick walled hollow graphite cylinder with a machined hole of the same diameter as the diffusion couple. In its center a hole of the same diameter as the diffusion couple was machined such that the samples can be threaded into the cylinder.

To be able to apply the desired load perpendicular to the prospective bonding interface, two graphite rods of the same diameter are inserted on both sides of the diffusion couple and act like a piston. With this setup the original shape of the parent materials can be maintained throughout the bond process.

Depending on the process requirements, the furnace can be run under various atmospheres. To maintain optimum surface conditions and to prevent from process-induced oxidation and debris of the diffusion couple the furnace chamber is constantly purged with reducing atmosphere consisting of 95% argon and 5 % hydrogen.

The preliminary diffusion bonding experiments are listed in table 4.1, summarizing the employed bonding parameters per run. The temperature profiles used for the diffusion bonding experiments can be subdivided into two or three sections. In the first stage, the furnace is slowly heated up to 50 °C to ensure that the heating elements and further components are in equilibrium and to have a defined and reproducible initial state. In the second stage, the chamber is heated to the desired peak temperature, which is held for several hours. This is the stage, where the actual bonding occurs. The dwelling time is varied across the diffusion experiments and applied loads are varied during the experiments. Finally, a third stage is introduced, where the setup is slowly cooled down to 200 °C to ensure equilibrium conditions and to ensure that stresses due to a change of temperature in the created bond containing several intermetallic compounds with different coefficients of thermal expansion. In this stage the load is also released to allow the bond to cool down in a relaxed state. Finally, after the run is finished, rapid cooling is enhanced

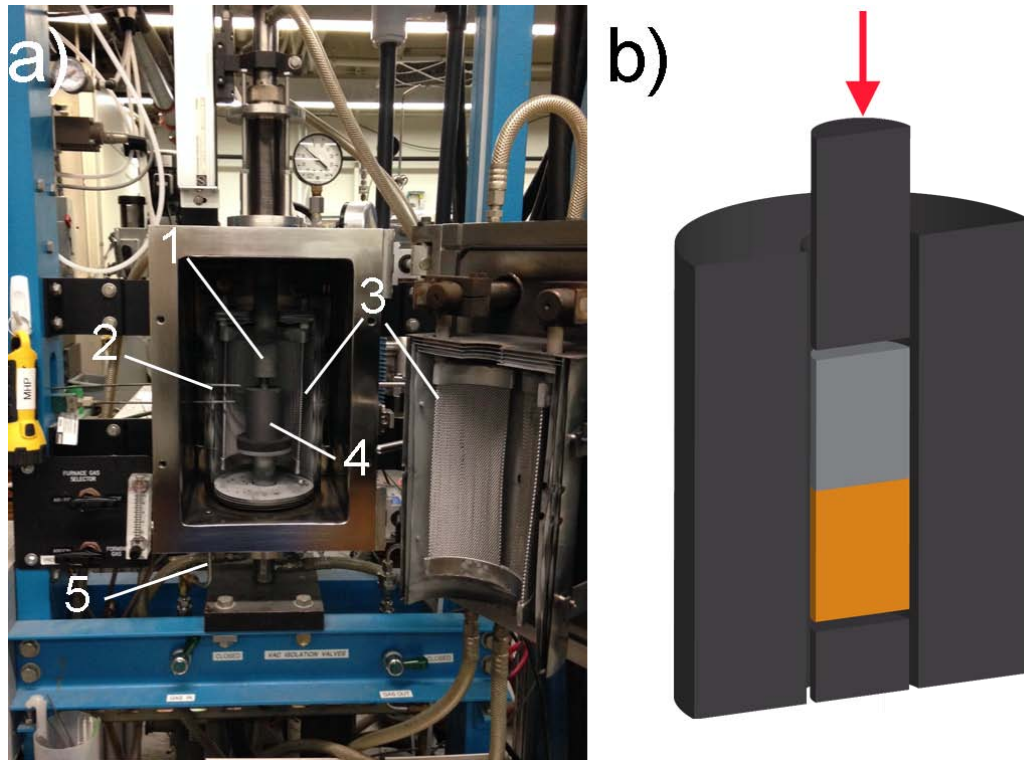


Figure 4.1: Mini hot press for diffusion bonding of Al-Cu couples: a) Hot press furnace with (1) load ram, (2) thermocouples, (3) heating elements, (4) constraining device (see b) , (5) valve for reducing atmosphere Ar_{95}H_5 . b) Schematic representation of constraining device preventing the diffusion couple from “mushrooming” (creeping) during the diffusion bonding process.

due to an external cooling circuit once the heating zone is switched off. Back at room temperature, the processed diffusion couples can be removed safely from the furnace.

Effect of temperature on diffusion bonding

The effect of temperature on the quality of the diffusion bond has not been systematically studied in this work. However, it was found that at temperatures below 450 °C the diffusion couples were weakly bonded, whereas bonding temperatures of 530 °C resulted in strongly bonded Al-Cu couples. If not otherwise mentioned, a set temperature of 530 °C was kept throughout the diffusion bonding experiments and the influence of other parameters such as surface condition, applied load, and dwelling time were investigated and are discussed hereafter.

Effect of surface condition on diffusion bonding

Optimum surface condition is crucial to ensure a high bonding quality. As previously mentioned, contaminations during the process are prevented by purging the furnace chamber with reducing atmosphere during the entire process. However the surface condition of both faying surfaces is even more delicate. After machining, the prospectively bonded surfaces were ground with SiC sandpapers to remove the casting zone resulting from electric discharge machining (EDM), followed by a cleaning procedure in an ultrasonic bath of isopropanol. It is claimed that ideal diffusion bonding condition is ensured if the faying surfaces can be brought together at atomic distance i.e. perfectly parallel and smooth surfaces enhancing atomic motion of both materials into each other. Since this scenario is impossible to achieve at a bulk length scale, another theory claims that diffusion bonding involves plastic deformation of the rough surfaces [Cline, 1966]. Especially since aluminum has a tenacious oxide layer (Alumina) [Wu and Lo, 2002], which only melts at temperatures exceeding the melting point of copper and aluminum, respectively [Celik et al., 1997]. Thus, it is assumed that plastic deformation of the tips on the rough surface leads to breakage of the oxides, which inhibit bond formation and in this case a higher surface roughness favors the formation of the diffusion bond. The effect of surface roughness on the bond quality is shown on two samples 23 and 25, where all the other process parameters were kept identical (see table 4.1). In sample 23 the surfaces were ground up to 600 grit size, whereas in sample 25 the surfaces were ground up to 1200 grit size, leading to a smoother

Table 4.1: Overview of selected preliminary diffusion bond samples

sample	r_1 °C/min	T_1 °C	d_1 min	f_1 N	r_2 °C/min	T_2 °C	d_2 min	f_2 N	r_3 °C/min	T_3 °C	d_3 min	f_3 N	surface roughness	investigated parameter
pipsl	5	50	5	2000	10	530	180	2000	5	200	0	0	600 SiC	
11	5	50	5	500	10	530	180	500	-	-	-	-	600 SiC	dwelling time
13	5	50	5	500	10	530	120	500	-	-	-	-	600 SiC	dwelling time
14	5	50	5	1000	10	530	60	1000	-	-	-	-	600 SiC	force
15	5	50	5	1000	10	530	120	1000	-	-	-	-	600 SiC	dwelling time
16	5	50	5	1000	10	530	180	1000	-	-	-	-	600 SiC	dwelling time
17	5	50	5	1000	10	530	30	1000	-	-	-	-	600 SiC	dwelling time
20	5	50	5	2000	10	530	60	2000	-	-	-	-	600 SiC	force
21	5	50	5	3000	10	530	60	3000	-	-	-	-	600 SiC	force
22	5	50	5	4000	10	530	60	4000	-	-	-	-	600 SiC	force
23	5	50	5	1000	10	530	180	1000	-	-	-	-	600 SiC	force
24	5	50	5	2000	10	530	180	2000	-	-	-	-	600 SiC	force
25	5	50	5	2000	10	530	180	2000	-	-	-	-	1200 SiC	surface roughness

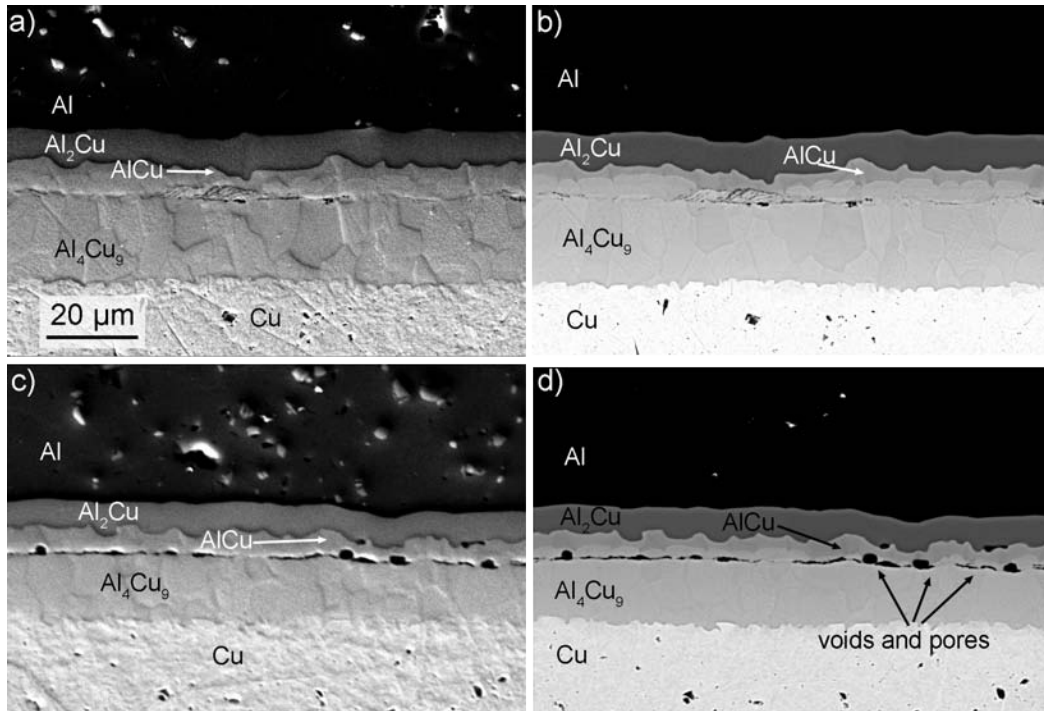


Figure 4.2: Effect of surface roughness on diffusion bonded interface: (a & b): SE and BSE image of sample ground with 600 SiC; (c & d): SE and BSE image of sample ground with 1200 SiC.

surface. Metallographic cross sections were inspected by means of scanning electron microscopy (SEM), where a secondary electron (SE) and back scatter electron (BSE) detector were employed. The cross sections are shown in Fig. 4.2. Fig. 4.2a and b show the cross section of the sample with rough bonding surface (sample 23) compared to the bond with smooth bonding surface (sample 25) in Fig. 4.2c and d. It can be concluded that in the case of bulk diffusion bond formation the best success for diffusion bonding is achieved by creating an intermediately rough surface with defined surface roughness as opposed to using a perfectly smooth surface. A measurement of the entire diffusion zone featuring three intermetallic compounds was carried out in both cases showing that the diffusion zone is 30 μm thick in the case of the rough surface whereas in the case of sample 25 the diffusion zone is only 26 μm thick, which also indicates that a smooth surface leads to retardation of the diffusion process. In the second case bigger voids are visible which may be attributed to the reduced plastic deformation at the bond interface, as proposed by [Zuruzi et al., 1999].

Effect of applied pressure on diffusion bonding

The effect of the applied force (pressure) perpendicular to the the diffusion bond was investigated in two steps. First, low force at 500 N was applied on two samples – 11 and 13 – to primarily investigate the dwelling time from 120 min to 180 min at a peak temperature of 530 °C. In Fig. 4.3 metallographic cross sections are shown. For the specimen 11 bonded during 2 h at 530 °C in Fig.4.3a the bond interface is poorly developed featuring several voids. The diffusion zone thickness is inhomogeneous ranging from 26 μm to only 15 μm , where the third intermetallic, AlCu, has yet not been evolved. In Fig.4.3b a slight improvement of the bond is visible featuring a continuous interface but it can be seen that the bonds are weak featuring unbonded regions. No improvements were found with a higher dwelling time. It can be concluded that an applied force of 500 N resulting in a bonding pressure of 3.9 MPa is insufficient.

Finally, a second measurement series to investigate the effect of applied force (bonding pressure), where all the other bonding parameters were kept identical, was conducted at elevated ram loads starting at 1000 N (7.8 MPa) up to 4000 N (31.6 MPa) – see samples 14, and 20 – 22 in table 4.1. Metallographic cross sections of the resulting bond interfaces are shown in Fig. 4.4. Some inhomogeneities in the bond formation as a function of bonding force were found: The bond formed with a force of 1000 N (7.8 MPa) revealed an inhomogeneously formed bonding interface with a diffusion zone thickness varying between 6 and 12 μm accompanied with abundant presence of pores and gaps (see Fig. 4.4a). In contrast specimen 20 – bonded at 2000 N (15.78 MPa) (see Fig. 4.4b) – features a plane interface of a bond thickness of approximately 11 μm . The samples created at 3000 N (23.4 MPa) and 4000 N (31.6 MPa) (see Fig. 4.4c and Fig. 4.4d respectively) resulted in similarly sound bonding interfaces, where no voids could be detected. The interface thickness was 19 μm and 18 μm , respectively. Accordingly, it can be concluded that an increase of the bonding force favors plane and homogeneous interfacial formation and thus accelerates the bonding process. To reduce the formation of inherent stresses the usage of very high bonding forces was renounced. It was found to be a good compromise to increase the bonding duration to 180 min but to decrease the applied load to 2000 N (approximately 16 MPa).

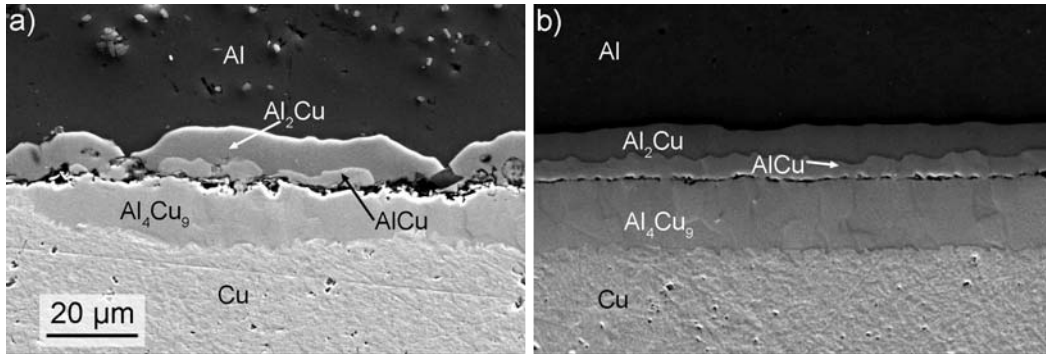


Figure 4.3: Effect of diffusion bonding time at 500 N force (a) 120 min at 530 °C and (b) 180 min at 530 °C. The latter reveals a throughout interface with parallel intermetallic compounds, however voids are still present between Al_4Cu_9 and AlCu .

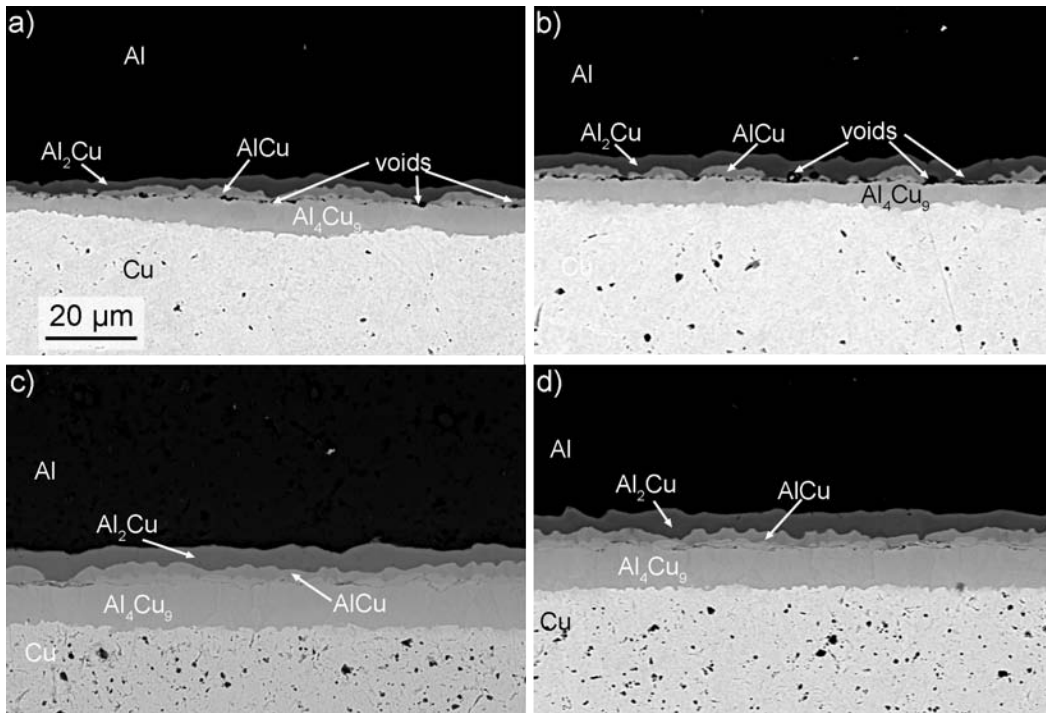


Figure 4.4: Effect of variation of force during bonding for 60 min at 530 °C.

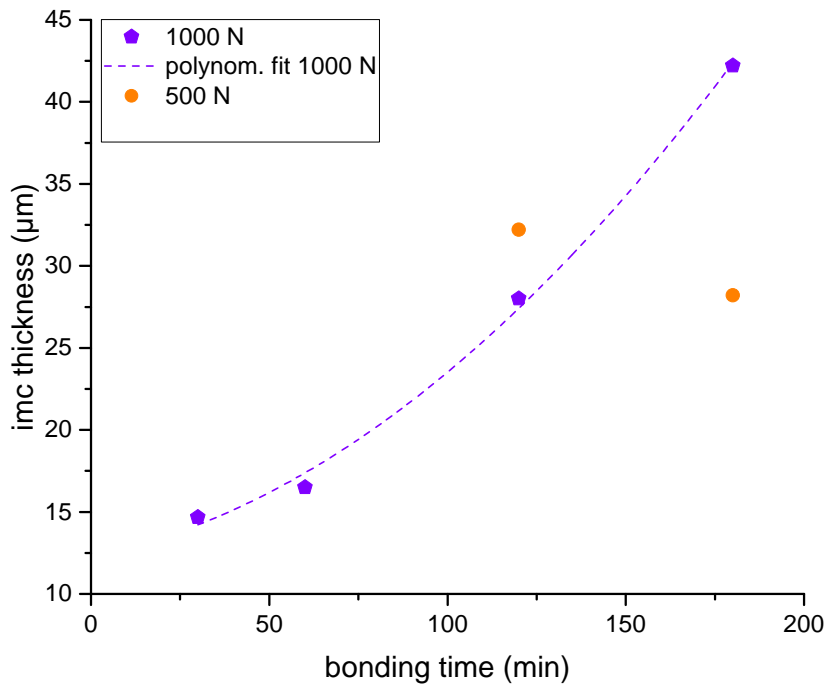


Figure 4.5: Dependence of interfacial thickness on bond time achieved at 530 °C at pressures of 3.9 MPa (500N) and 7.8 MPa (1000N).

Effect of process duration (dwelling time) on resulting bond interface

The diffusion bonding kinetics were studied by measuring the entire intermetallic stack thickness as a function of bonding duration on samples 14 – 17 (see table 4.1) and 11 and 13. In both series the process temperature was set at 530 °C and thus they only differ in the applied load: Samples 14 – 17 were held at 7.8 MPa, whereas in the case of 11 and 13 a load of 3.9 MPa was used. In Fig. 4.5 the stack thickness as a function of bond duration is plotted for both series. It can be seen that at a holding pressure of 3.9 MPa no significant changes in the intermetallic thickness was observed, whereas in the case of an applied load of 7.8 MPa a parabolic relationship between intermetallic thickness and dwelling duration is confirmed. This again concludes that at loads below 7 MPa the load ram is not stable and thus no reproducible processes can be performed.

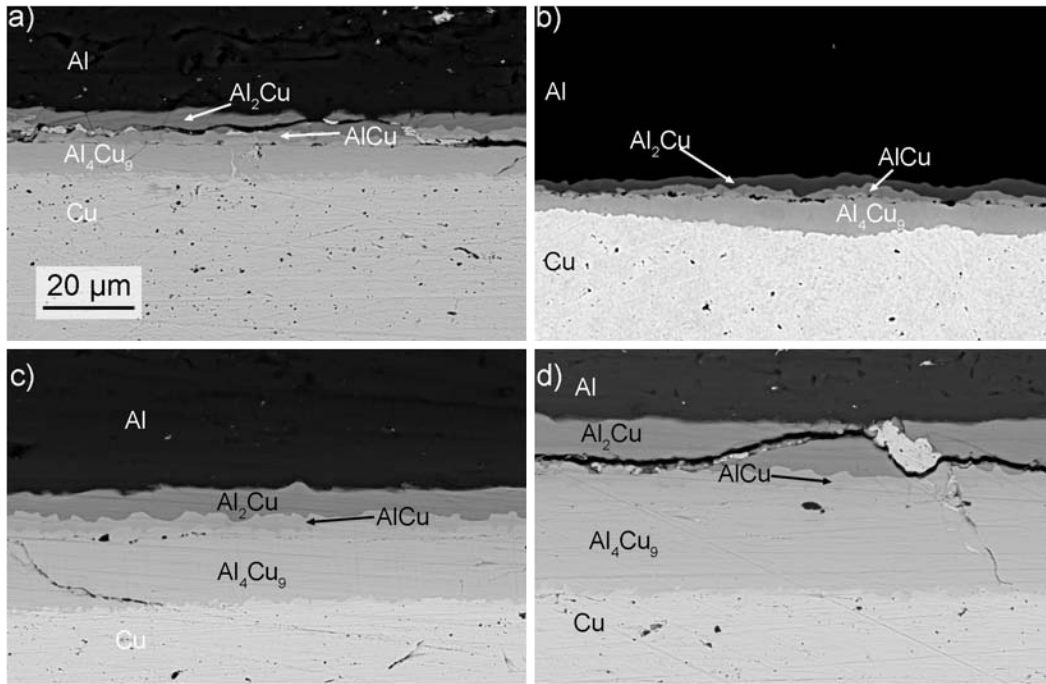


Figure 4.6: Interfacial evolution during diffusion bonding process with applied load 1000 N (7.8 MPa) (a) after 30 min (sample 17), (b) after 60 min (sample 14), (c) after 120 min (sample 15), and (d) after 180 min (sample 16).

4.1.2 Summary of preliminary diffusion bond experiments

Summarizing the described diffusion bond experiments above in 4.1.1, the following conclusions can be drawn on the choice of the optimum processing parameters for the prospective fatigue specimen preparation:

- Increased surface roughness of the bonding surface favors diffusion bond formation due to plastic deformation at the surface tips when pressure is applied.
 1. The plastic deformation of the rough tips allows a close contact of the bonding elements.
 2. The tenacious aluminum oxide layer, inherent to the aluminum surface, inhibits chemical reactions. The rough surface tips can break this layer and thus interdiffusion of aluminum into copper and vice versa is enhanced.
- Increase of normal pressure reduces void formation and leads to plastic deformation of the bonding surface. On the other hand bonding pressures exceeding 15 MPa increase stresses in the bond causing cracking of the brittle intermetallics, which is not desired for the bonding process. Thus bonding pressures around 15 MPa were found to be optimal for this purpose.
- Interfacial evolution (i.e. the thickness of the diffusion zone) follows a parabolic dependence from interfacial thickness with increasing bonding duration.
- The energy release rate is decreased by orders of magnitude if a symmetrical material sequence is chosen. A specimen setup is chosen, where a high purity 50 μm thin aluminum foil is sandwiched between two bulk high purity copper rods.

4.1.3 Characterization of diffusion bonded fatigue specimen

For the following experiments fatigue samples containing bulk intermetallic compound layers are desired. Hence, a total bonding duration of 180 min was chosen at which the peak temperature is held. The bonding pressure was set to 15 MPa during the process and was released for the cooling period, which is separated into two stages: From a set temperature of 530 $^{\circ}\text{C}$ to 200 $^{\circ}\text{C}$ a controlled slow cooling rate of 5 $^{\circ}\text{C}/\text{min}$ was chosen to achieve equilibrium conditions and to avoid internal stresses. In the second stage, the furnace chamber is rapidly cooled down to room

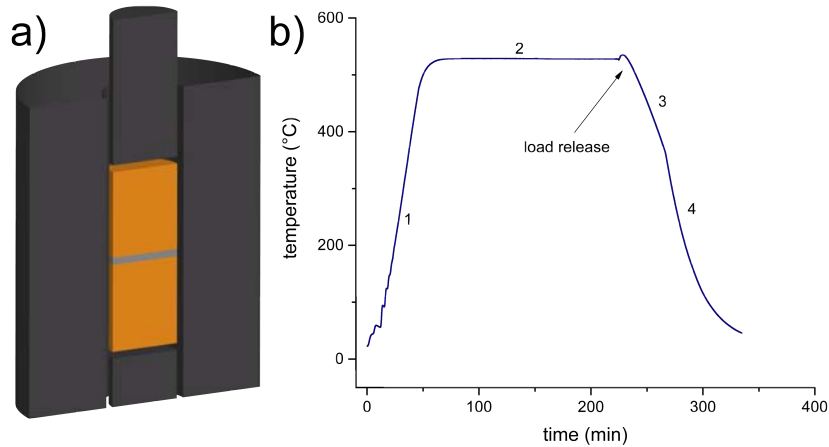


Figure 4.7: (a) Specimen setup for bonding process: thin Al foil sandwiched between two bulk copper rods. (b) Final temperature profile monitored with thermocouple. It can be subdivided into four process steps: (1) heating to desired peak temperature with a heating rate of 10 °C/min, (2) dwelling at 530 °C, 3: slow cooling down 5 °C/min, 4: rapid cooling to room temperature. During 1 and 2 a bonding pressure of 15 MPa was applied to the parts to be bonded, in the cooling phase the load was released.

temperature by means of an external water cooling circuit. The actual temperature was monitored during the entire run with a K-type thermocouple, which was inserted into the chamber and brought close to the specimen surface. The specimen setup consisting of a thin Al foil sandwiched between two bulk Cu rods and the final temperature profile are depicted in Fig. 4.7.

A detailed characterization of the resulting diffusion bond interface is given in the following section. First, in 4.1.3 the microstructure of the interface is discussed followed by nanoindentation measurements to determine the mechanical properties of the formed intermetallic compounds in 4.1.3.

Interfacial microstructure

Metallographic cross sections were created out of the resulting diffusion bond, made by hot pressing of a thin Al foil sandwiched between two Cu rods using the process parameters described in 4.1.3.

The resulting bond interface was metallographically sectioned followed by mechanical grinding and polishing procedures up to final polishing with a 0.1 µm diamond suspension. Residual mechanical stresses and scratches at the surface were removed by ion milling with a precision ion polishing system (PIPS) from GATAN,

which is typically used for TEM specimen preparation. Here, low current argon beams smoothly ablate the surface of the specimen, where flat incident angles of 5° between the surface and the beams are chosen. During the milling process the specimen rotates to allow even material removal. For the analyses a high resolution field emission gun (FEG) FEI XL 30 SEM equipped with an EDAX camera to record electron backscatter diffraction (EBSD) patterns was used.

Fig. 4.8 shows a high resolution back scattered electron image giving a phase sensitive contrast and thus clearly showing the symmetrically evolved intermetallic phases across the bond, where the brightest region is the copper richest and in the darkest region aluminum is the predominant element. Additional EDX scans confirmed the intermetallic phases, which could be identified as Al_2Cu (located next to the thin remaining aluminum layer), followed by AlCu and Al_4Cu_9 (located next to the bulk copper). Additionally, electron backscatter diffraction scans (EBSD) were recorded from selected areas, as shown in Fig.4.9. Therefore, the specimen was inclined at a tilt angle of 70° and the diffraction patterns were observed with an EDAX camera. Fig.4.9b shows an EBSD scan of $158\text{ }\mu\text{m} \times 273\text{ }\mu\text{m}$ that was chosen along the diffusion bond, where a scanning step size of $0.2\text{ }\mu\text{m}$ was chosen, resulting in a total of approximately 10^6 scan points. The resulting EBSD data was optimized with the data analysis software TSL analysis OIM, where grain dilatation algorithms were employed. In all material layers no preferential crystallographic orientation can be seen in the resulting inverse pole figure maps. However, a considerable inhomogeneity of grain sizes occurs across the material layers. Whereas copper and aluminum feature an average grain size of $60\text{ }\mu\text{m}$ and $40\text{ }\mu\text{m}$, respectively the intermetallics have a significantly lower average grain size. Al_2Cu has an average grain size of $30\text{ }\mu\text{m}$ and is the coarsest grained material. Its counter part Al_4Cu_9 and AlCu have average grain sizes of $15\text{ }\mu\text{m}$ and $3\text{ }\mu\text{m}$, respectively. The residual aluminum layer solely consists of a one grain size thick layer. To obtain more statistics on the grain size distribution in the bulk copper, a second scan at lower magnification was conducted afar from the bond interface (see Fig.4.9b).

Mechanical properties of Al-Cu intermetallic compound

Nanoindentation tests were conducted to assess the mechanical properties of the evolved intermetallic compounds in the resulting diffusion bond with above described microstructure (see section 4.1.3). Therefore, an unmounted plane-parallel sample was machined from the diffusion bond and metallographically sectioned in-

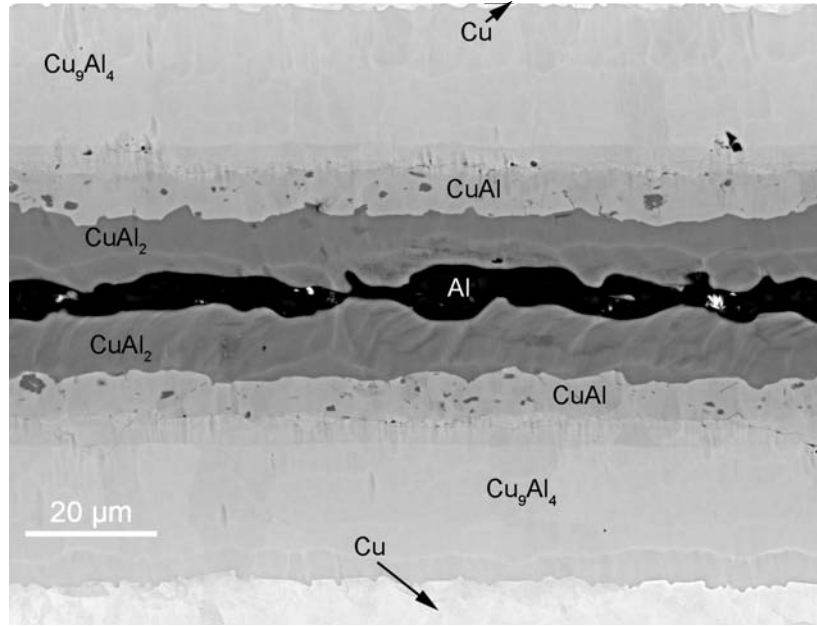


Figure 4.8: Cross section of diffusion zone featuring the present intermetallic compounds formed between copper and aluminum. The present intermetallic compounds are symmetrically distributed ranging from Al richest up to Cu richest.

cluding fine polishing with a 0.1 μm diamond suspension followed by a precision ion polishing procedure of the investigated cross-section. The small specimen with mirror like finishing was directly glued to the sample holder of the nanoindenter. The measurements were conducted with an ASMEC Unat device in combination with a Vickers indentation tip. More than 10 indents per intermetallic compound layer were sampled. In Al_4Cu_9 and AlCu a total of 13 measurement points were chosen respectively. For the Al_2Cu layer 17 points were necessary due to its slightly uneven surface. The indentation process was controlled by an implemented ISO standard program, which determines the indentation velocity, holding time, pre-set maximum indentation load and load relieve rate. The maximum indentation load was chosen as a function of the corresponding phase layer thickness and its hardness known from literature [Kouters et al., 2013]: To avoid plastic interactions with adjacent interfaces a rule of thumb dictates that the resulting indent should not exceed one third of the relevant feature. Here, special regard was set to the resulting indent is smaller than one third of the layer thickness to inhibit interactions between the plastic zone emanating from the indent and the adjacent interfaces. The obtained results are summarized in table 4.2 including the number of measurement

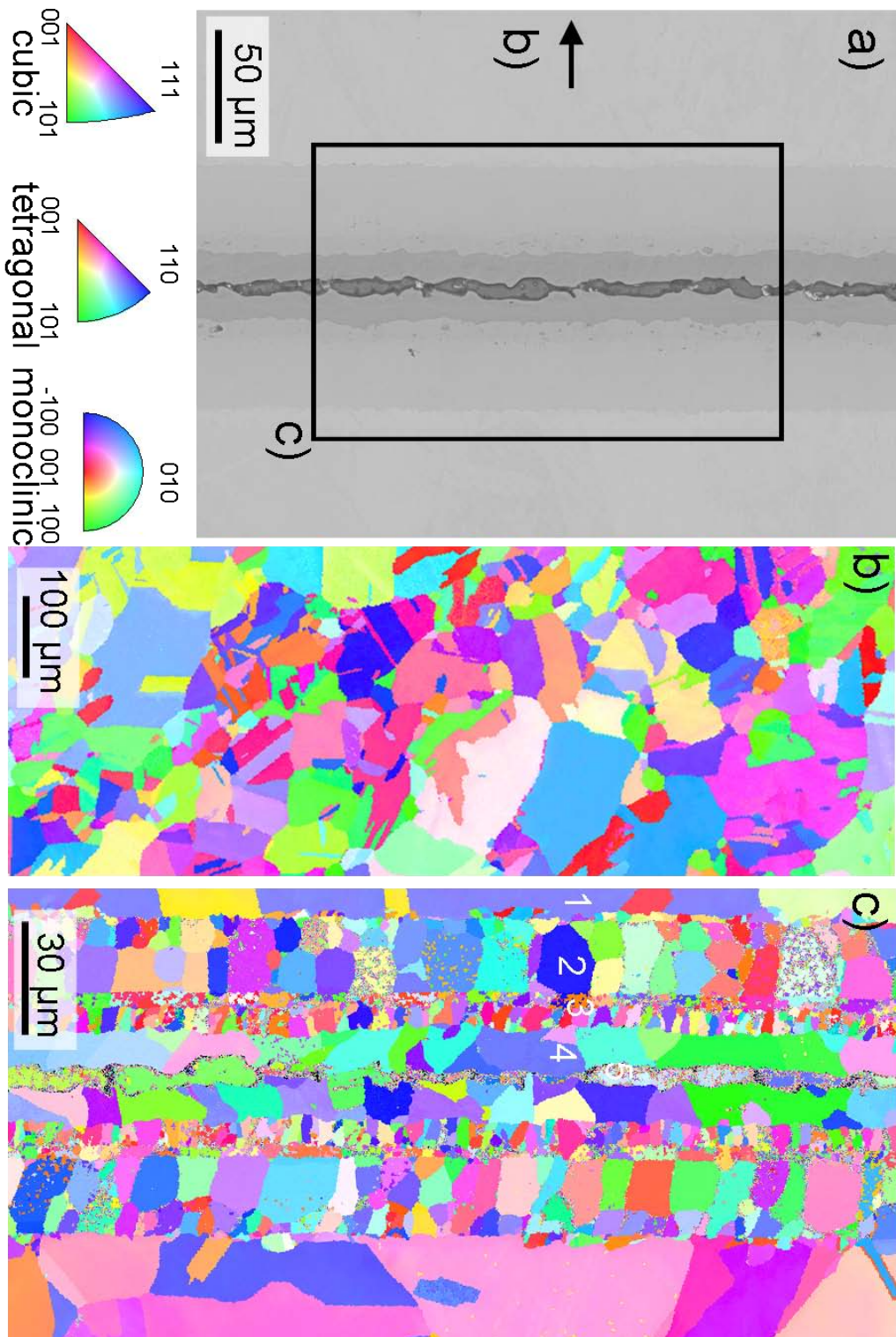


Figure 4.9: Microstructure of bulk Cu-Al-Cu diffusion bonded interface (a) SEM overview of bond interface, (b) low magnification inverse pole figure (IPF) map of copper afar from bond interface and (c) close-up and IPF map of the present materials 1: copper, 2: Al_4Cu_9 , 3: AlCu , 4: Al_2Cu , and 5: thin aluminum layer in the center of the bond. The IPF pole legend for cubic (copper, aluminum, Al_4Cu_9), tetragonal (Al_2Cu) and monoclinic (CuAl) lattice are given.

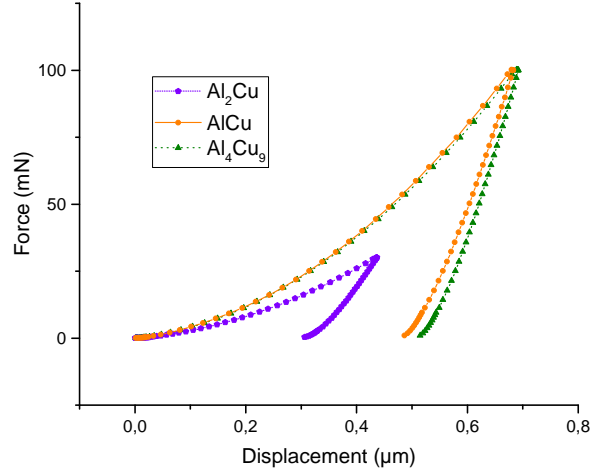


Figure 4.10: Nanoindentation results comparing the different intermetallic layers: Average force–displacement curves for Al_2Cu , AlCu and Al_4Cu_9 .

Table 4.2: Nanoindentation results of Al-Cu intermetallic compounds. With F denoting the maximum load, E the Young’s modulus and H_V the Vickers hardness. All values are presented with their statistical uncertainties (standard deviation).

Material	# data points	F (mN)	E (GPa)	H_V (MPa)
Al_2Cu	16	30.068 ± 0.002	111.1 ± 6.8	442 ± 25
AlCu	12	100.182 ± 0.001	168.0 ± 5.5	651 ± 19
Al_4Cu_9	12	100.188 ± 0.004	183.8 ± 10.8	606 ± 31

points (i.e. indents) per layer, maximum indentation load and hardness values, elastic moduli, and Vickers hardness including the corresponding uncertainties (i.e. standard deviation); representative load-displacement curves averaging the single measurement points for each tested intermetallic phase are depicted in Fig. 4.10. After excluding the outliers, these curves were directly obtained from the software. The zero point calibration occurred by optimizing a Hertzian fit in the first section of the load-displacement curve. Due to the increased hardness of AlCu and Al_4Cu_9 , respectively, a maximum load of 100 mN was set, whereas for Al_2Cu a maximum load of 30 mN was chosen.

4.1.4 Heat treatments of diffusion bond interface

Isothermal heat treatments were conducted to study interfacial reactions among the present materials in the as-bonded state when subjected to further heat treatments. In the following fatigue experiments another question will be to understand the role of the soft aluminum sandwiched between the hard intermetallic compound layers. Additionally, it was the aim to obtain a microstructure similar to the as-bonded state, but with entirely consumed aluminum in order to investigate the role of the presence or absence of aluminum layer on the high cycle fatigue properties of the diffusion bond. The heat treatments were conducted at 500 °C from 1 h up to 4 h under inert atmosphere (N_2).

Four as-bonded diffusion bonds were subjected to the heat treatments and subsequently metallographically sectioned to study their morphology, interfacial thickness and microstructure. In Fig. 4.11 SEM-micrographs of the aged diffusion bonds are juxtaposed in combination with transverse EDX line-scans revealing the atomic distribution across the bonds to identify the layers. As can be seen, in all four cases the intermetallics are the same as in the as-bonded state again Al_2Cu , $AlCu$ and Al_4Cu_9 . For each heat treatment secondary electron images highlighting different layers the microstructural morphology in combination with back scattered electron images and EDX linescans revealing the different layers were conducted. The resulting intermetallic compound layer thicknesses and the total diffusion bond thickness (i.e. the thickness of the entire stack of intermetallic layers including the aluminum layer-if still present) is shown in table 4.3. After 2 hours of annealing the aluminum layer is still partly present (due to inhomogeneities of the initial thickness of the aluminum) and is only entirely consumed after 3 hours. When comparing the individual layer thicknesses of the evolved intermetallic compounds it can be concluded that the intermetallic reactions occur as follows: While the overall diffusion bond thickness remains approximately constant regardless of the annealing time the following interfacial reactions occur: Firstly, the aluminum layer is entirely consumed, and further transformed into $CuAl_2$. Finally, the $AlCu$ layer grows. In Fig. 4.12c+d the microstructure of the annealed specimen (3 h/500 °C) is compared to the microstructure obtained after 4 h annealing at 500 °C revealing a pronounced grain coarsening in the present intermetallic compound layers.

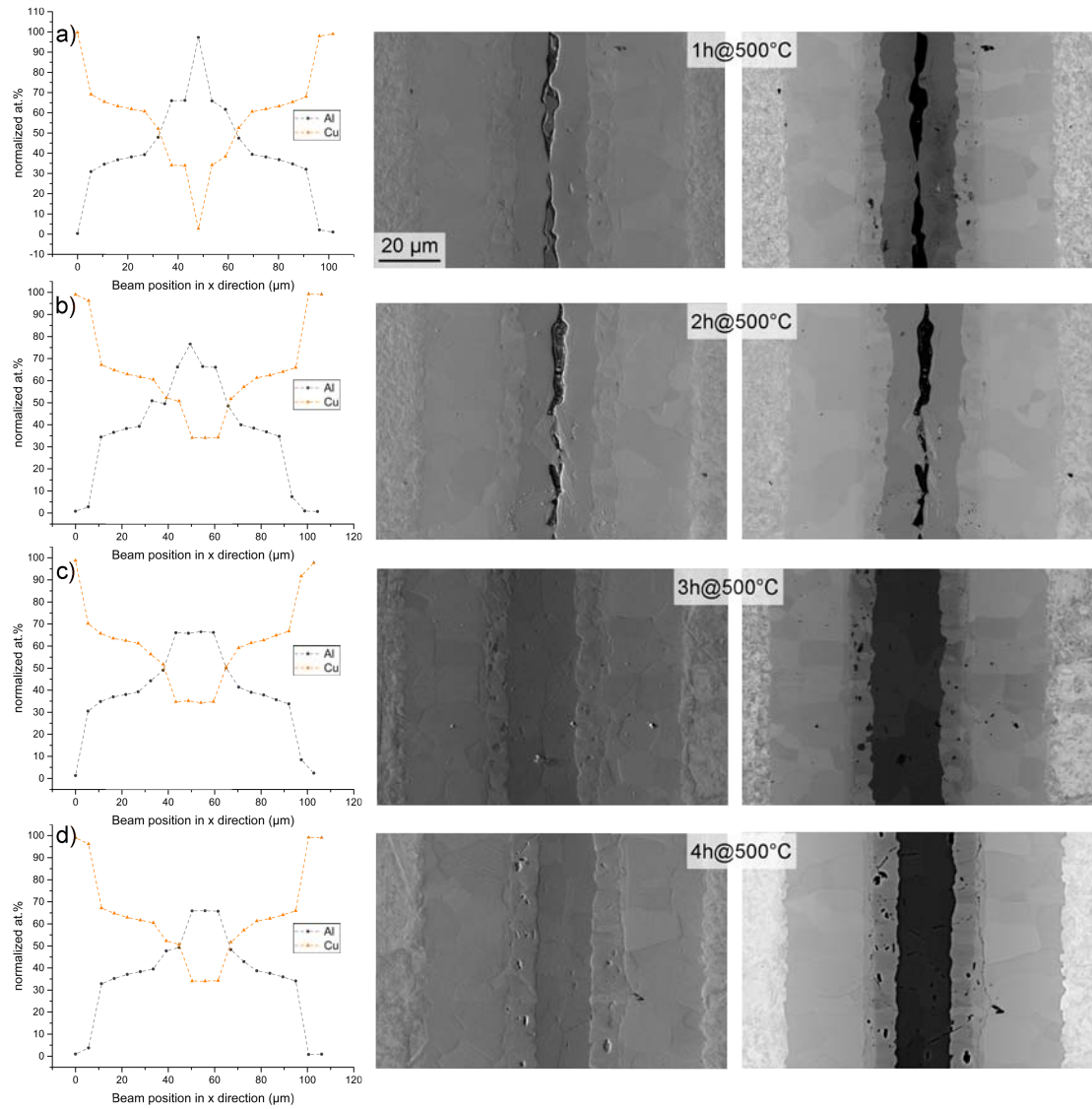


Figure 4.11: Microstructures after heat treatment for (a) 1 h at 500 °C (b) 2 h at 500 °C (c) 3 h at 500 °C (d) 4 h at 500 °C. Left: SEM-EDX profiles showing the distribution of Al and Cu across the bond, middle: secondary electron microscope, right: back scatter electron image. The scale is identical for all micrographs.

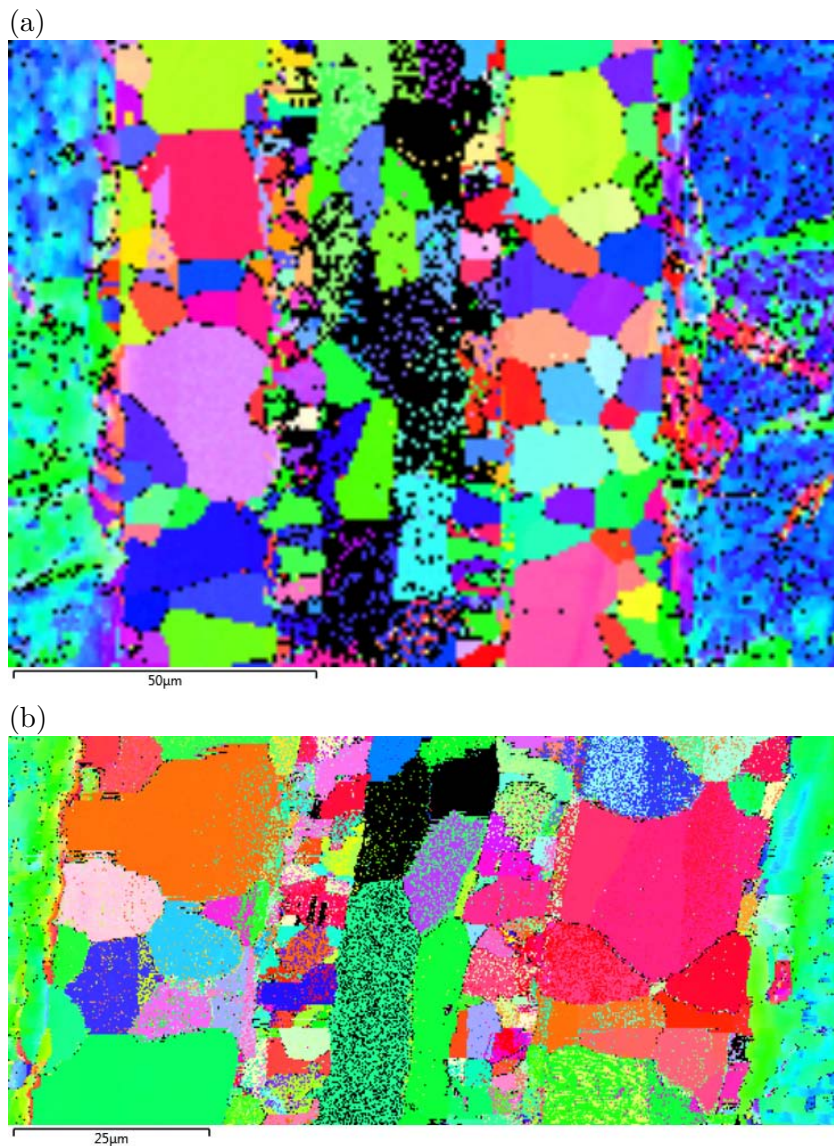


Figure 4.12: Inverse pole figure maps of specimens annealed for (a) 3 h at 500 °C and (b) 4 h at 500 °C.

Table 4.3: Material layer thickness as a function of annealing time

Material heat treatment	aluminum thickness (μm)	Al_2Cu thickness (μm)	AlCu thickness (μm)	Al_4Cu_9 thickness (μm)	total diffusion zone thickness (μm)
as-bonded	1.8-7.1	10.8	6.1	23.9	88.0
1h at 500°C	1.2 – 4.8	10.7	5.8	25.1	87.4
2h at 500°C	1.6 – 4.1	9.2 – 11.6	5.1	26.3	86.4
3h at 500°C	—	23.1	6.9	26.0	90.4
4h at 500°C	—	16.5	8.1	26.5	91.5

4.2 Ultrasonic fatigue testing of bulk Al-Cu interfaces

High cycle fatigue tests were conducted on bulk Al-Cu diffusion bonds featuring the microstructure and intermetallic compounds described in section 4.1.3. It was the aim to understand the influence of brittle intermetallic compounds on crack initiation, propagation, deflection processes and final fracture behavior of the entire Al-Cu bond and thus to reveal the lifetime limiting, weakest link when subjected to cyclic mechanical loads. Emphasis is set on the effect of load mixity on the fatigue behavior of the bond and to vary the amounts of shear and tensile stress acting on the investigated Al-Cu bond. Three lifetime curves were measured, where the diffusion bond interface was subjected to three different load conditions to reveal which stress contribution is most harmful to the bond.

The diffusion bonds, processed as previously described in 4.1.3, were tested by means of an ultrasonic fatigue testing setup operating at 20 kHz. Dog-bone shaped fatigue specimens fulfilling the longitudinal resonance condition at the operation frequency were machined from a bulk diffusion bonded Cu rod-Al foil-Cu rod-sandwich such that the investigated bond is located at the center of the gauge section, where maximum strain occurs. Attached to the ultrasonic resonance fatigue setup the specimen is stimulated to resonance vibration causing cyclic stresses at the center of the sample resulting in subsequent fatigue failure. The setup and specimen design are shown in Fig. 4.13. The stress amplitude acting cyclically at the bond interface is measured by a strain gauge, which is glued to the specimen in a way that the bond is located at the center of the 3 mm long strain gauge section. Thus, the strain ϵ_y acting parallel to the loading direction on the bulk copper and on the diffusion zone respectively is integrally sampled. The resulting stress amplitude σ_y is obtained by applying the one dimensional Hooke's law since in the high cycle fatigue regime the induced stresses are mainly elastic. Thus it

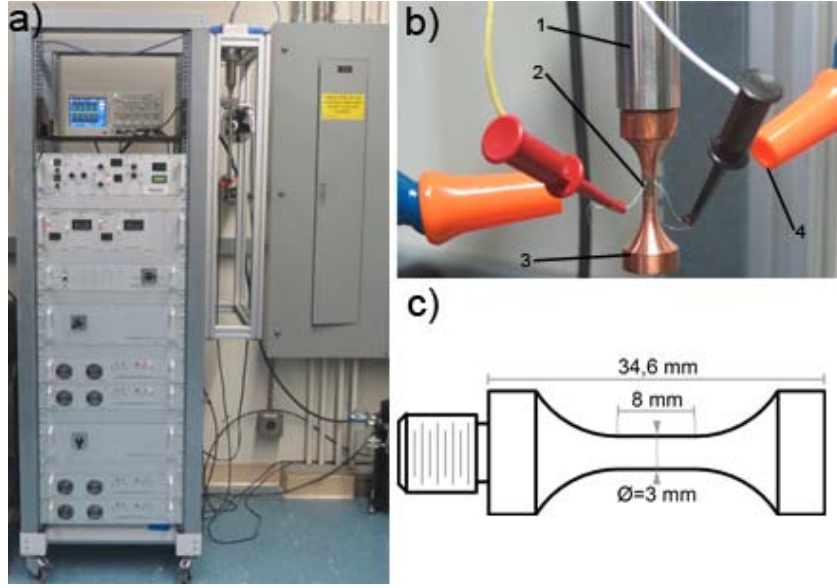


Figure 4.13: Setup for ultrasonic fatigue testing of bulk specimen: (a) Ultrasonic resonance fatigue system with attached specimen to horn (b). Technical drawing of fatigue specimen with bond interface located at the strain node, resonating at approximately 20 kHz (c).

follows for the measured and adjusted stress amplitude:

$$\sigma_y = E \cdot \epsilon_y \quad (4.1)$$

where ϵ_y is the measured strain parallel to the loading direction. Since the strain gauge section is 3 mm long and the diffusion bond thickness is only approximately 100 μm thick, copper accounts for the main strain contribution and thus its Young's modulus E of 120 GPa is employed. Pure tensile stress loading condition, i.e mode I, acting at the bond interface is achieved, when the bond is oriented perpendicular to the loading direction. A combined loading condition, resulting in a mixed mode of mode I (tensile) and mode II (shear) loading, is obtained by inclination of the bond at a certain angle θ , which is schematically illustrated in Fig. 4.14. The stress state at the interface can be described as plane stress condition and the problem can be described by a two dimensional cartesian coordinate system. The coordinate system x-y describes the external loading condition, where the y-axis is parallel to the load train of the setup. To quantify the contributions of tensile stress σ and shear stress τ acting on the inclined bond the coordinate system x'-y' is introduced, which is rotated at an angle θ with respect to x-y such that the x'-axis coincides

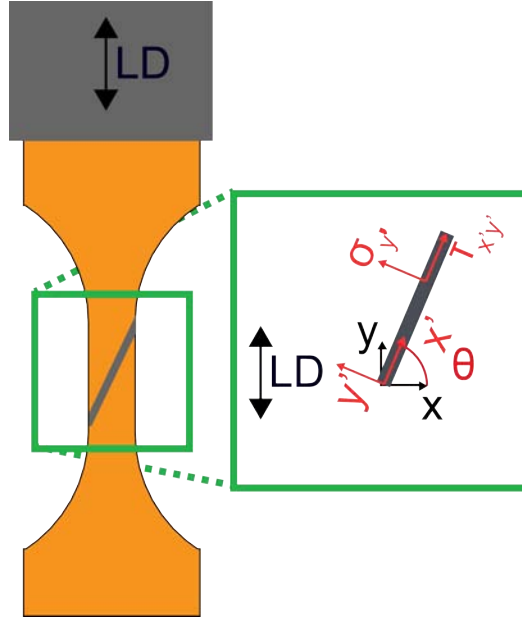


Figure 4.14: Orientation of the bond interface with respect to the loading direction (LD). The coordinate system x-y describes the externally applied loading condition. The coordinate system x'-y' rotated at an angle θ from x-y describes the stress conditions occurring at the bond interface.

with the inclined interface.

The correlation between tensile $\sigma_{y'}$ and shear stress $\tau_{y'x'}$ acting at the bond interface due to the longitudinal excitation parallel to the loading direction σ_y are obtained by the following relations:

$$\sigma_{y'} = \frac{F_{y'}}{A_{y'}} = \frac{F_y \cdot \cos \theta}{A_y / \cos \theta} = \sigma_y \cdot \cos^2 \theta \quad (4.2a)$$

$$\tau_{y'x'} = \frac{F_{x'}}{A_{y'}} = \frac{F_y \cdot \sin \theta}{A_y / \cos \theta} = \sigma_y \cdot \sin \theta \cdot \cos \theta \quad (4.2b)$$

where the nomenclatures are explained in Fig. 4.14.

For the following fatigue experiments three interfacial orientations were chosen and are described hereafter:

1. 0° (interface perpendicular to LD, 100% tensile stress acting at the bond)
2. 45° (50% tensile stress, 50% shear stress)

3. 67°(30% tensile stress, 70% shear stress)

Prior to each measurement the resonance frequency of the load train is manually adjusted, where the incoming and reflected signals are monitored with an oscilloscope. The resonance frequency of the setup corresponds to the adjustment, where maximum amplitude of the feedback signal is observed. Once the resonance frequency is found, a frequency controlled mode is set. Finally, a calibration procedure is conducted, that operates the setup such that a desired stress amplitude is reached, where the strain is linearly related to the power amplitude of the setup. To prevent the specimen from excessive heating, the experiments are conducted under discontinuous pulse/pause-mode, where the pulse duration lasts 200 ms followed by a pause mode of 250 ms. Compressed air cooling is additionally used at the gauge section during the entire fatigue test. The used ultrasonic fatigue setup and the chosen specimen constellation including a technical drawing of the specimen are shown in Fig. 4.13. The end of the fatigue test is determined, when the pre-set amplitude can only be achieved by a significant drop of the frequency indicating that increased fatigue damage has evolved, which disturbs the resonance condition due to decreased coupling of the specimen.

4.3 Influence of loading mode on the fatigue behavior of bulk Al-Cu bonds

The high cycle fatigue behavior of the bulk Al-Cu diffusion bond with above described microstructure and intermetallic compounds (see section 4.1.3) was studied under three different, well-defined load conditions with variable amounts of mode I (tensile loading) and mode II (shear loading). The desired loading condition could be obtained by inclining the interface at a certain angle as illustrated in Fig. 4.14. In all three cases, the center of the interface coincides with the strain node of the setup (i.e. the center of the gauge section of the fatigue specimen).

The chosen orientations for this study are 0°, 45° and 67° leading to 100%/0%, 50%/50% and 30%/70% normal stress/shear stress contributions, respectively.

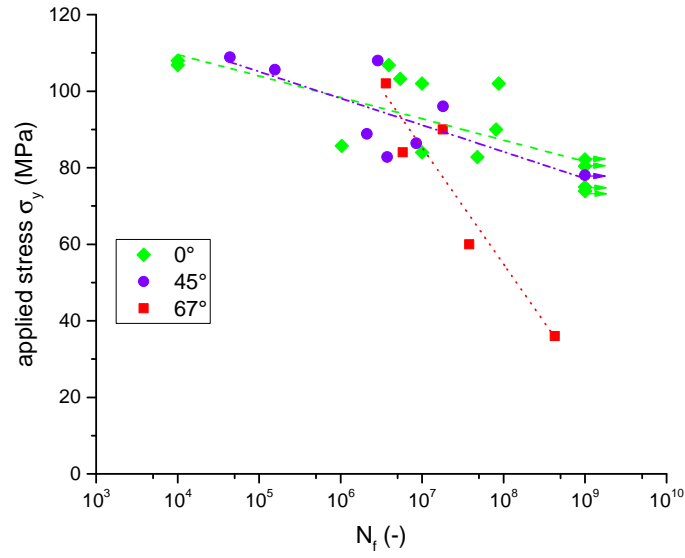
Three fatigue data plots depending on the interface orientation relative to the loading direction are summarized in Fig.4.15. Two representations of the data are chosen: In Fig.4.15a the applied stress σ_y parallel to the loading direction is plotted against the number of loading cycles to failure N_f . N_f is easily determined as

a significant loss of the resonant frequency automatically stops the experiment. A drastic decrease of the resonant frequency is typically due to a loss of coupling caused by a significantly evolved fatigue crack within the sample. This representation, however, does not give any information on the stresses occurring at the interface but only on the applied stress amount necessary to rupture the bond after a defined number of loading cycles.

When comparing the fatigue behavior of a material undergoing complex stress states, suitable yield criteria need to be introduced, as previously discussed in section 2.1.2. While the representation of equivalent stresses according to the von Mises yield criterion is widely applied to ductile, engineering materials, the investigated material combination is composed of brittle intermetallics, which are involved in the crack propagation and fatigue failure process. Therefore, the Rankine yield criterion is used in the present study to compare the equivalent stresses depending on the loading modes and the fatigue data expressed in equivalent stress $\sigma_{eqRankine}$ vs. N_f in Fig.4.15b.

From this representation of the fatigue data it can be concluded that the bulk Al-Cu bond is less sensitive to loading in tension-compression than to an increased amount of shear loading contribution. The obtained results are different to previous investigations, where the high cycle fatigue behavior of ductile materials is compared under pure tension-compression loading vs. pure torsional loading (i.e. pure shear loading) (e.g. [Mayer, 2006] and [Akiniwa et al., 2008]). In both studies the investigated materials (aluminum and high strength steel, respectively) show a higher fatigue performance under pure shear than under pure tensile loading. In contrast, in a previous study (Ref. [Tanaka et al., 1984]) it was reported that Otsuka et al. (see Ref. [Otsuka et al., 1980]) compared the crack propagation modes of A7076-T6 aluminum under mode I and mode II and proved that the fatigue crack propagates faster in mode II. Zimmermann and co-authors compared the fatigue behavior of laser welded steel-steel and iron-steel joints under pure torsional and a combination of axial and torsional loading (see Ref. [Zimmermann et al., 2014]). Again, it was shown that the joints subjected to pure torsional loads have a higher fatigue performance than in the specimens subjected to a load combination between torsional and axial mode. According to Ref. [Li et al., 2009], which reviews the multiaxial fatigue models for ductile, semi-ductile and brittle materials, the controlling parameter of brittle materials is the amplitude of maximum normal stress/strain. When comparing the fatigue data of the specimens with an interface

(a)



(b)

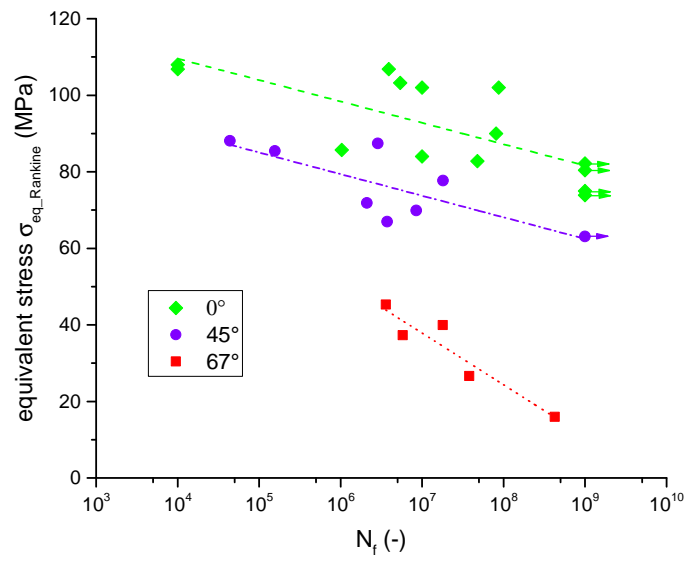


Figure 4.15: Fatigue data of bulk Al-Cu diffusion bond interface: (a) plot of applied stress σ_y (b) plot of equivalent stress using the Rankine criterion $\sigma_{eq,Rankine}$. Arrows indicate run-outs.

orientation perpendicular to the loading direction (see Fig. 4.15) with literature, the data is comparable to the data of obtained for high cycle fatigue investigations of polycrystalline bulk pure copper which ranges at loading cycles to failure between 115 MPa to approximately 95 MPa, respectively. A fatigue limit was set around 92 MPa for cycles up to 10^{10} see e.g. Ref. [Phung et al., 2013] or [Stanzl-Tschegg and Schönbauer, 2010]. In the case of coarse-grained, pure aluminum the high cycle fatigue values are around 35 MPa for loading cycles of 10^6 . A so-called “fatigue limit” of this material was set around 30 MPa, see e.g. Ref. [Höppel et al., 2010].

Furthermore, a study was conducted on how the different stress amounts vary in relation to the applied stress σ_y as a function of inclination angle θ , which was previously described in Fig.4.14. The results are summarized in Fig. 4.16, where the stress ratio of the corresponding stress over σ_y as a function of inclination angle ranging from 0° (corresponding to 100% tension-compression, which is when the interface is perpendicular to the loading direction) up to 90° (here, the interface would be parallel to the loading direction). In this plot a comparison of the pure tensile stress $\sigma_{y'}$ and pure shear stresses $\tau_{x'y'}$ acting at the interface and the resulting equivalent stress distributions applying the Tresca, von Mises and Rankine criteria. From this analysis it can be deduced that both, the von Mises and Tresca criterion, overestimate the stresses occurring at the bond, which was a further confirmation to apply the Rankine criterion in this fatigue study since brittle materials are involved.

4.3.1 Fractographic observations

Fractographic investigations were conducted on the obtained fracture areas to further understand the failure mechanisms involved in this material combination.

In the case of the specimens subjected to 100% tension-compression loads (pure mode I) a very clear fracture morphology could be identified. The specimens subjected to this loading mode all ruptured entirely at the end of the fatigue experiment. Representative fracture areas are shown in Fig.4.17. In Fig.4.17a and Fig.4.17b an overview of two corresponding fractured bonds are shown. The crack initiated in the aluminum layer in the center of the bond followed by a deflection into the neighboring layer, Al_2Cu , where a radially outwards crack propagation is observed. In the last step final fracture occurred in the most brittle layer AlCu . At higher magnification images in Fig.4.17c-d show the crack path from the initiation

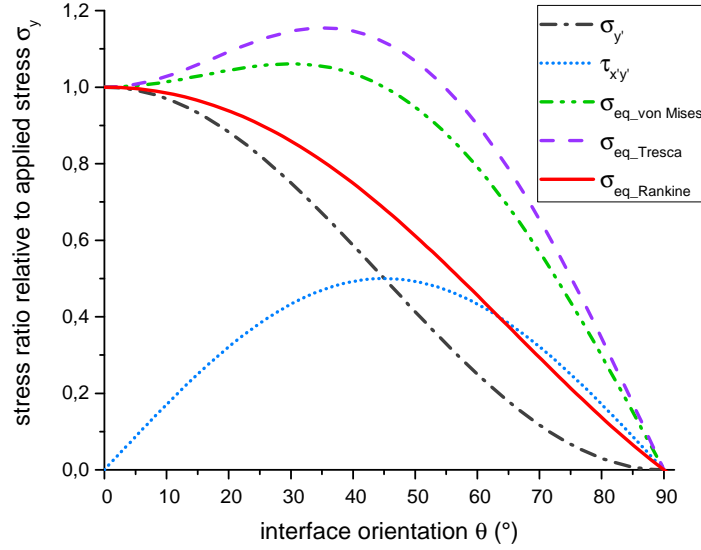


Figure 4.16: Stress measures as a function of inclination angle of the interface: pure shear stress $\tau_{x'y'}$, pure tensile stress $\sigma_{y'}$, and comparison of equivalent stresses obtained by: Rankine $\sigma_{eq_Rankine}$, von Mises $\sigma_{eq_vonMises}$ and Tresca σ_{eq_Tresca} .

site, denoted by ductile dimples parallel to the loading direction and the surrounding crack propagation morphology, which evolves radially in Al_2Cu . In Fig.4.17e-f the ductile dimples in the aluminum are highlighted. In further specimens the same fracture pattern was observed, where each process is denoted by a characteristic morphology, as shown in the SEM micrographs in Fig.4.18. Fig.4.18a highlights the transition from the crack initiation site (aluminum) to the crack propagation, which occurs in the neighboring layer. It can be seen, that in the propagation zone the grains are deformed and that transgranular fracture occurred. Partially some highly deformed grains could be identified, as highlighted in Fig.4.18b. The final fracture regime is characterized by a purely brittle intergranular fracture, which occurred in the small-grained Al-Cu area.

The interfaces inclined at 45° to the loading direction showed a very complex fracture morphology, as shown in Fig. 4.19. Here, crack initiation was found to occur close to the sample surface, located at the position of the strain node. From fracture mechanistic approaches where the crack propagation of a notch oriented 45° to remote tensile loads (see e.g. [Broek, 1986], [Anderson, 2005] or [Gross, 1996]) it is expected that finally the crack propagates perpendicular to the remote tensile

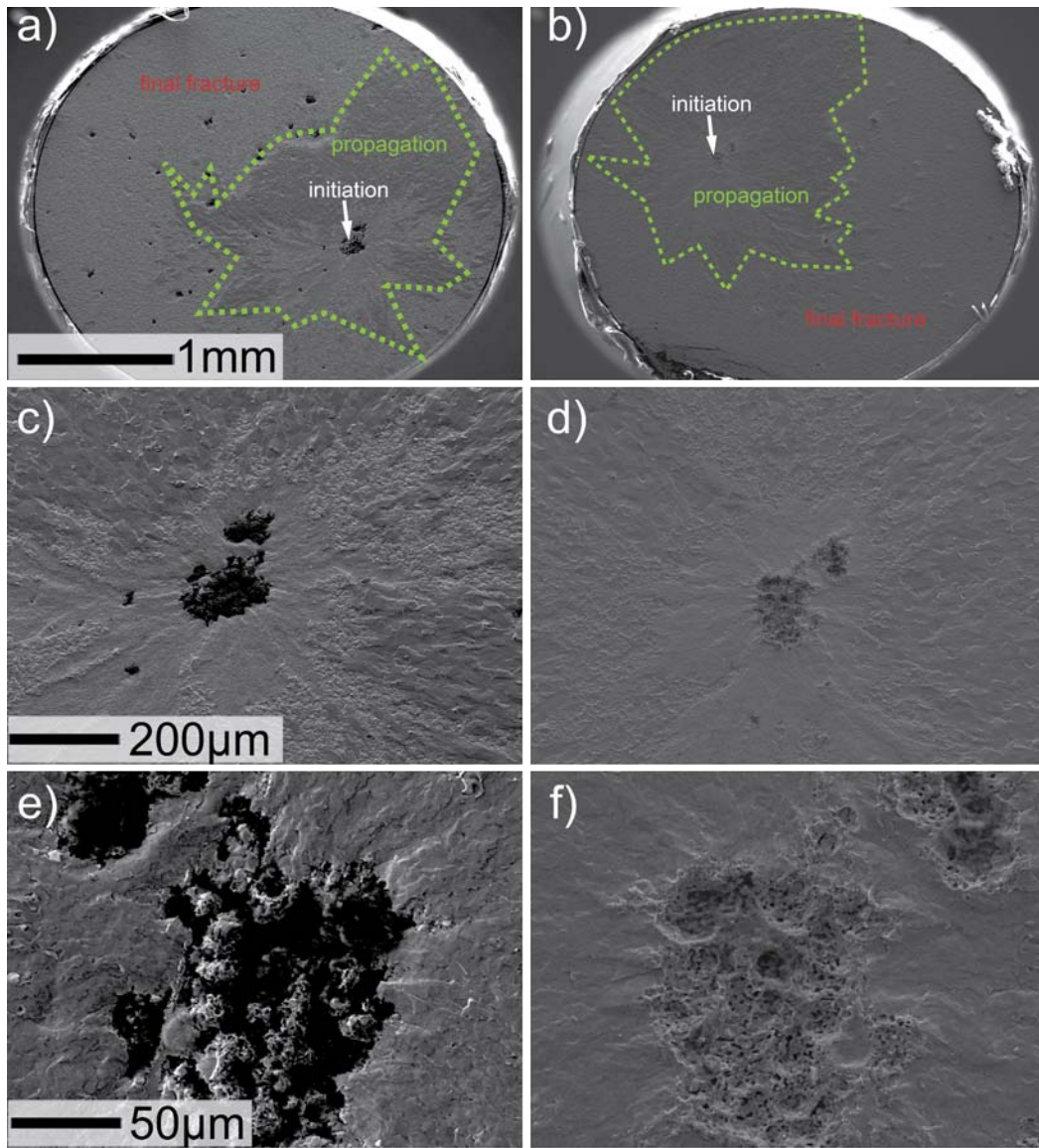


Figure 4.17: Typical fatigue fractographs of mode I fatigue specimen (0°): (a & b) give an overview indicating the fatigue initiation in the center of the bond in aluminum, followed by a radially outwards crack propagation in Al_2Cu . Final fracture occurred in the bond periphery in the most brittle intermetallic, AlCu , denoted by an intergranular fracture type. (c & d): close-up of crack deflection. (e & f): high-light of dimples in Al.

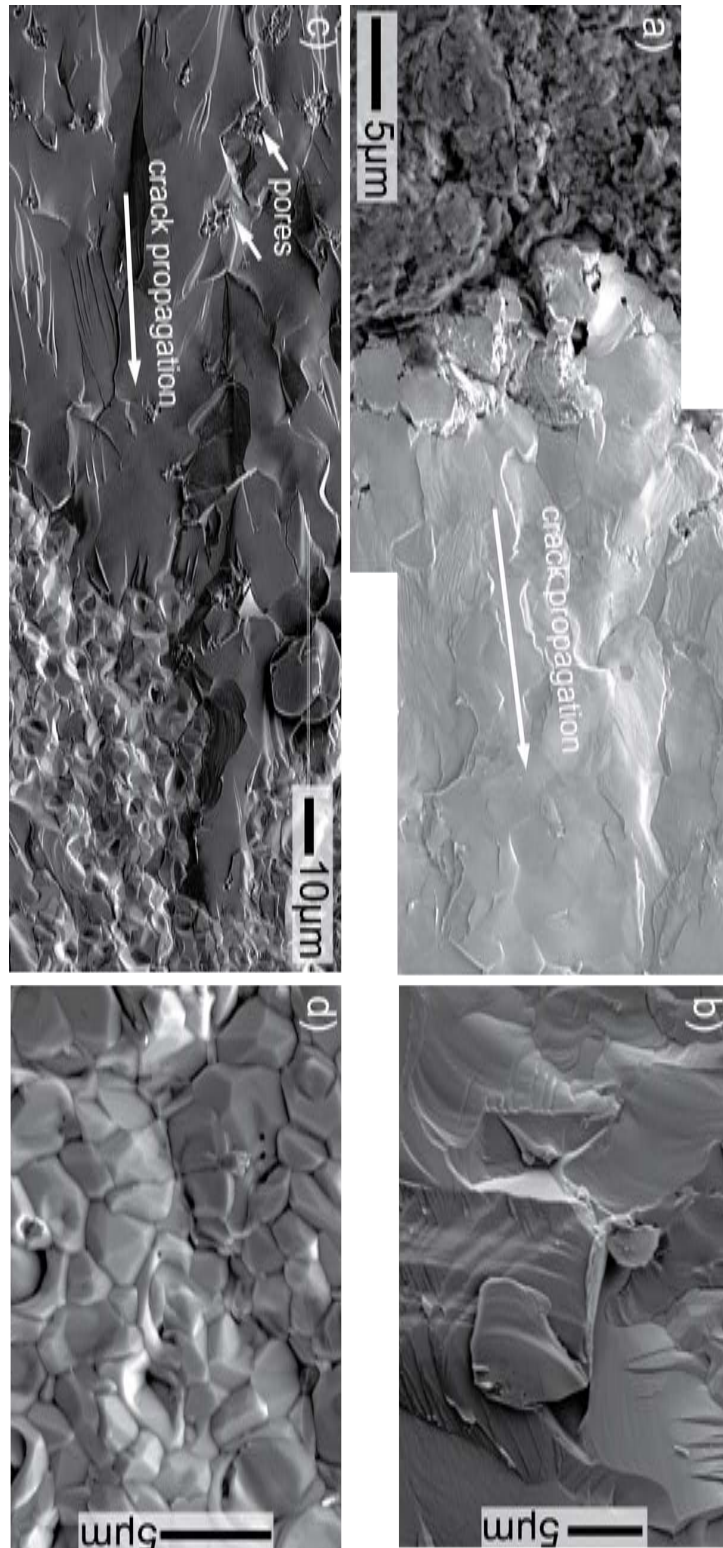


Figure 4.18: Close up of crack path morphologies of fatigued Al-Cu bonds (pure mode I): (a) Crack deflection from initiation site (Al) to crack propagation regime (Al_2Cu), (b) high magnification of fatigued Al_2Cu highlighting highly deformed grain, (c) crack deflection from Al_2Cu into AlCu (d) brittle, final fracture in AlCu (intergranular fracture).

load. In this case, however, the crack remained in the bond interface, which is oriented 45° to the load direction. The crack meandered between the intermetallic compounds until throughout the diffusion bond. This fracture behavior is indicative for a fracture type of brittle nature. Additionally, cracks perpendicular to the fracture surface could be identified, which may have occurred during final fracture due to stress release. In Fig. 4.19c & d a close-up of the selected region is shown to highlight the intermetallic phases (c) by a BSE image and the shear morphology (d) by a SE image. In (d) a clear delamination of the involved layers are shown. The specimens inclined at 67° did not rupture, when the experiment stopped. The resonance condition was disrupted due to a remarkable decrease of the eigenfrequency, which is typically considered as evidence for a significant crack evolution. However, in the highly inclined samples it is assumed that due to the high area of the bond interface crack deflection into the soft and ductile copper, which does not result in a separation of the fatigue specimen. Further investigations are necessary to confirm this assumption.

While there exists no studies on the fatigue behavior of the investigated material combination, few publications on the static fracture behavior of bulk Al-Cu diffusion couples exist (see Ref. [Kouters et al., 2011], [Kouters et al., 2013], [Koberna and Fiala, 1993]). While in the studies conducted by Kouters and coauthors it was shown that an overall degradation of the bond occurred, Koberna et al. identified Al_2Cu as the most fracture sensitive material and correlated the induced stresses due to the formation of intermetallics with their change in density compared to the density of its two neighboring material layers (see Ref. [Koberna and Fiala, 1993]). In another study conducted by Chen and co-authors (see Ref. [Chen et al., 2006]) static fracture tests on Al-Cu bonds created by roll bonding followed by a subsequent sinter treatment to grow the intermetallic compounds again confirmed that fracture occurred in the same IMC layer, Al_2Cu . These studies however are static studies and the fatigue behavior of such bonds is still unknown.

In a previous study [Cremer et al., 2013], where the fatigue behavior of a welded seam was ultrasonically tested the crack initiation was mainly attributed to incomplete fusion sites, which act as stress concentrators according to the $\sqrt{\text{area}}$ -law suggested by [Fatigue and Murakami, 2002]. In the present study, however, such

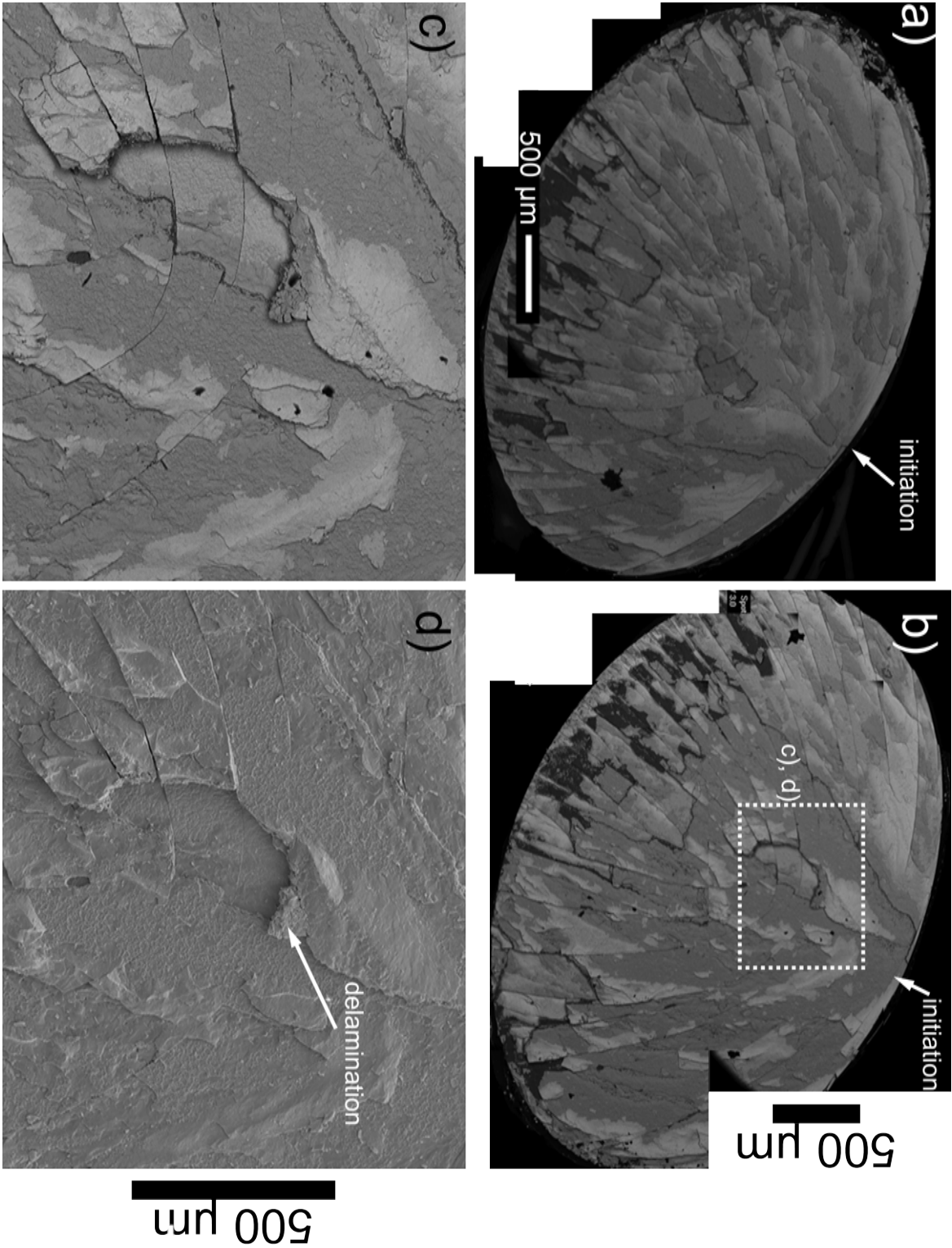


Figure 4.19: Fatigue fracture morphologies of specimens inclined at 45°.

unbonded regions could not be found.

4.4 Role of aluminum on the fatigue behavior of bulk Al-Cu bonds

The fatigue fractographs of the as-bonded diffusion bond interfaces oriented perpendicular to the loading direction the crack initiation site could be identified as aluminum. To understand the role of the thin aluminum layer and to compare with the case of its absence in the Al-Cu diffusion bond interface with several brittle intermetallic compounds a comparative study, where the fatigue behavior of bulk Al-Cu diffusion bond interfaces with entirely consumed aluminum was conducted. The diffusion bonded fatigue specimens were subjected to additional isothermal heat treatments (at 500 °C for 3 h under inert atmosphere), as described in 4.1.4. The aim was to achieve a comparable microstructure of the prevailing materials, where especially excessive grain coarsening was avoided. Fig.4.20 compares the fatigue life data of the previously investigated as-bonded specimens with the specimens with the aged specimens, where the aluminum was entirely consumed. It could be shown that, even though aluminum is the site of crack initiation, it acts as buffer. The fractographs of the aged specimens shown in Fig. 4.21 again revealed a crack propagation and a final fracture regime being in agreement with previous observations in the previous section in 4.3.1. However the crack initiation regime was difficult to identify and still need further systematic investigations. Highly magnified of the crack propagation, which again occurred in Al_2Cu and final fracture in AlCu of the aged fatigue specimens are shown in Fig.4.22.

The experiments are in agreement with the comparison of the high cycle fatigue behavior of the miniaturized ball bond specimens presented in section 3.4.2: Even though aluminum could always be identified as the responsible crack initiation site, highly annealed specimens where the aluminum has been entirely consumed fail catastrophically at lower stress amplitudes when subjected to cyclic loads.

4.5 Summary

In this chapter the aim was to study the fatigue behavior of bulk Al-Cu pairs with a geometry that allows a predefined loading setup in contrast to the inevitable, “complicated” loading condition during the fatigue test of the miniaturized speci-

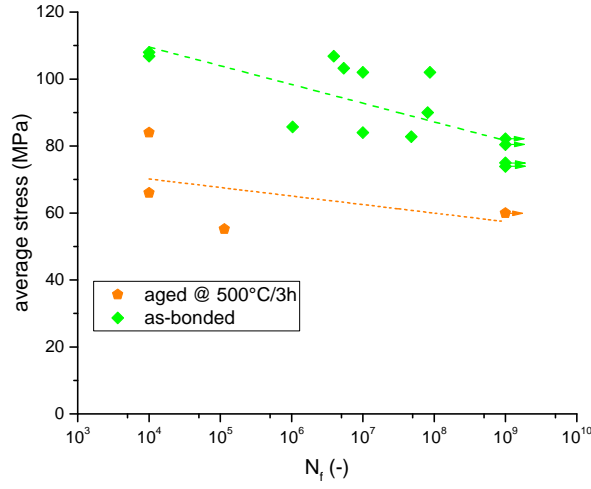


Figure 4.20: Fatigue data of bond interface oriented perpendicular to loading direction: as-bonded (with aluminum) aged for 3 hours at 500 °C, where the aluminum is entirely consumed. Arrows indicate run-outs.

mens as presented in chapter 3. The bulk fatigue experiments were conducted on bulk Al-Cu pairs, which were created by diffusion bonding. Therefore the first part of this project was dedicated to optimize the diffusion bond parameters such that bulk intermetallic layer evolve at the interface and to reduce process induced flaws such as unbonded regions or cracks. Furthermore, the aim was to obtain the same three intermetallic compounds Al_2Cu , AlCu and Al_4Cu_9 to mimic the highly aged state of the miniaturized Al-Cu ball bonds.

It was found that optimum conditions for this purpose were to sandwich a thin aluminum foil between two bulk copper rods. To aid the diffusion process and to maintain the original rod shape of the components a constraining die was machined. The bonding process was conducted at 530 °C for 180 minutes under inert atmosphere to minimize contaminations of the faying surfaces during the process. The resulting diffusion bond was composed of the same intermetallics as the highly aged ball bond specimens, which were confirmed by EDX and EBSD scans: Al_2Cu , AlCu and Al_4Cu_9 . This solid-solid joining method was chosen over other techniques as it ensures a flat bond interface with parallel intermetallic compounds at a macroscopic length scale.



Figure 4.21: Overview of fatigue fracture surface of bond interface oriented perpendicular to loading direction aged for 3 hours at 500 °C(aluminum is entirely consumed): Crack initiation is difficult to determine, crack propagation occurred again in Al_2Cu followed by final fracture in AlCu .

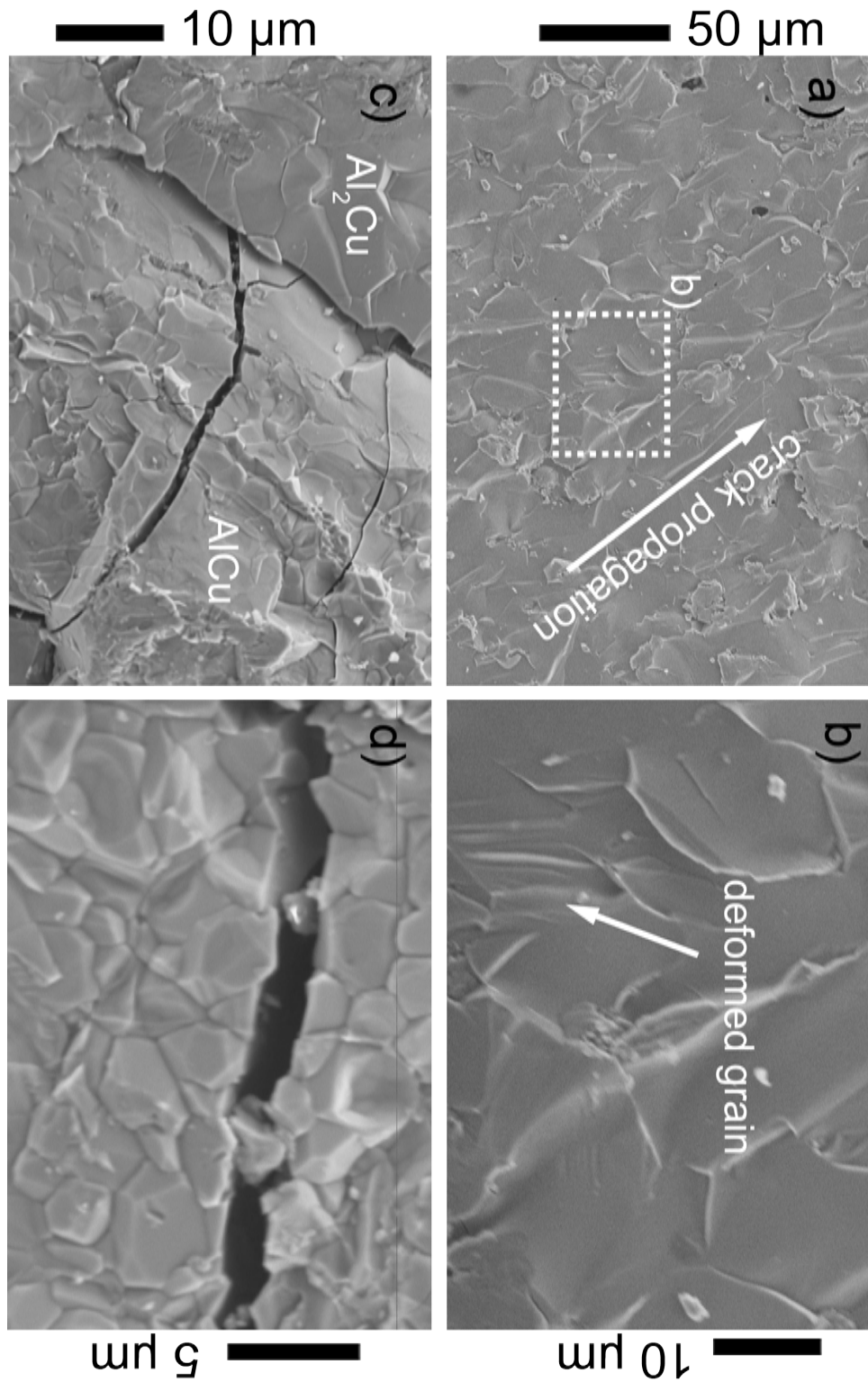


Figure 4.22: Close-up of the typical crack propagation and final fracture morphologies: (a) Crack propagation in Al_2Cu showing the crack propagation direction along the deformed grains (b) highly magnified deformed grain in crack propagation regime (c) transition between propagation and final fracture (d) final fracture in AlCu denoted by brittle, inter granular fracture.

Dogbone-shaped, high cycle fatigue specimens were created and tested with an ultrasonic resonance fatigue setup operating at 20 kHz. The resonating samples were created such that the diffusion zone is located at the strain node of the load train of the setup.

To achieve mixtures of mode I and mode II loading, specimens were created where the diffusion bonded interface is inclined at a certain angle relative to the loading direction. It could be shown, by usage of the Rankine equivalent stress criterion, that the specimens with a higher shear loading mode (mode II) feature a lower high cycle fatigue performance compared to the specimens loaded at pure tension-compression (mode I) loads.

In the case of the specimens loaded at mode I, fractographic investigations revealed that the crack initiation site was aluminum followed by crack propagation through Al_2Cu and final fracture in AlCu . The crack propagation regime was denoted by highly deformed grains, which gave a hint of plasticity involved in the fracture process.

Additionally, the high cycle fatigue behavior of aged diffusion bond samples, where aluminum has been entirely consumed, was compared to the as-bonded samples under pure mode I loading. In agreement to previous investigations on miniaturized ball bond specimens it could be demonstrated that the presence of aluminum is crucial for the high cycle fatigue behavior and thus, the samples with aluminum have a higher fatigue performance than the samples, where aluminum has been entirely consumed.

It can be concluded from these high cycle fatigue experiments that the lower the ductility of the investigated material, the more it will fail in a catastrophic way.

5 In-situ TEM fatigue test of Al-Al₂Cu interface

In the following chapter the aim is to observe crack initiation, propagation and crack deflection processes, which are involved during cyclic loading of the highly aged Al-Cu system, in-situ.

In chapter 3, the fatigue behavior of miniaturized Al-Cu interfaces was investigated. It was found that due to the inherent bond geometry, where the transition between the bonded and unbonded regime in the bond periphery acts as natural notch and crack initiation is forced in the aluminum. In the highly aged state as described in 3.4.1, where the three intermetallics Al₂Cu, AlCu and Al₄Cu₉ are developed, crack initiation and propagation were again observed in aluminum at the bond periphery. However, at locations where the aluminum was entirely consumed, crack deflection was observed into the copper rich intermetallic compound, followed by a final fracture in the intermetallic AlCu.

To exclude the above mentioned geometry effects and to thoroughly understand how this material combination performs under well-defined cyclic loading conditions, a bulk “handable” and well-defined geometry with a bond interface featuring the same intermetallic compounds, as previously described, was chosen and studied in chapter 4. Analogous to the miniaturized Al-Cu interface aluminum was responsible for the crack initiation process. However, crack propagation was observed in Al₂Cu followed by final fracture in the brittle AlCu intermetallic compound.

While in the previous chapters integral fatigue lives were studied, where the total lifetime under a pre-set load condition is measured, it is aimed at observing and comprehending the involved mechanisms behind fatigue failure in this material system. Therefore, a micron scale fatigue test in a TEM is designed and conducted on the Al-Al₂Cu system to study crack initiation, propagation – and possible crack deflection – up to final fracture. In situ nanomechanical testing in the TEM has provided great insight into fundamental deformation mechanisms

by imaging defect interactions during the experiment with nanoscale resolution and correlating them with the resulting load-displacement curve. First advances in the field of in-situ testing and nanomechanical testing under TEM have been reported in e.g. Ref. [Takeuchi et al., 1973]. Since then, in-situ TEM has been widely developed and has become a versatile investigation technique to study (size dependent) dislocation behavior, grain boundary interaction, etc., as reviewed in [Legros, 2014], [Yu et al., 2015], [Kraft et al., 2010] where the latest advances in this field are reported. The success of in-situ testing is mainly attributed to the milestones in the development of MEMS (microelectromechanical systems) devices, which are now implemented in TEM sample holders as capacitive sensors but also as push-to-pull devices. Furthermore, focused ion beam (FIB) machining allows a precise and selective sample preparation down to the sub-micron scale. While in-situ TEM deformation is widely used to understand deformation processes in a wide range of materials. To date only few in-situ fatigue TEM experiments exist [Zhong et al., 2006] [Hosseinian and Pierron, 2013] and fatigue or crack propagation testing of interfaces in bi-layer and multi-layer materials has been mainly conducted at higher length scales under the SEM [Völker et al., 2015].

In the present chapter a design for an in-situ fatigue setup is presented allowing to test specific interfaces by machining a micron sized fatigue specimen with a sharp notch, to force crack propagation at the Al-Al₂Cu interface under repeated loads.

It is aimed at understanding the role of the interface, which separates the material, where the crack initiates (that is aluminum) and the neighboring material, Al₂Cu and to further observe how the materials contribute to the crack evolution under cyclic deformation. To combine both questions an in-situ test setup was chosen, where the investigated materials Al and Al₂Cu separated by an interface are cyclically loaded and observed simultaneously by means of TEM. In the first section in 5.1 the specimen design and the idea of the fatigue setup are presented. In 5.2 the results from the in-situ fatigue experiment are shown, where five stages from the first loading cycle to final failure are observed and described.

5.1 Specimen design

In this study crack initiation and propagation properties of the aluminum-Al₂Cu interface are investigated and the involved physical mechanisms are observed in-situ under TEM. Therefore, an electron transparent lamella is extracted from a

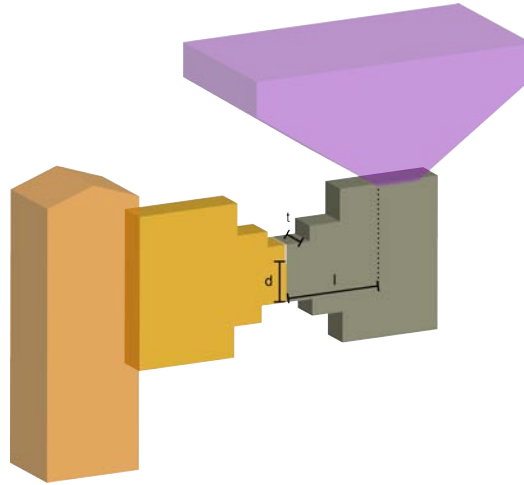


Figure 5.1: In-situ TEM fatigue setup: Cantilever-type TEM lamella displaying notch geometry at tested interface of two adjacent materials. One side of the specimen is fixated to the Omniprobe sample holder, the free-end of the specimen is cyclically indented with a picoindentation diamond tip.

metallographic cross section of the previously described (see.3.4.1) highly aged (200 °C 2000h) Cu-Al ball bond interface. The lamella is shaped to a miniaturized, cantilever-type fatigue lamella, which is cyclically bent by means of a picoindenter at its free end. A small notch is introduced at the edge of the gauge section, to study the toughness of the Al-A₂Cu-interface. Specimen geometry and indentation set-up are schematically illustrated in Fig. 5.1.

For the specimen preparation a FEI Strata 235 dual beam Focused Ion Beam (FIB) was used and observed in a field emission scanning electron column. The key steps of the specimen preparation procedure are summarized in Fig. 5.2. First, a trench is cut out of the metallographic cross section (a) followed by a lift-out procedure carried out with an Omniprobe micromanipulator tool. Then, the lamella is mounted and fixated on the Omniprobe transmission electron sample holder where the investigated interface is oriented relative to the prospective loading axis (b). Finally, the lamella is cut into its desired shape, where the geometry of the gauge section is oriented as the interface (c, d).

A Hysitron PI95 sample holder equipped with a picoindentation diamond tip is employed for the fatigue experiment, as shown in Fig. 5.3, which is operated under load control and records the corresponding displacement behavior.

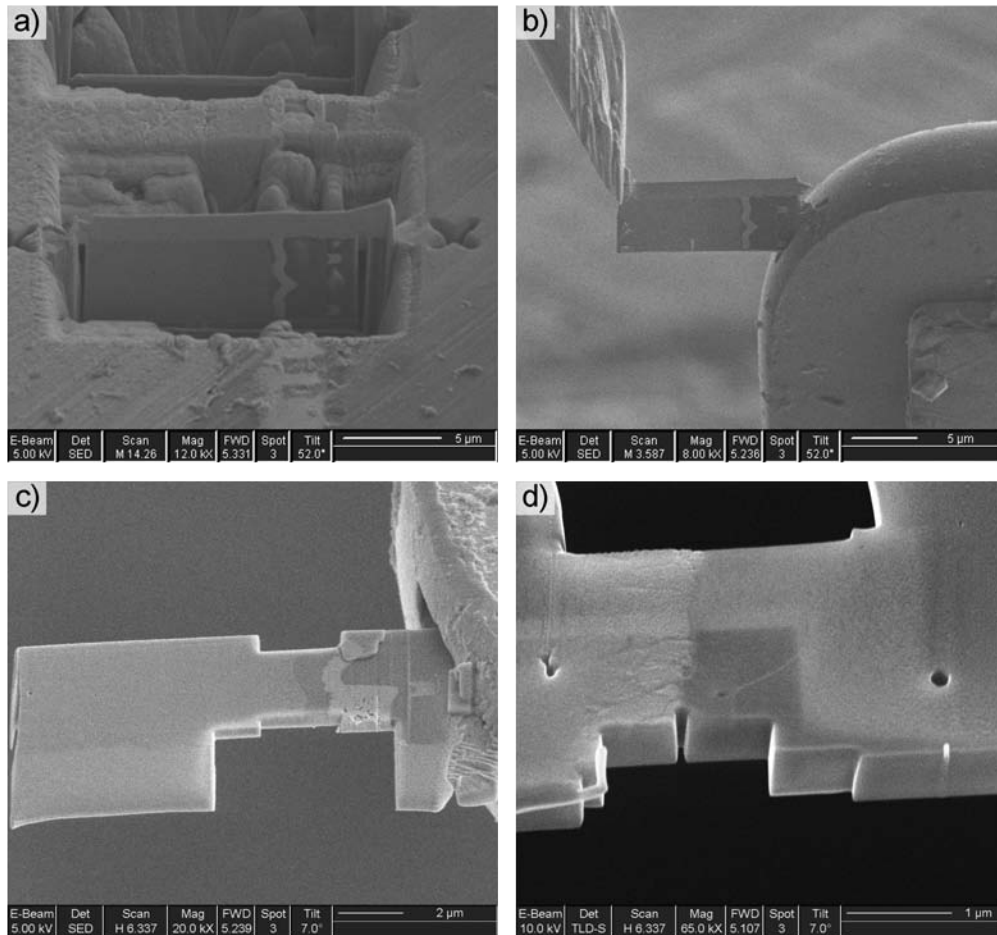


Figure 5.2: Preparation of in-situ fatigue test specimen during omniprobe lift out and FIB cutting: (a) Liftout cut for future lamella, (b) Omniprobe lift out of lamella and positioning to omniprobe sample holder, (c) FIB cut fatigue specimen with testing interface in center of gauge section, (d) Close up of notched specimen, where notch is located at interface to force crack propagation.

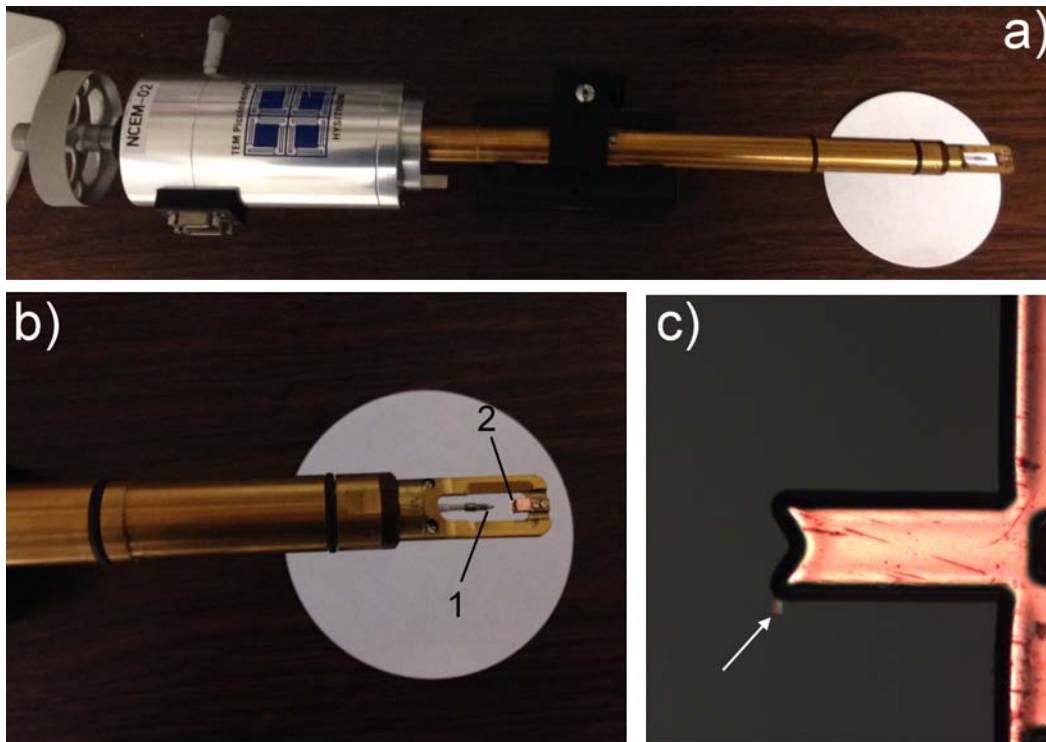


Figure 5.3: Hysitron PI95 picoindenter aligned to perform in-situ deformation experiments under TEM: (a) overview, (b) close-up showing (1) indenter tip (2) specimen holder, (c) optical microscopy image showing TEM lamella for in-situ fatigue test.

5.2 In-situ fatigue experiment

The fatigue experiment is observed by means of a JEOL 3010 transmission electron microscope, which operates at 300 kV enhancing a higher penetration of electrons through the relatively “thick” metallic specimen. A lamella thickness of approximately 300 nm was chosen to avoid buckling of the sample during the test. After TEM alignment the indenter tip is positioned close to the free-end of the small cantilever specimen, which requires precise alignment. To ascertain that indenter and lamella are in the same planar axis, both are brought into the position of minimal contrast. Then, to ensure the onset of loading, the indenter is smoothly brought into contact with the lamella, where small loads can be recorded. Once the pre-adjustments are conducted, the fatigue experiment can start. A low magnified TEM image of the specimen setup under the microscope is shown in Fig. 5.4. A to-and fro motion of the indenter tip results in a mode I loading of the interface. Thus, a load controlled cyclic loading condition is programmed, leading to a load maximum of 100 μN and a load minimum of 10 μN , which corresponds to a load ratio $R = 0.1$. Each cycle lasts two seconds and consists of a loading (up to maximum preset load) and unloading (to the minimum preset load). The load and resulting displacement profile of the fatigue test run including representative figures of the fatigued specimen is depicted in Fig. 5.5.

The fatigue process of the Al – Al₂Cu – specimen in this experiment can be summarized by five characteristic stages:

Stage i In the first stage of the cyclic loading experiment an – almost – purely reversible deformation behavior of the specimen is observed, denoted by a constant displacement amplitude, which ranges from cycles 0 – 100.

Stage ii Crack nucleation and slow crack propagation occurs, ranging from cycle numbers 101 – 160.

Stage iii Steady crack growth and identification of multiple crack branching during cycles 161 – 280.

Stage iv Unstable and “catastrophic” crack growth occurs in the last cycles from 281 – 295.

Stage v The end of the fatigue experiment is denoted by total rupture of the specimen, which occurred during cycles 296 – 300.

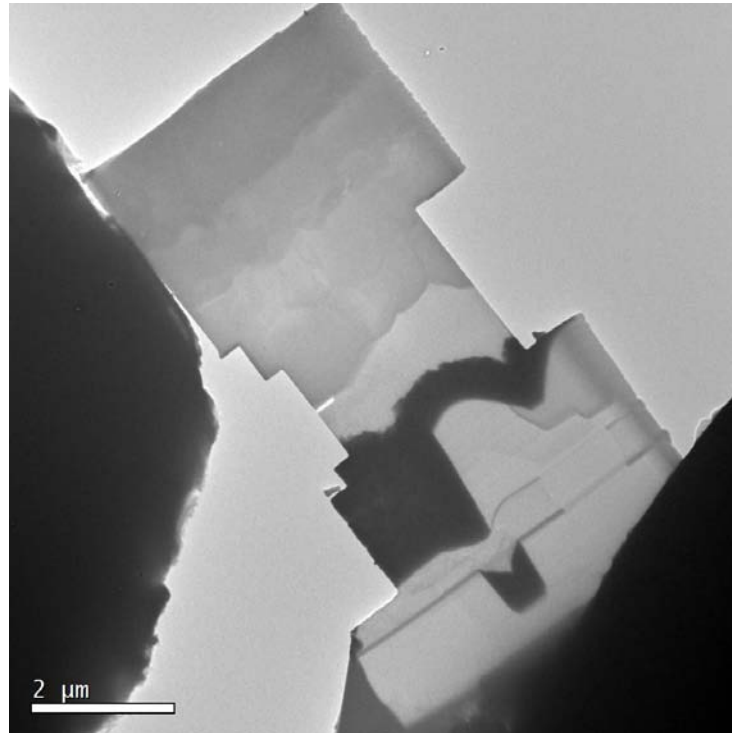


Figure 5.4: Setup overview transmission electron microscope.

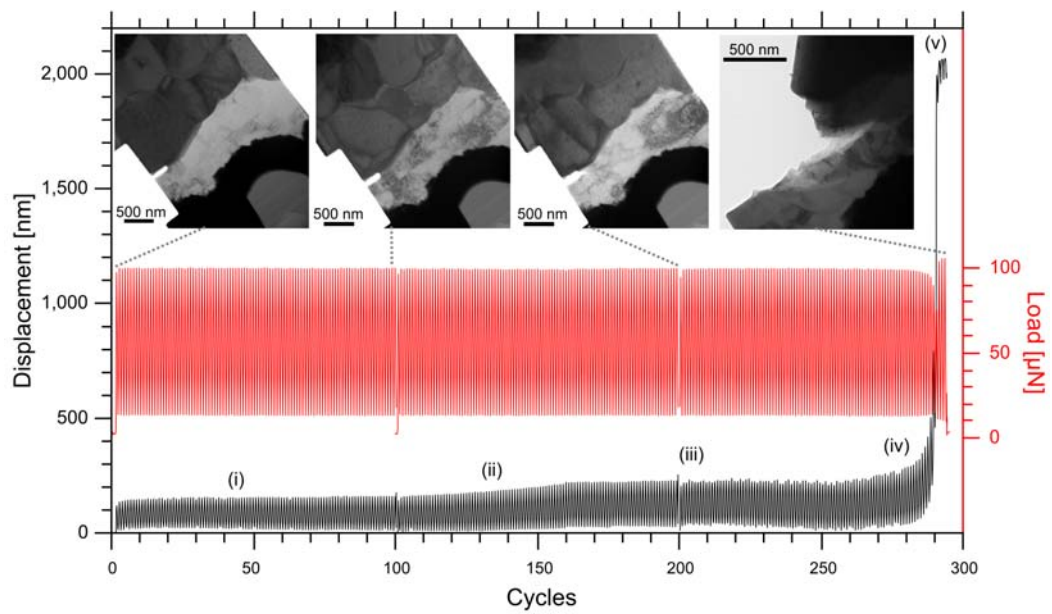


Figure 5.5: Load curve vs. number of loading cycles and corresponding displacement measurement vs. number of loading cycles

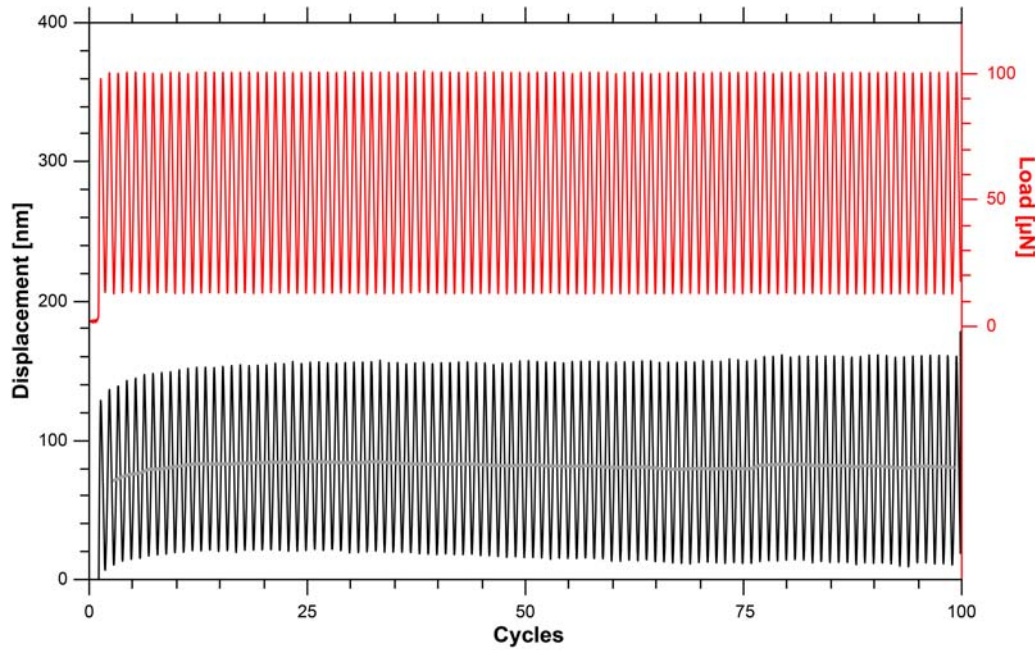


Figure 5.6: Fatigue experiment cycles 0 – 100: close-up of load and displacement curve vs. number of loading cycles.

5.2.1 Stage i – reversible (elastic) cyclic loading

In Fig. 5.6 the load and displacement curves of the first 100 loading cycles of the fatigue experiment are shown. The pre-adjusted, constant loading condition – 100 μN loading and 10 μN unloading resulting in a $R = 0.1$ load ratio of the fatigue experiment – could be maintained accurately during the experiment. The corresponding displacement curves, which were simultaneously monitored show a perfectly reversible behavior leading to a displacement amplitude of approximately 150 nm per cycle. In Fig. 5.7 characteristic screenshots of the in-situ observation of the experiment are shown. Three selected loading cycles – cycle number 2, 67 and 100 – are shown, where the load maximum is compared to the load minimum. Along the experiment no deformation of the notch such as closing or opening at the Al-Al₂Cu interface was observed. Main deformation was observed in the soft aluminum, where high dislocation densities appear and vanish during loading and unloading. It has to be noted, that very few dislocations were also observed in the Al₂Cu intermetallic. Fig. 5.7 illustrates the final condition of the specimen after 100 loading cycles, where only few permanent dislocations can be identified.

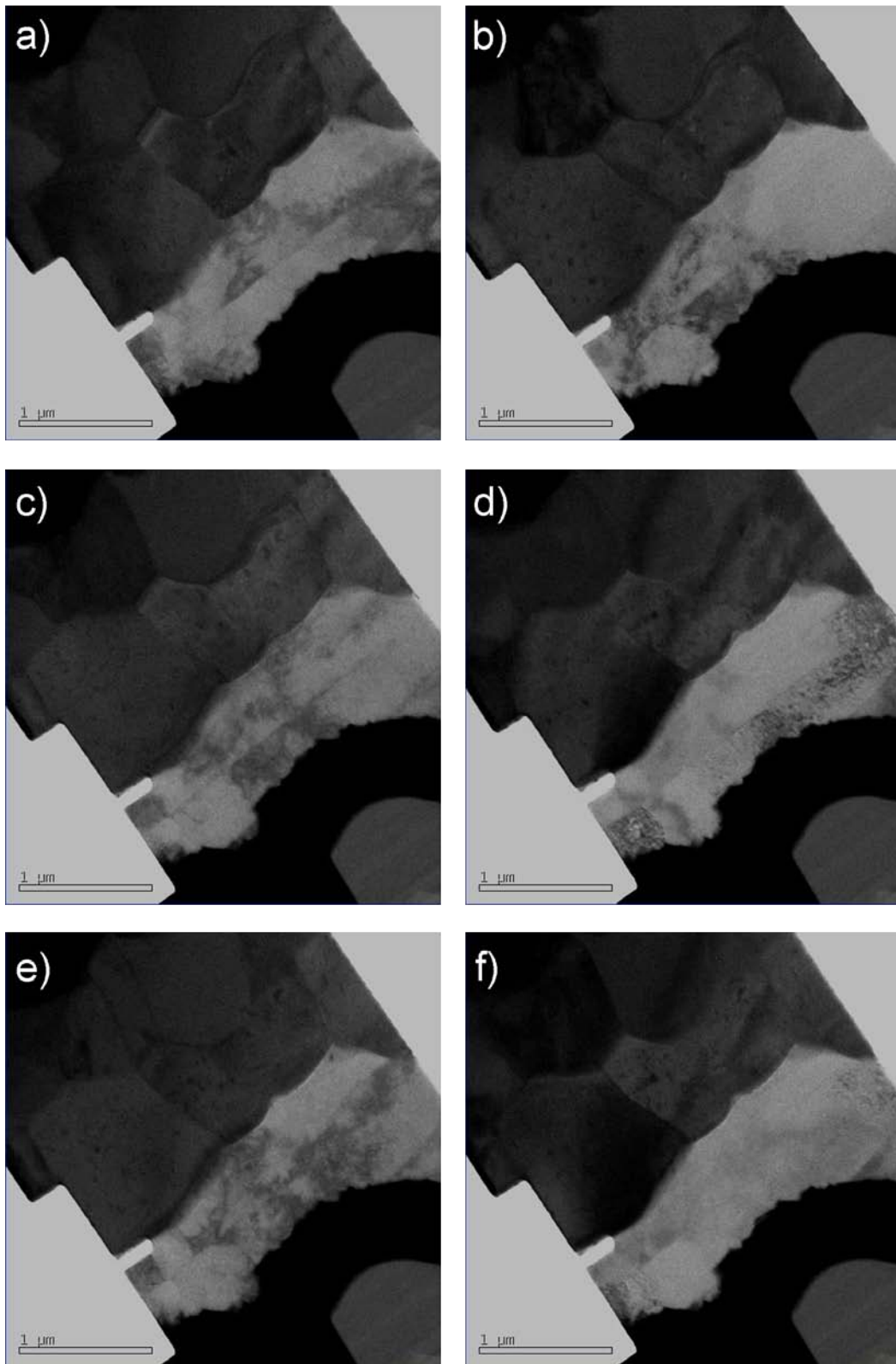


Figure 5.7: Selected screen shots of in-situ cyclic loading of Al-Al₂Cu-interface at different loading cycles: 2nd loading cycle: (a) loading and (b) unloading; cycle number 67 (c) loading and (d) unloading; cycle number 100: (e) loading and (f) unloading.

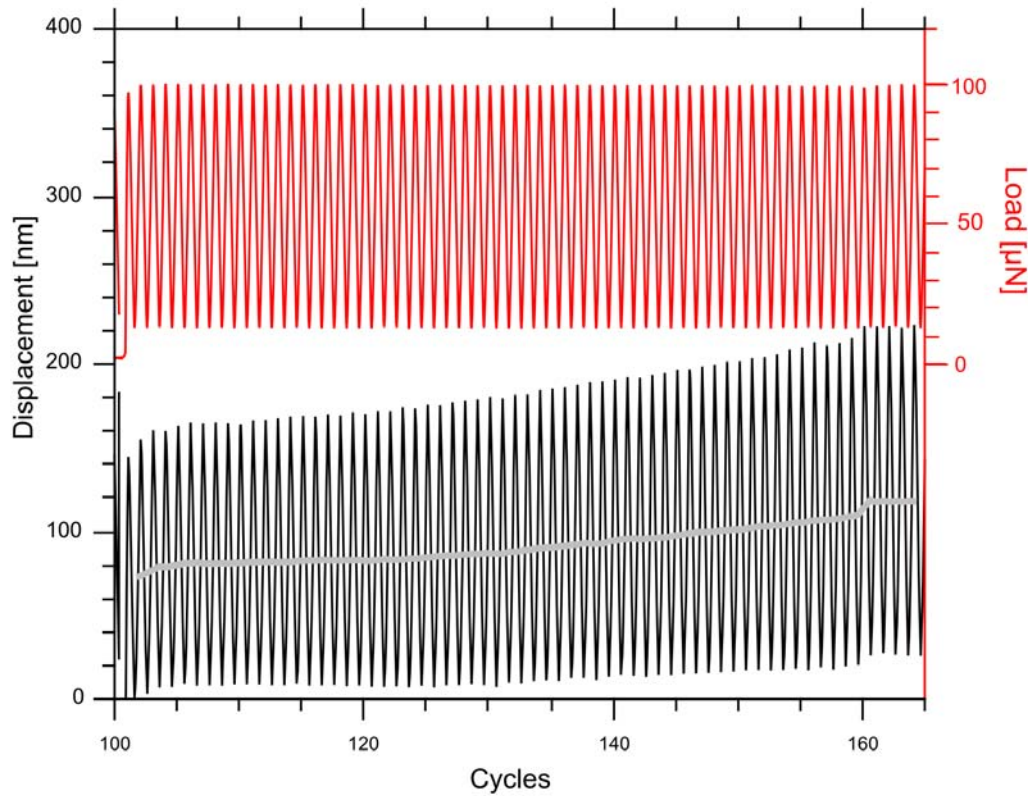


Figure 5.8: Fatigue experiment cycles 100 – 165: close-up of load and displacement curve vs. number of loading cycles.

5.2.2 Stage ii-crack initiation and slow crack propagation

In the second part of the fatigue experiment, which encompasses 100 – 165 loading cycles at the same load condition, crack nucleation and slow crack propagation are observed. Again, the load curve reflecting this section of the experiment in Fig. 5.8 proves constant and defined loading conditions throughout the experiment. The displacement curve however shows a steady increase in the displacement amplitudes, which indicates further deformation and could be correlated to the crack initiation process involved in Fig. 5.9, which could first be identified at cycle 131. The following cycles up to approximately 160 do not reveal any changes in the crack length or shape as can be seen in Fig. 5.10.

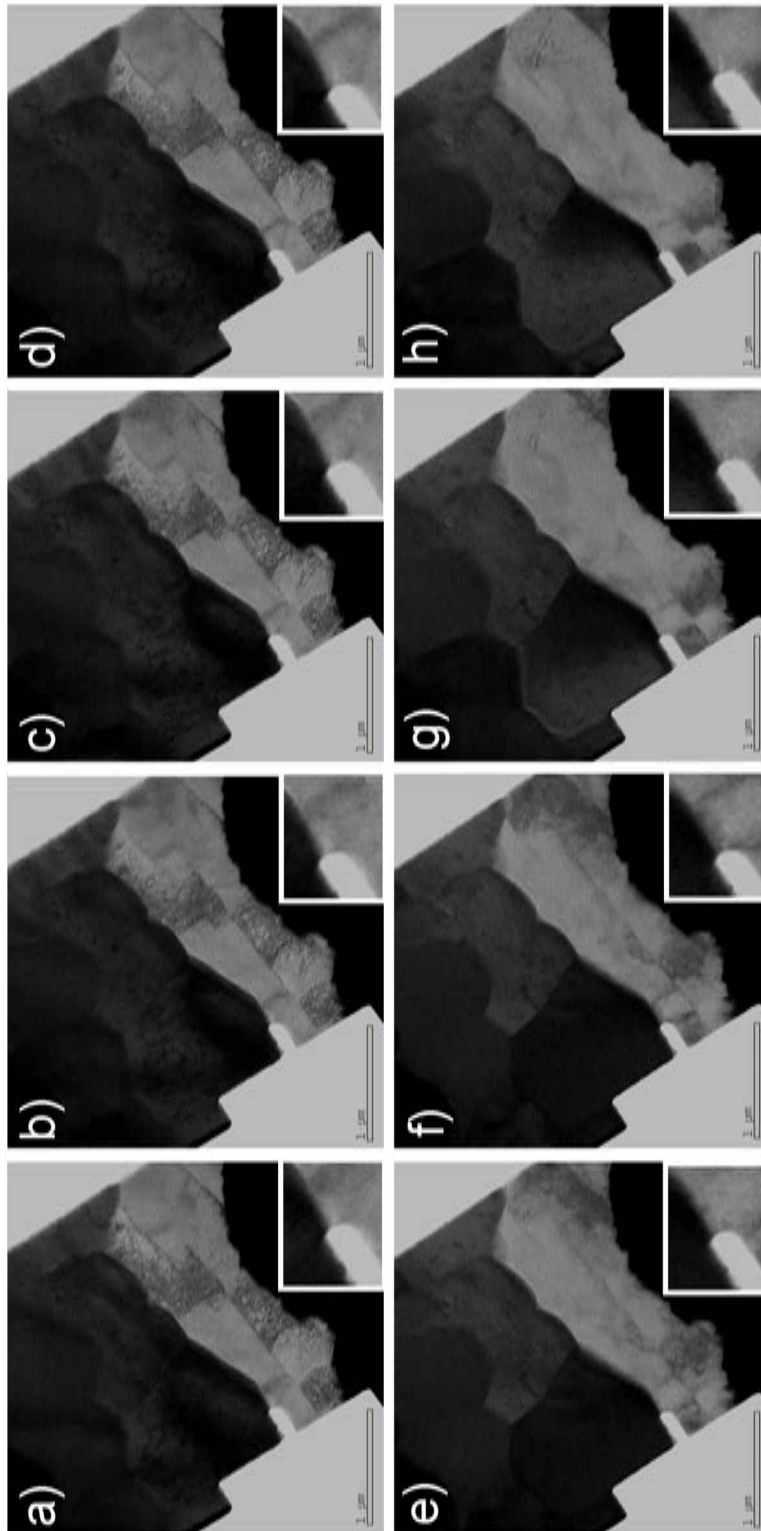


Figure 5.9: Crack initiation: (a-d) loading conditions with respective unloading conditions (e-h). Cycle 127: (a,e) high dislocation density in aluminum; Cycle 130: (b, f) cycle prior to crack initiation; Cycle 131: (c,g) crack can be identified in the vicinity of the notch; Cycle 132: (d, h) Same crack condition.

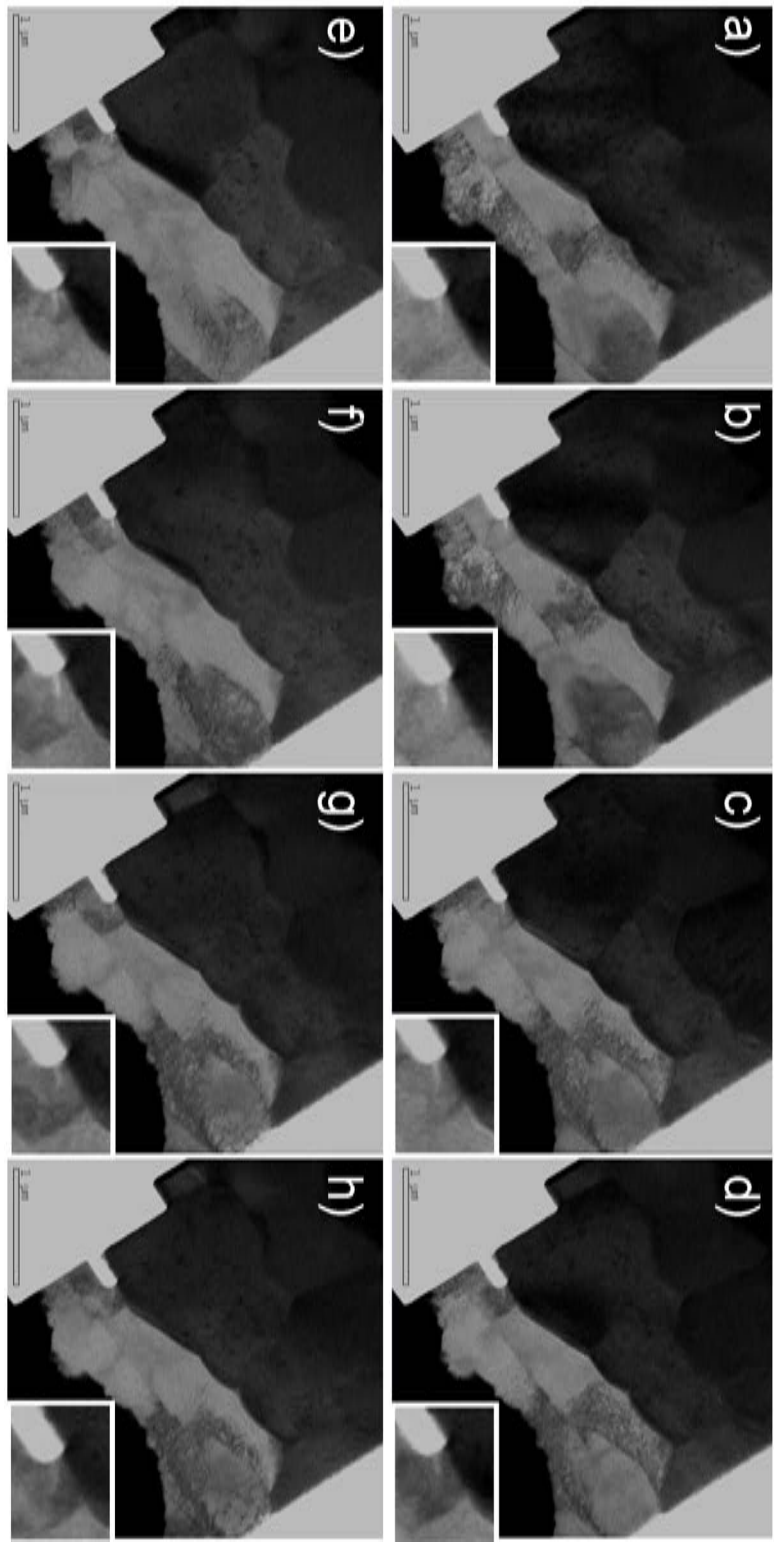


Figure 5.10: Constant crack length during further cycling: (a-d) loading and corresponding unloading conditions (e-h). Cycle 141: (a,e) ; Cycle 151: (b, f) ; Cycle 157: (c,g); Cycle 161: (d, h).

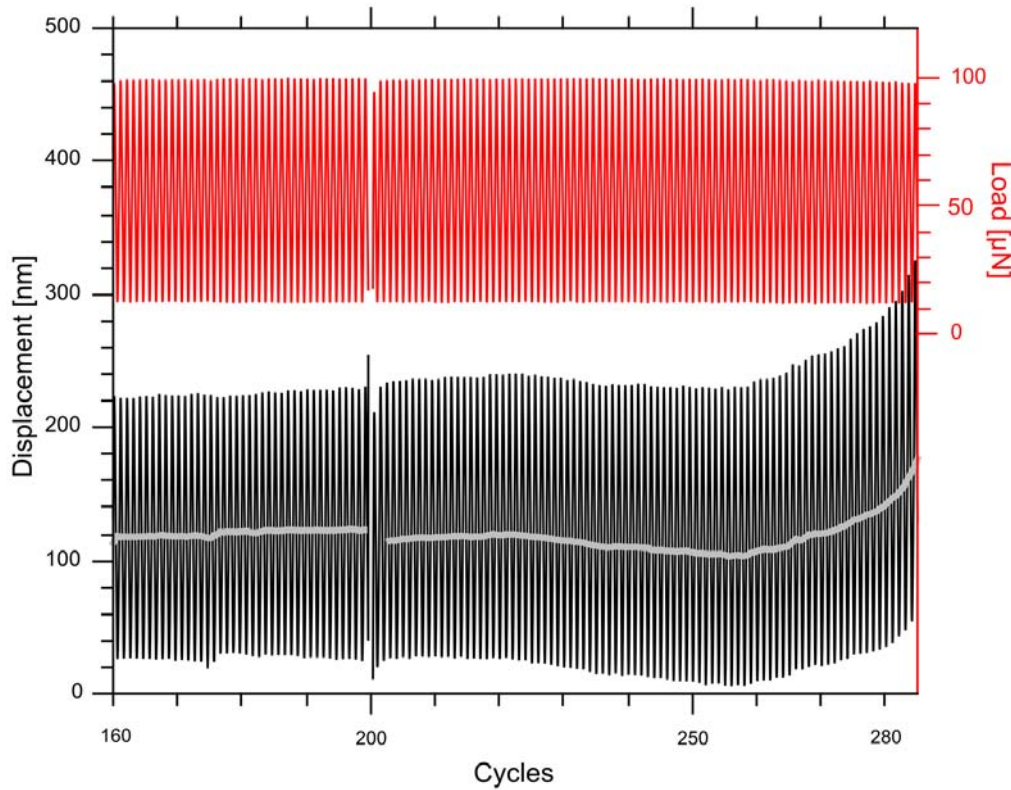


Figure 5.11: Fatigue experiment cycles 160 – 285: close-up of load and displacement curve vs. number of loading cycles.

5.2.3 Stage iii: Slow crack growth

In the third stage slow crack growth is observed, which approximately lasts 125 cycles and encompasses one third of the entire fatigue experiment. Thus, it may be concluded that crack propagation is the main contribution in the fatigue experiment. In this part of the experiment the crack, which initiated in an aluminum grain in the vicinity of the notch and branches towards the aluminum layer and grows within the first grain. Characteristic loading and unloading conditions are summarized in Fig. 5.12. The majority of the cycles show a crack opening at the load maximum and a closing in the unloading state. Few cycles (approximately 10) were observed, where the wake of the crack remains closed during loading (see Fig. 5.12b and e).

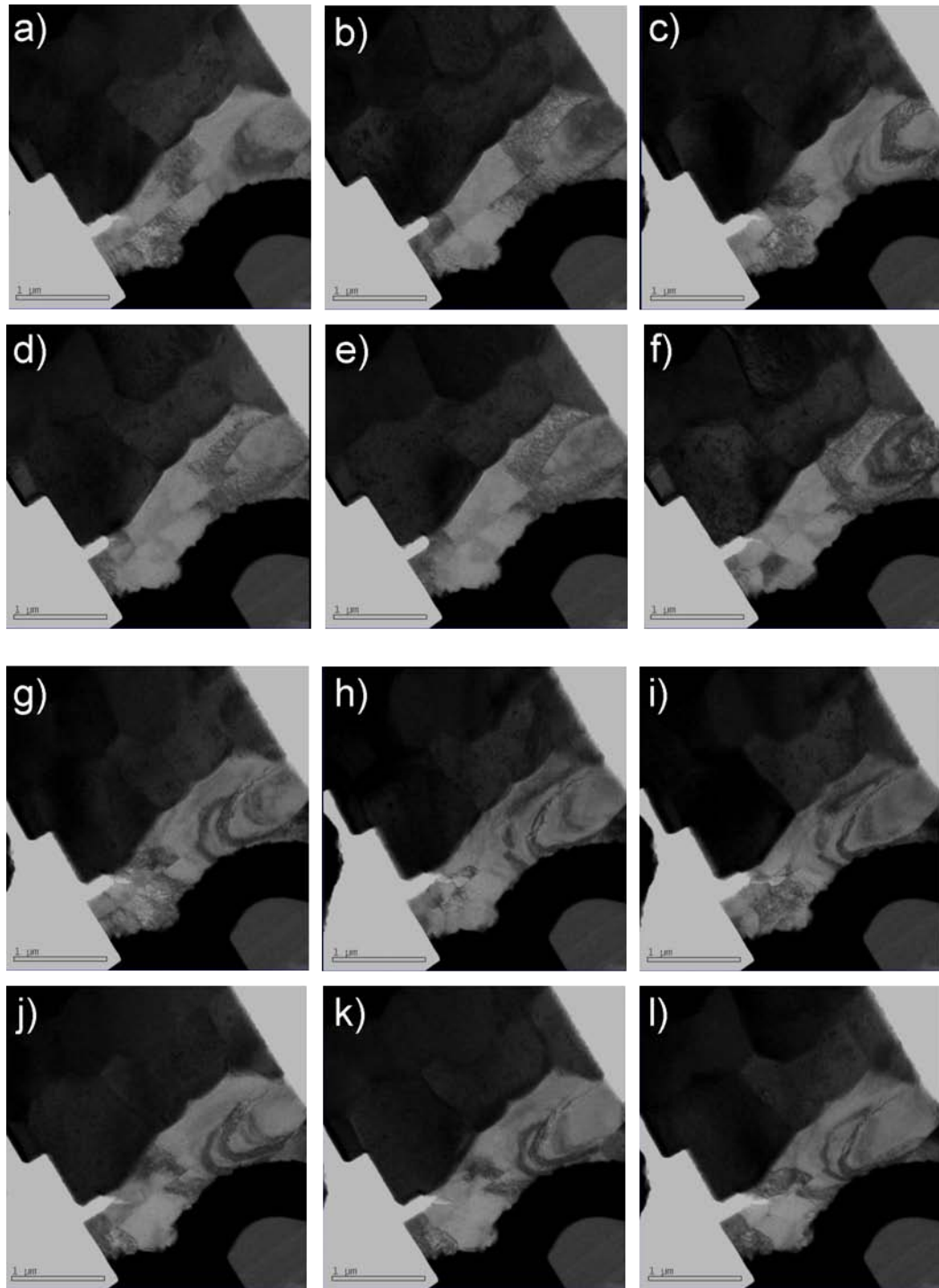


Figure 5.12: Key steps in slow crack propagation regime: Crack grows inwards the aluminum, grain boundary in Al serves as obstacle for further crack growth. Selected cycles in loading and unloading condition: (a-c): loaded and (d-f) corresponding unloaded states; (g-i) loaded and (j-l) unloaded.

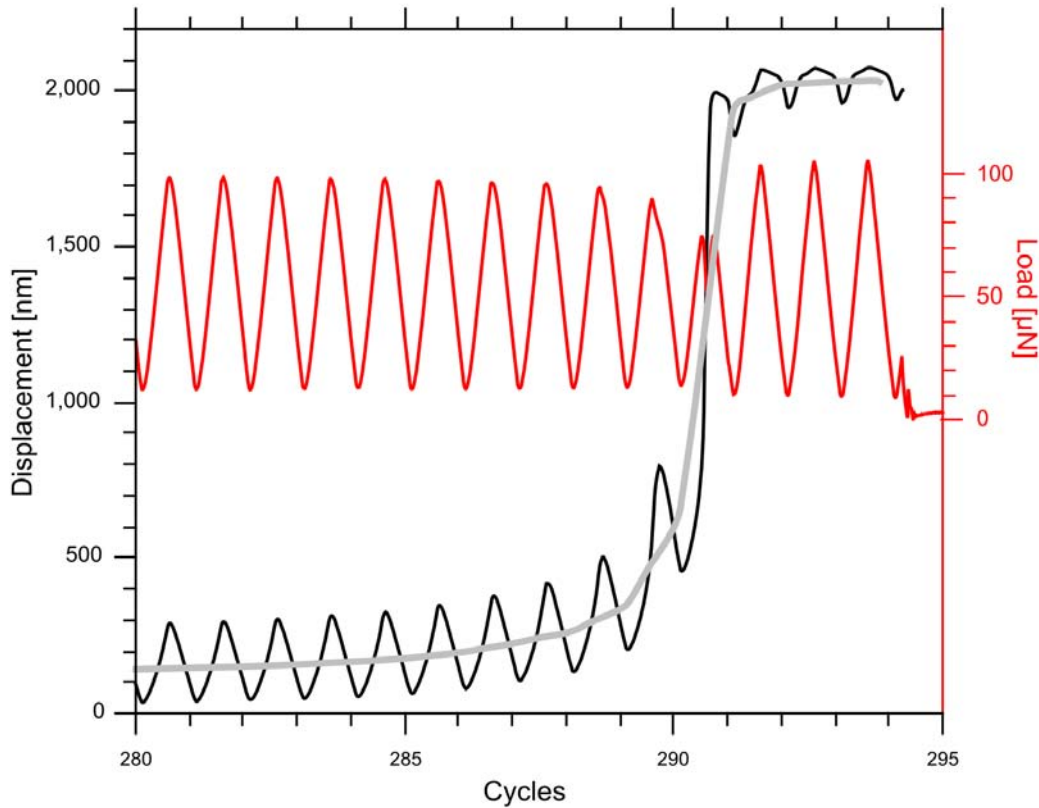


Figure 5.13: Fatigue experiment cycles 280 - 295

5.2.4 Stage iv & Stage v: Rapid crack growth and catastrophic failure

In the fourth stage rapid crack growth occurs once the crack overcomes the grain-boundary, which represented a major obstacle in the previous stages. Once the grain boundary is passed, crack growth and propagation are unstable and high deformations in the wake of the crack tip can be identified. Thus, this stage is particularly short and only lasts approximately 15 cycles and result in total rupture of the lamella. The final fracture – stage v – is shown in Fig. 5.14, where a highly deformed aluminum residual is shown. Several shear features indicate that aluminum failed in a ductile way, where multiple cracks branched during the experiment.

Fig. 5.16 represents the crack growth as a function of loading cycles to failure including representative images of the loaded in-situ fatigue experiment.

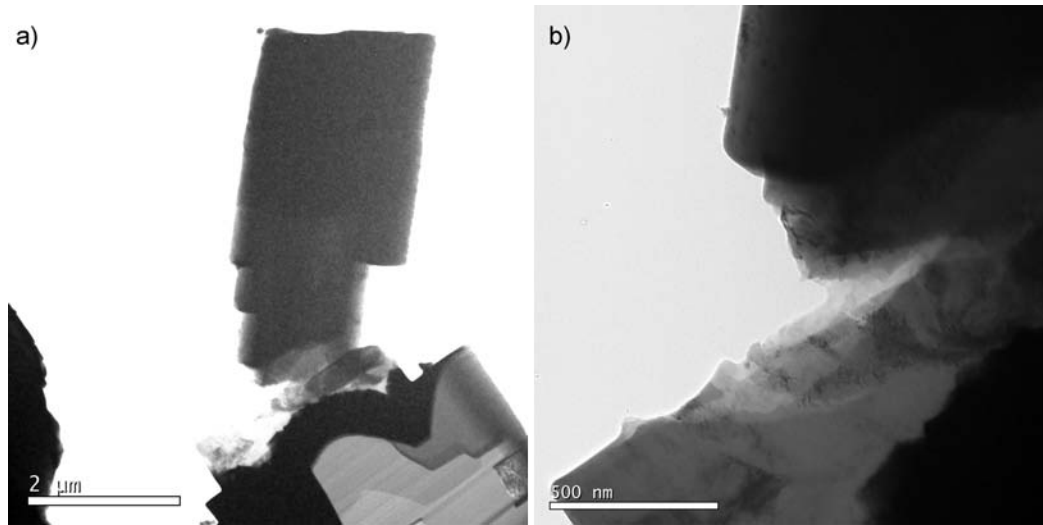


Figure 5.14: Final failure of fatigue experiment.

5.3 Summary

For a closer understanding of crack propagation and crack deflection behavior of the Al-Al₂Cu interface as observed in the previous studies (see chapter 3 and chapter 4) to be involved in the initial crack formation, an additional more detailed investigation was undertaken. One aim was to study the role of that interface under cyclic loading to determine the weakest site responsible for fatigue failure. For this purpose an electron transparent lamella was extracted from a highly aged miniaturized Al-Cu ball bond interface, where the intermetallics Al₂Cu, AlCu and Al₄Cu₉ are present in addition to the parent materials. A gauge section has been shaped by means of focused ion beam techniques, and a notch was introduced at the edge of the interface to force crack initiation at the interface or in the vicinity thereof. Surprisingly, it was found that the notch did not force crack propagation along the interface, but in the aluminum grain in the vicinity of the notch, where a dislocation concentration could be identified. The crack fully developed within this aluminum grain and entirely evolved through the aluminum. Once the crack encountered the grain boundary, a retardation of further crack growth could be observed. Thus, the grain boundary acted as a main obstacle, leading to retardation of the crack evolution for several cycles. Once the grain boundary was overcome, catastrophic crack growth occurred leading to total failure within the aluminum layer. Though the crack propagation processes could solely be observed within the

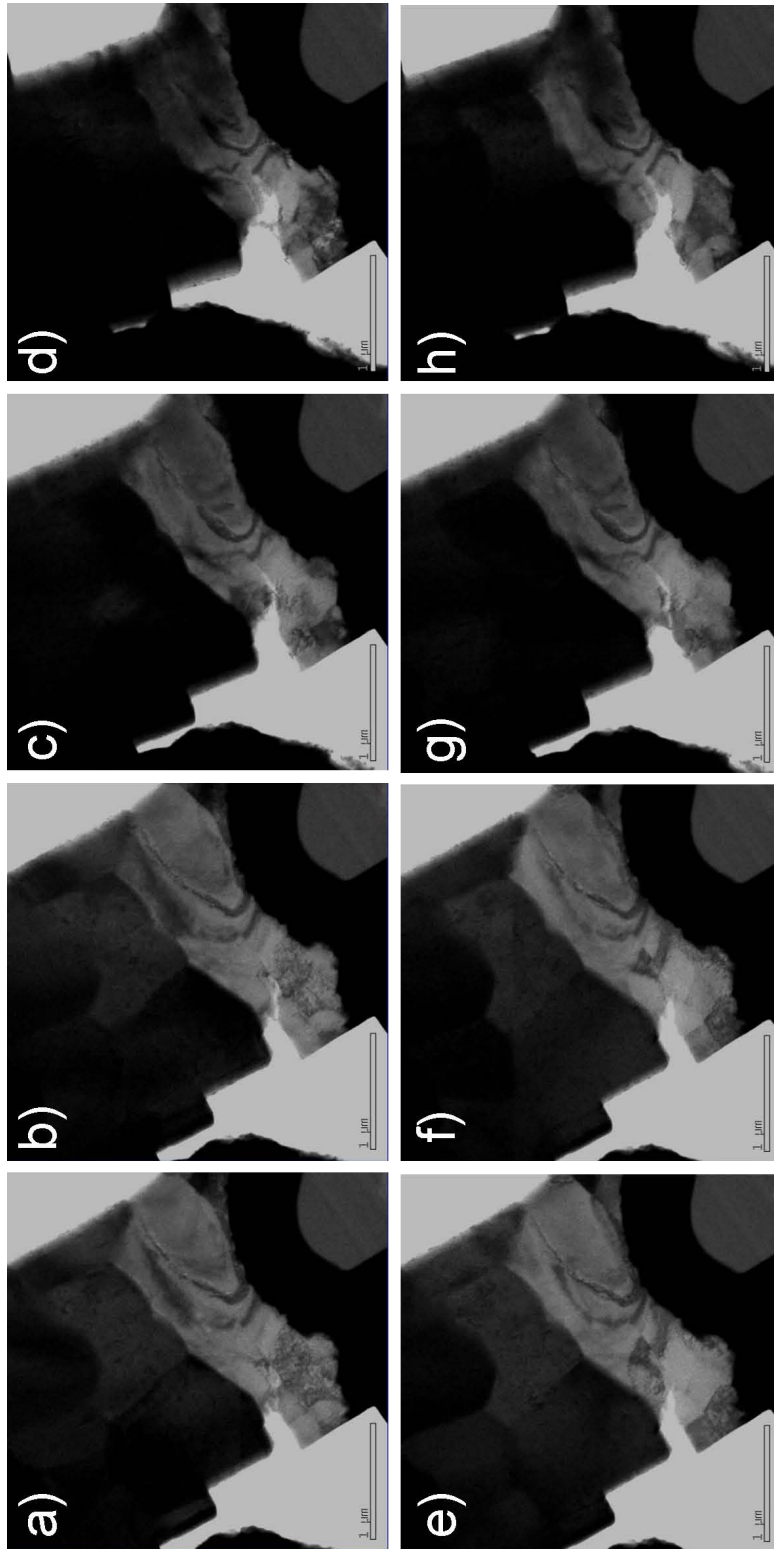


Figure 5.15: Rapid crack growth in the last cycles of the fatigue experiment: (a-d) loading and (e-f) corresponding unloading.

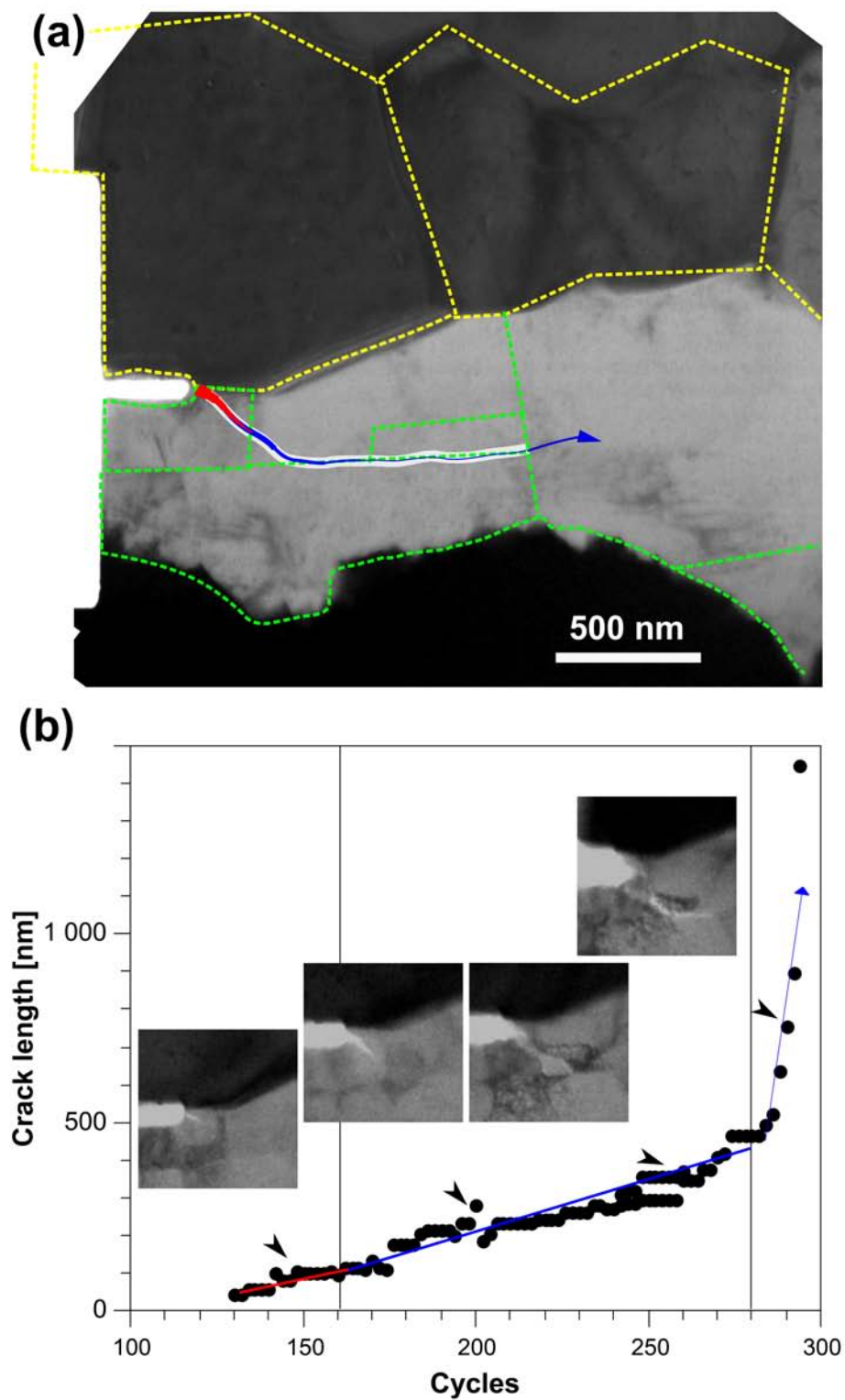


Figure 5.16: Crackpath during in-situ experiment

aluminum it was also found that high stresses occurred in the neighboring Al_2Cu grains. Thus it can be concluded that the resistance of the brittle intermetallic phase against plastic deformation increases the stresses in the vicinity of the crack, which leads to early failure of the specimen in the aluminum. Thus, this experiment is in agreement with the results of preceding miniaturized and bulk high cycle fatigue experiments.

6 General summary and conclusion

The combination of different metallic materials to bimetallic bonds is of high technological significance as it is widely employed in various applications due to the particular physical properties. One key application is for example Al-Cu wire bonds, which connect microelectronic devices to their outside circuitry.

When these bonds are subjected to elevated temperatures, interdiffusion of both materials into each other occurs, leading to the formation of intermetallic compounds at the bond interface. It is well known that such intermetallic compounds feature disparate physical properties compared to the parent materials, copper and aluminum. Thus, an overall change of the Al-Cu bond reliability is expected as Al-Cu intermetallics are known to be harder, denser and more brittle than the ductile aluminum and copper. An increased brittleness is typically associated with a drastic decrease of the toughness of a material, thus a high degree of formation and growth of intermetallic compounds at the Al-Cu interface leads to a reduced damage tolerance and a general degradation of the bond. While the physical and mechanical properties such as the Young's modulus, indentation fracture toughness, hardness and density of Al-Cu intermetallics have been thoroughly characterized in literature, only few studies exist on the fatigue and static fracture behavior of Al-Cu bonds with high intermetallic compound evolution. In service above-mentioned bonds are not only subjected to elevated temperatures but also to various cyclic loads, which may be caused by mechanical vibrations or thermo-mechanically induced leading to cyclic stresses at the bond interface.

Because of the reasons mentioned, it was the **main aim of this thesis** to investigate the **mechanical fatigue behavior of such bonds in as-bonded condition** and, as a second step, to further study the **impact of interfacial intermetallic compound evolution** on the mechanical fatigue behavior.

Another aim of this thesis was to reveal the **fracture mechanisms occurring in bimetallic Al-Cu interfaces under cyclic loading**, again with the aspect to quantify the **influence of intermetallic compound evolution**.

To realize these aims, this **thesis** has been divided in **three parts**:

The first part was concerned with a technological application, with the goal to measure for the first time the **fatigue behavior of thermosonic wire interconnects** made of copper wires bonded on aluminum pads. These interconnects are used by standard in the microelectronics sector. State-of-the-art test methods to assess the bond reliability of such miniaturized bimetallic joints are static destructive shear tests, which do not reflect the service conditions nor do they give any information on the mechanical fatigue behavior of such bonds; thus, a specially designed accelerated fatigue test setup had to be developed in the frame of this work. This setup consists of a novel ultrasonic resonance fatigue system in combination with a special, solder-based specimen preparation allowing to induce cyclic mechanical stresses at the bond interface. Two approaches were achieved in this work: A single bond test technique, which allows to study the mechanical fatigue behavior of each bond individually, and a multiple bond test technique allowing to assess the average fatigue behavior of several bonds located on the investigated device. The end of life was determined by a so-called fatigue lift-off failure, where the specimens are detached at the bond interface due to cyclic loading. Finite element computations proved that the lifetime curves from both of these techniques are in similar ranges when they are part of plots of von Mises-stress vs. loading cycles to failure. One focus of the first part of this thesis was to **study the role of intermetallic compound formation** on the mechanical fatigue behavior of thermosonic Al-Cu bonds. Therefore three microstructural states obtained by isothermal annealing of the bonds were investigated: (i) the as-bonded state, (ii) an intermediately aged state and (iii) a highly aged state. In case of (ii) two intermetallics, Al_2Cu and Al_4Cu_9 , and in case of (iii) even three intermetallics, Al_2Cu , AlCu and Al_4Cu_9 developed. While ball shear tests did not reflect the application relevant loading conditions and impact of interfacial evolution on the reliability of a bond, fatigue tests proved a clear degradation with increased intermetallics formation. Characteristic **fracture morphologies** revealed two stages to occur during fatigue failure not at least due to the specific geometry of the ball bonds: (i) crack propagation and (ii) final fracture. It turned out that the crack path highly depends on the microstructural evolution of the bond. However, in final fracture or when the Al pad material is entirely consumed, interfacial intermetallics are responsible for failure. The failure mechanisms can be summarized as follows:

as-bonded: (i) crack propagation in Al pad (ii) final fracture at the original Al-Cu

bond interface

200 °C, 200 h: (i) crack propagation in Al pad (ii) final fracture at the interface between Al_2Cu and Al_4Cu_9

200 °C, 2000 h: (ia) crack propagation in remaining Al and deflection (ii) at the interface between Cu and Al_4Cu_9 (ii) final fracture in AlCu

It has been shown that the crack propagated through the Al pad material; final fracture, however, occurred in the most brittle site. This study revealed that lifetime of Al-Cu bonds is directly related to the amount of residual aluminum pad metallization.

In the second part of this thesis the aim was to **mimic the highly aged microstructure** of the miniaturized ball bonds **by bulk samples**, in order to test the high cycle fatigue properties of the Al-Cu multilayer under well-defined loading conditions. Combinations of the mode I (tension-compression) and mode II (shear loading) could be realized. To optimize the fatigue test conditions, preliminary diffusion bond experiments were conducted. Because bulk, flat, parallel and thoroughly developed intermetallic compound layers were required for the fatigue investigations, special diffusion bond treatments were achieved under accurate control of temperature (about 530 °C) and pressure (about 16 MPa for 180 min). As a final fatigue diffusion bond, a thin aluminum foil was placed between two bulk copper rods featuring the same intermetallic compounds as before: Al_2Cu , AlCu and Al_4Cu_9 . For the fatigue experiments, again a resonance fatigue system operating at 20 kHz was employed. Here, the bulk fatigue specimens were machined out of the diffusion couples and designed such that the longitudinal resonance condition of the fatigue setup has been fulfilled. The investigated diffusion zone was located at the strain maximum of the load train (i.e. in the center of the bond). The loading combination of mode I and mode II was realized by inclining the diffusion bond at a defined angle relative to the loading direction. To compare the fatigue properties of three datasets obtained by a certain inclination, the Rankine yield criterion was used since it is suited best for brittle materials. It was shown that this material combination is more susceptible to mode II (shear) loading than to mode I (tension-compression) loading. Furthermore, fractographic investigations showed that in the case of pure mode I fatigue loading, a clear fracture path was traced back: Again, crack initiation occurred in the aluminum layer in the center of the specimen, crack deflection and propagation occurred circumferentially in the

neighboring layer Al_2Cu . The final fracture was observed in the most brittle layer AlCu . In an additional study on fully aged specimens, it was shown that when the aluminum is entirely consumed under mode I-loading, a lower fatigue behavior results. The fractographs showed entirely brittle behavior.

The scope of the **third part of this thesis were in-situ transmission electron microscopic observations of the crack initiation and propagation** of the aluminum- Al_2Cu interface on a micron scale. Here, the fatigue test was conducted on a pre-notched, cantilever-shaped electron transparent lamella extracted from the highly aged miniaturized ball bond interface by means of focused ion beam. Cyclic testing of the $\text{Al-Al}_2\text{Cu}$ interface could be realized by the usage of a pico-indenter, which was implemented in the TEM sample holder. It was expected that crack propagation occurs along a pre-notched interface but, in contrast, the entire propagation process occurred in the aluminum. Therefore, also this result showed that – in accordance with all previous findings of this thesis - an interfacial crack in a ductile- brittle interface tends to propagate in the ductile layer.

In general, in all investigations of this thesis - in applying fatigue test techniques at different length scales - it was found that cracking is easiest to initiate in the most ductile layer. Moreover, it was found that intermetallic compound formation is detrimental for the fatigue behavior of Al-Cu bonds as it shows increasing brittleness and high intrinsic stresses caused by the disparate physical properties of each intermetallic within the material system.

7 Outlook

Each study gives rise to further investigations. Thus, an outlook for prospective investigations in this field shall be given hereafter:

Fatigue investigations of thermosonic ball bonds by means of a specially developed fatigue testing setup allowed to determine the weakest sites of the bond interface. Furthermore, this method proved a high microstructural sensitivity compared to the state of the art static ball shear tests. It could be shown that the accelerated fatigue test technique specially designed for miniaturized ball bonds serves as a rapid screening tool, which reflects accelerated loading conditions. Thus, this novel fatigue test method is a powerful tool, which can be implemented in prototyping of future bond technologies and material combinations. A further improvement of the suggested method would be the possibility to implement the effect of elevated temperatures during the fatigue tests.

In the second part of this thesis, the high cycle fatigue behavior of bulk, diffusion-bonded Al-Cu bonds featuring three different intermetallic compounds (Al_2Cu , AlCu , Al_4Cu_9) could be successfully tested. Extensive efforts in the specimen design led to a successful fatigue testing setup, which allowed to test these bonds under well-defined loading conditions being a combination of mode I and mode II loads by means of an ultrasonic resonance fatigue setup. Thus, a novel test method allowing to test various bulk joints under combined loads could be successfully created and is adaptable to further weld types and material combinations. Nevertheless, in the frame of this study on the high cycle fatigue behavior of bulk Al-Cu joints, the presented project gives rise to further investigations: First, it still needs to be clarified what the involved crack initiation mechanisms are and how many cycles of the lifetime are consumed for the initiation and propagation processes, therefore interrupted tests should be conducted in combination with metallographic sectioning to reveal the crack initiation site. A more sophisticated method to study the crack initiation studies would be 3-D computer tomographic methods, which allow

to observe these processes in-situ. Additionally, analyses of the mixed mode loading by Finite Element computations would be useful to understand the internal stresses as a function of the present intermetallic compounds. Furthermore, the fracture behavior of the highly inclined specimens needs to be clarified. A further interesting investigation could be to measure crack propagation resistance curves, where miniaturized notches are introduced at the interfaces and within the material layers, in order to reveal the toughness of each material and the role of the neighboring intermetallic compounds under cyclic loads. Again, since such bonds are subjected to temperature extremes, it would be certainly of interest to conduct these tests at different temperatures.

The in-situ observations of the interfacial crack growth performed in the third part of this thesis were conducted for a better understanding of the micro-mechanisms of failure in the interface of miniaturized bi-materials. The chosen Al-Al₂Cu interface was examined since this material combination was found to be responsible for the fatigue behavior of the previously investigated samples, and due to its high relevance for microelectronic applications being a main subject of the present study. It would be definitely of utmost interest to repeat similar in-situ fatigue tests, where the notch is shifted either into the aluminum or in the intermetallic to observe the crack path and deflection. Furthermore these experiments can be extended to other interfaces and material combinations.

In the case of the investigated Al-Al₂Cu interface, another interesting question would be to directly compare if the presence of the brittle Al₂Cu promotes the crack growth in the aluminum due to increased stresses; in this connection, a comparative crack propagation study only in a pre-notched aluminum cantilever lamella would be of interest. The specimen preparation of the test lamella was conducted with a FIB with an Argon ion source. The heavy ion source may contaminate the specimens and influence their micromechanical behavior. An attractive alternative would be to prepare these specimens with Helium ions, which will probably be the future in the preparation of sensitive specimens for in-situ testing and transmission electron microscopy in general.

Acknowledgments

First, I would like to thank my supervisors at Univ.-Prof. Dr. Michael Zehetbauer and Dr. Golta Khatibi for their excellent supervision, valuable discussions, for giving me the opportunity to work on this topic and for allowing me to pursue my scientific ambitions.

Dr. Khatibi allowed me to work in the frame of the Comet K-project *Micromat*, where I could benefit from precious industrial cooperations and gain deeper insights into the booming semiconductor industry. Without her guidance and motivation this work would not have been possible.

At this point, I would like to thank our industrial partners from Infineon Villach, Dipl.-Ing. Rainer Pelzer and Dr. Michael Nelhiebel, for the good cooperation. Dr. Werner Robl from Infineon Regensburg organized the production of the “custom-made” soldering templates for multiple bond testing. Dr. Martin Lederer is acknowledged for the finite element computations.

I would like to thank Dr. Stephan Puchegger for his support at the SEM and Martina Rohrer for sample preparation.

At this point, I would like to express my gratitude to Prof. Tresa Pollock, University of California, Santa Barbara (UCSB), USA for hosting me as a guest researcher in her group. I am grateful for her openness to this topic and for her generous guidance. I would also like to cordially thank Chris Torbet, who supported me wherever he could on the multiple technical issues I encountered and for his enthusiasm to ultrasonic fatigue.

For the in-situ experiments conducted at the Molecular Foundry (formerly: NCEM) of Lawrence Berkeley Laboratory in Berkeley, California I would like to thank Dr. Christoph Gammer.

Finally, my warm thanks go to all my colleagues I came across in the following research groups: Physics of Nanostructured Materials group (University of Vienna), the Pollock group (UCSB) and the Mechanical Response of Materials group (University of Technology, Vienna). I am also grateful for the collegial discussions with

my former PhD mates and friends Dr. Johanna Akbarzadeh, Dr. Tamara Pinterich and Dr. Jelena Horky.

Finally, I would like to thank my family and friends for support.

My loving thanks go to Christoph, who has always been a great inspiration in the past years.

The following funding sources made my research possible: The Austrian Research Promotion Agency (FFG) and the Vienna Business Agency (ZIT) in the frame of the research project *Micromat* and the Marietta Blau scholarship awarded by the Austrian the Federal Ministry of Science and Research (BMWF).

Bibliography

- [AST, 2015] (2015). ASTM Standard E8/E8M-15a, Standard Test Methods for Tension Testing of Metallic Materials, ASTM International.
- [Akiniwa et al., 2008] Akiniwa, Y., Stanzl-Tschegg, S., Mayer, H., Wakita, M., and Tanaka, K. (2008). Fatigue strength of spring steel under axial and torsional loading in the very high cycle regime. *International Journal of Fatigue*, 30(12):2057–2063.
- [Albert, 1838] Albert, W. A. J. (1838). Ueber Treibseile am Harz. *Archive fuer Mineralogie, Geognosie, Bergbau und Huettenkunde*, 10:215–234.
- [Amistoso and Amorsolo, 2010] Amistoso, J. O. S. and Amorsolo, A. V. (2010). Thermal Aging Effects on Cu Ball Shear Strength and Cu/Al Intermetallic Growth. *Journal of Electronic Materials*, 39(10):2324–2331.
- [Anderson, 2005] Anderson, T. L. (2005). *Fracture Mechanics Fundamentals and Applications*. Taylor and Francis Group, Boca Raton, third edition.
- [Basquin, 1910] Basquin, O. H. (1910). The exponential law of endurance tests. In *Proceedings of the American Society for Testing and Materials*, volume 10, pages 625–630.
- [Bauer and Lessmann, 1976] Bauer, C. L. and Lessmann, G. G. (1976). Metal-Joining Methods. *Annual Review of Materials Science*, 6(1):361–387.
- [Bisschop, 2007] Bisschop, J. (2007). Reliability methods and standards. *Micro-electronics Reliability*, 47(9-11):1330–1335.
- [Braunovic et al., 2010] Braunovic, M., Rodrigue, L., and Gagnon, D. (2010). Nanoindentation Study of Intermetallic Phases in Al-Cu Bimetallic System. In *Electrical contacts, 2008. Proceedings of the 54th IEEE Holm conference on*, pages 270–275.

- [Breach and Wulff, 2010] Breach, C. D. and Wulff, F. W. (2010). A brief review of selected aspects of the materials science of ball bonding. *Microelectronics Reliability*, 50(1):1–20.
- [Broek, 1986] Broek, D. (1986). *Elementary engineering fracture mechanics*. Martinus Nijhoff Publishers, Dordrecht, 4th edition.
- [Celik et al., 1997] Celik, S., Ay, I., and Otmanboeluek, N. (1997). Diffusion bonding of pure copper and aluminium in argon gas atmosphere. *Praktische Metallographie*, 34(8):417–429.
- [Chen et al., 2006] Chen, C.-Y., Chen, H.-L., and Hwang, W.-S. (2006). Influence of Interfacial Structure Development on the Fracture Mechanism and Bond Strength of Aluminum/Copper Bimetal Plate. *Materials Transactions*, 47(4):1232–1239.
- [Christ, 1991] Christ, H.-J. (1991). *Wechselverformung von Metallen*. Springer, Berlin Heidelberg.
- [Cline, 1966] Cline, C. (1966). An analytical and experimental study of diffusion bonding. *Welding Journal*, 45(11):481–489.
- [Coffin, 1954] Coffin, L. F. (1954). A study on the effects of cyclic thermal stresses on a ductile metal. *Transactions of the ASME*, 76.
- [Cohen et al., 1995] Cohen, I. M., Huang, L. J., and Ayyaswamy, P. (1995). Melting and solidification of thin wires: a class of phase-change problems with a mobile interface - II. Experimental confirmation. *International Journal of Heat Transfer*, 38(9):1647–1659.
- [Crandall et al., 1978] Crandall, S., Dahl, N., and Lardners, T. (1978). *Introduction to the Mechanics of Solids*. McGraw-Hill, Boston, 2nd edition.
- [Cremer et al., 2013] Cremer, M., Zimmermann, M., and Christ, H. J. (2013). High-frequency cyclic testing of welded aluminium alloy joints in the region of very high cycle fatigue (VHCF). *International Journal of Fatigue*, 57:120–130.
- [Dowling, 1999] Dowling, N. E. (1999). *Mechanical Behavior of Materials. Engineering methods for deformation, fracture, and fatigue*. Prentice-Hall Inc., 2nd edition.

- [Drozdov et al., 2008a] Drozdov, M., Gur, G., Atzmon, Z., and Kaplan, W. D. (2008a). Detailed investigation of ultrasonic Al–Cu wire-bonds: I. Intermetallic formation in the as-bonded state. *Journal of Materials Science*, 43(18):6029–6037.
- [Drozdov et al., 2008b] Drozdov, M., Gur, G., Atzmon, Z., and Kaplan, W. D. (2008b). Detailed investigation of ultrasonic Al–Cu wire-bonds: II. Microstructural evolution during annealing. *Journal of Materials Science*, 43(18):6038–6048.
- [Ellyin, 1997] Ellyin, F. (1997). *Fatigue Damage, Crack Growth and Life Prediction*. Chapman & Hall, London, 1st edition.
- [Ewing and Humfrey, 1903] Ewing, J. A. and Humfrey, J. C. (1903). The Fracture of Metals under Repeated Alternations of Stress. *Philosophical Transactions of the Royal Society of London. Series A, Containing Papers of a Mathematical or Physical Character*, 200:241–250.
- [Fatigue and Murakami, 2002] Fatigue, M. and Murakami, Y. (2002). *Metal Fatigue: Effects of Small Defects and Nonmetallic Inclusions*. Elsevier, Oxford, first edition.
- [Fenner, 1999] Fenner, R. T. (1999). *Mechanics of Solids*. CRC Press, Boca Raton.
- [Fouk, III et al., 2008] Fouk, III, J., Johnson, G., Klein, P., and Ritchie, R. (2008). On the toughening of brittle materials by grain bridging: Promoting intergranular fracture through grain angle, strength, and toughness. *Journal of the Mechanics and Physics of Solids*, 56(6):2381–2400.
- [Gottstein, 2014] Gottstein, G. (2014). *Materialwissenschaft und Werkstofftechnik-Physikalische Grundlagen*, volume 45. Springer, 4 edition.
- [Griffith, 1920] Griffith, A. A. (1920). The Phenomena of Rupture and Flow in Solids. *Philosophical Transactions, Series A*, 221:163–198.
- [Gross, 1996] Gross, D. (1996). *Bruchmechanik*. Springer, Berlin, 2nd edition.
- [Hang et al., 2009] Hang, C., Song, W., Lum, I., Mayer, M., Zhou, Y., Wang, C., Moon, J., and Persic, J. (2009). Effect of electronic flame off parameters on copper bonding wire: Free-air ball deformability, heat affected zone length, heat affected zone breaking force. *Microelectronic Engineering*, 86(10):2094–2103.

- [Hang et al., 2008] Hang, C. J., Wang, C. Q., Mayer, M., Tian, Y. H., Zhou, Y., and Wang, H. H. (2008). Growth behavior of Cu/Al intermetallic compounds and cracks in copper ball bonds during isothermal aging. *Microelectronics Reliability*, 48:416–424.
- [Harman, 2010] Harman, G. (2010). *Wire Bonding in Microelectronics*. McGraw-Hill, third edition.
- [Höppel et al., 2010] Höppel, H. W., Prell, M., May, L., and Göken, M. (2010). Influence of grain size and precipitates on the fatigue lives and deformation mechanisms in the VHCF-regime. *Procedia Engineering*, 2(1):1025–1034.
- [Hosseinian and Pierron, 2013] Hosseinian, E. and Pierron, O. (2013). Quantitative in situ TEM fatigue testing on nanocrystalline metallic ultrathin films. *Nanoscale*, 5(24):12532–12541.
- [Huang et al., 1995] Huang, L. J., Ayyaswamy, P., and Cohen, I. M. (1995). Melting and solidification of thin wires: a class of phase-change problems with a mobile interface - I. Analysis. *International Journal of Heat Transfer*, 38(9):1637–1645.
- [Hull et al., 2011] Hull, D., Bacon, J., Materials, C., Slip, C. O. F., Dislocations, P., Metals, P., Gb, S., Deformation, P., and Bacon, D. (2011). *Introduction to Dislocations*, volume 1. Elsevier, Oxford, 5th edition.
- [Inglis, 1913] Inglis, C. E. (1913). Stresses in a Plate Due to the Presence of Cracks and Sharp Corners. *Transactions of the Institute of Naval Architects*, 55:216–241.
- [Irwin, 1956] Irwin, G. R. (1956). Onset of Fast Crack Propagation in High Strength Steels and Aluminum Alloys. In *Sagamore Research Conference Proceedings, Vol. 2*, pages 289–305.
- [JEDEC, 2009] JEDEC (2009). Wire Bond Shear Test Method EIA/JESD22-B16.
- [Johnson and Paris, 1968] Johnson, H. H. and Paris, P. C. (1968). Sub-critical flaw growth. *Engineering Fracture Mechanics*, 1(1):3–45.
- [Kazakov, 1985] Kazakov, N. F. (1985). *Diffusion Bonding of Materials*. Pergamon Press, New York.

- [Khatibi et al., 2010] Khatibi, G., Lederer, M., Weiss, B., Licht, T., Bernardi, J., and Danninger, H. (2010). Accelerated mechanical fatigue testing and lifetime of interconnects in microelectronics. *Procedia Engineering*, 2(1):511–519.
- [Khatibi et al., 2008] Khatibi, G., Wroczewski, W., Weiss, B., and Licht, T. (2008). A fast mechanical test technique for life time estimation of micro-joints. *Microelectronics Reliability*, 48(11-12):1822–1830.
- [Koberna and Fiala, 1993] Koberna, M. and Fiala, J. (1993). Intermetallic Phases Influencing the Behavior of Al-Cu Joints. *Journal of Physics and Chemistry of Solids*, 54(5):595–601.
- [Kouters et al., 2013] Kouters, M., Gubbels, G., and Dos Santos Ferreira, O. (2013). Characterization of intermetallic compounds in Cu–Al ball bonds: Mechanical properties, interface delamination and thermal conductivity. *Microelectronics Reliability*, 53(8):1068–1075.
- [Kouters et al., 2011] Kouters, M. H. M., Gubbels, G. H. M., O’Halloran, O., Rongen, R., and Weltevreden, E. R. (2011). Mechanical properties of intermetallics formed during thermal aging of Cu-Al ball bonds. In *2011 12th Int. Conf. on Thermal, Mechanical and Multi-Physics Simulation and Experiments in Microelectronics and Microsystems, EuroSimE 2011*, pages 11–13.
- [Kraft et al., 2010] Kraft, O., Gruber, P. a., Mönig, R., and Weygand, D. (2010). Plasticity in Confined Dimensions. *Annual Review of Materials Research*, 40(1):293–317.
- [Lassnig et al., 2015] Lassnig, A., Pelzer, R., Gammer, C., and Khatibi, G. (2015). Role of intermetallics on the mechanical fatigue behavior of Cu-Al ball bond interfaces. *Journal of alloys and compounds*.
- [Lassnig et al., 2012] Lassnig, A., Pelzer, R., Khatibi, G., Weiss, B., and Nelhiebel, M. (2012). Accelerated lifetime measurements of Cu-Al ball bonded interconnects. In *2012 13th International Thermal, Mechanical and Multi-Physics Simulation and Experiments in Microelectronics and Microsystems, EuroSimE 2012*.
- [Lassnig et al., 2013] Lassnig, A., Trasischker, W., Khatibi, G., Weiss, B., Nelhiebel, M., and Pelzer, R. (2013). Accelerated lifetime estimation of thermosonic Cu ball bonds on Al metallization. *Microelectronic Engineering*, 106:188–194.

- [Lederer et al., 2015] Lederer, M., Lassnig, A., Khatibi, G., and Delshadmanesh, M. (2015). Reliability assessment of copper ball bonds by combination of simulation and accelerated mechanical testing. In *2015 16th International Thermal, Mechanical and Multi-Physics Simulation and Experiments in Microelectronics and Microsystems, EuroSimE 2015*, number 3, pages 1–8.
- [Lee and Kwon, 2013] Lee, K. S. and Kwon, Y. N. (2013). Solid-state bonding between Al and Cu by vacuum hot pressing. *Transactions of Nonferrous Metals Society of China (English Edition)*, 23(2):341–346.
- [Lee et al., 2005] Lee, W.-B., Bang, K.-S., and Jung, S.-B. (2005). Effects of inter-metallic compound on the electrical and mechanical properties of friction welded Cu/Al bimetallic joints during annealing. *Journal of Alloys and Compounds*, 390(1-2):212–219.
- [Legros, 2014] Legros, M. (2014). In situ mechanical TEM: Seeing and measuring under stress with electrons. *Comptes Rendus Physique*, 15(2-3):224–240.
- [Li et al., 2009] Li, B., Reis, L., and de Freitas, M. (2009). Comparative study of multiaxial fatigue damage models for ductile structural steels and brittle materials. *International Journal of Fatigue*, 31(11-12):1895–1906.
- [Li et al., 2006] Li, M., Li, S., and Ji, H. (2006). Metallurgical Behavior of Au/Al Bond Interface during High Temperature Storage of Ultrasonic Wedge Bonding. *2006 7th International Conference on Electronic Packaging Technology*, pages 1–4.
- [Magnien and Khatibi, 2014] Magnien, J. and Khatibi, G. (2014). Assessment of mechanical reliability of surface mounted capacitor by an accelerated shear fatigue test technique. *Microelectronics Reliability*, 54(9-10):1764–1769.
- [Manson, 1954] Manson, S. S. (1954). Behavior of materials under conditions of thermal stress. *NACA report 1170 National Advisory Committee for Aeronautics*, pages 1–37.
- [Mason, 1956] Mason, W. P. (1956). Internal Friction and Fatigue in Metals at Large Strain Amplitudes. *Journal of Acoustical Society of America*, 28(6):1207–1218.

- [Mayer, 2006] Mayer, H. (2006). Ultrasonic torsion and tension-compression fatigue testing: Measuring principles and investigations on 2024-T351 aluminium alloy. *International Journal of Fatigue*, 28(11):1446–1455.
- [Murali et al., 2004] Murali, S., Srikanth, N., and Vath, C. J. (2004). Effect of wire size on the formation of intermetallics and Kirkendall voids on thermal aging of thermosonic wire bonds. *Materials Letters*, 58(25):3096–3101.
- [Murray, 1985] Murray, J. L. (1985). The aluminium-copper system. *International Metals Reviews*, 30(5):211–233.
- [Orhan et al., 1999] Orhan, N., Aksoy, M., and Eroglu, M. (1999). A new model for diffusion bonding and its application to duplex alloys. *Materials Science and Engineering: A*, 271(1-2):458–468.
- [Otsuka et al., 1980] Otsuka, A., Mori, K., and Ohshima, T. (1980). Fatigue crack growth of steel and aluminum alloy specimens under mode II loading. *Zairyo*, 29:1042.
- [Paris and Erdogan, 1963] Paris, P. and Erdogan, F. (1963). A critical analysis of crack propagation laws. *Journal of Basic Engineering, Trans. ASME, Series D*, 85:528–534.
- [Pelzer et al., 2012] Pelzer, R., Nelhiebel, M., Zink, R., Woehlert, S., Lassnig, A., and Khatibi, G. (2012). High temperature storage reliability investigation of the Al–Cu wire bond interface. *Microelectronics Reliability*, 52(9-10):1966–1970.
- [Philofsky, 1970] Philofsky, E. (1970). Intermetallic Formation in Gold-Aluminum Systems. *Solid-State Electronics*, 13:1391–1399.
- [Phung et al., 2013] Phung, N.-l., Marti, N., Blanche, A., Ranc, N., Saintier, N., Gr, F., Thoquenne, G., Phung, N.-l., Marti, N., Blanche, A., Ranc, N., Phung, N. L., Marti, N., Blanche, A., Ranc, N., Chrysochoos, A., Saintier, N., Grégori, F., and Bacroix, B. (2013). Very High Cycle Fatigue for single phase ductile materials : slip band appearance criterion. In *5th Fatigue Design Conference*.
- [Pilkey and Pilkey, 2008] Pilkey, W. D. and Pilkey, D. F. (2008). *Peterson’s Stress Concentration Factors*. John Wiley & Sons, New York, 3rd edition.

- [Pippan et al., 2011] Pippan, R., Zelger, C., Gach, E., Bichler, C., and Weinhandl, H. (2011). On the mechanism of fatigue crack propagation in ductile metallic materials. *Fatigue & Fracture of Engineering Materials & Structures*, 34(1):1–16.
- [Pook, 2007] Pook, L. (2007). *Metal Fatigue - What it is, why it matters*. Springer.
- [Qin et al., 2011] Qin, I., Shah, a., Huynh, C., Meyer, M., Mayer, M., and Zhou, Y. (2011). Role of process parameters on bondability and pad damage indicators in copper ball bonding. *Microelectronics Reliability*, 51(1):60–66.
- [Rabkin et al., 1970] Rabkin, D. M., Ryabov, V. R., Lozovskaya, A. V., and Dovzhenko, V. A. (1970). Preparation and Properties of Copper-Aluminum Intermetallic Compounds. *Poroshkovaya Metallugiya*, 8(92):101–107.
- [Rankine, 1857] Rankine, W. J. M. (1857). On the Stability of Loose Earth. *Philosophical Transactions of the Royal Society of London*, 147:9–27.
- [Ritchie, 1977] Ritchie, R. (1977). Influence of microstructure on near-threshold fatigue crack propagation in ultra-high strength steel. *Metal Science*, 11:368–381.
- [Ritchie, 1999] Ritchie, R. (1999). Mechanisms of fatigue-crack propagation in ductile and brittle solids. *International Journal of Fracture*, 100:55–83.
- [Ritchie et al., 2000] Ritchie, R., Gilbert, C., and McNaney, J. (2000). Mechanics and mechanisms of fatigue damage and crack growth in advanced materials. *International Journal of Solids and Structures*, 37(1-2):311–329.
- [Ritchie, 1988] Ritchie, R. O. (1988). Mechanisms of fatigue crack propagation in metals, ceramics and composites: role of crack tip shielding. *Materials Science and Engineering: A*, 103:15–28.
- [Ritchie and Dauskardt, 1991] Ritchie, R. O. and Dauskardt, R. (1991). Cyclic Fatigue of Ceramics A Fracture Mechanics Approach to Subcritical Crack Growth and Life Prediction. *Journal of the Ceramic Society of Japan*, 99:1047–1062.
- [Roth, 1985] Roth, L. D. (1985). *Ultrasonic Fatigue Testing*, volume 8. Ohio ASM.
- [Saksala, 2010] Saksala, T. (2010). Damage-viscoplastic consistency model with a parabolic cap for rocks with brittle and ductile behavior under low-velocity

- impact loading. *International Journal for Numerical and Analytical Methods in Geomechanics*, 34(13):1362–1386.
- [Schneider-Ramelow et al., 2013] Schneider-Ramelow, M., Geißler, U., Schmitz, S., Grübl, W., and Schuch, B. (2013). Development and Status of Cu Ball/Wedge Bonding in 2012. *Journal of Electronic Materials*, 42(3):558–595.
- [Stanzl-Tschegg and Schönbauer, 2010] Stanzl-Tschegg, S. E. and Schönbauer, B. (2010). Mechanisms of strain localization, crack initiation and fracture of polycrystalline copper in the VHCF regime. *International Journal of Fatigue*, 32(6):886–893.
- [Stickler and Weiss, 1982] Stickler, R. and Weiss, B. (1982). *Review of the application of ultrasonic fatigue test methods for the determination of crack growth and threshold behavior of metallic materials*, *Ultrasonic Fatigue*. The Metallurgical Society of AIME.
- [Suresh, 1991] Suresh, S. (1991). *Fatigue of materials*. Cambridge University Press, Cambridge, 1st edition.
- [Takeuchi et al., 1973] Takeuchi, T., Ikeda, S., Ikeno, S., and Furubayashi, E.-i. (1973). A Specimen Stage for Low Temperature Tensile Deformation in an Electron Microscope. *Japanese Journal of Applied Physics*, 12(1):142–145.
- [Tanaka et al., 1984] Tanaka, K., Matsuoka, S., and Kimura, M. (1984). Fatigue Strength of 7075-T6 Aluminum Alloy Under Combined Axial Loading and Torsion. *Fatigue and Fracture of Engineering Materials and Structures*, 7(3):195–211.
- [Tresca, 1864] Tresca, H. (1864). Mémoire sur l’écoulement des corps solides soumis à de fortes pressions. *Comptes rendus hebdomadaires des séances de l’Académie des sciences*, 59(2):754–758.
- [Völker et al., 2015] Völker, B., Venkatesan, S., Heinz, W., Matoy, K., Roth, R., Batke, J.-M., Cordill, M. J., and Dehm, G. (2015). Following crack path selection in multifilm structures with weak and strong interfaces by in situ 4-point-bending. *Journal of Materials Research*, 30(08):1090–1097.

- [von Mises, 1913] von Mises, R. (1913). Mechanik der festen Koerper im plastisch deformablen Zustand. *Nachrichten von der königlichen Gesellschaft der Wissenschaften zu Göttingen*, 1:582–592.
- [Walter et al., 2015] Walter, T., Khatibi, G., Nelhiebel, M., Heinz, W., and Robl, W. (2015). High cycle fatigue properties of Cu films. *Microelectronic Engineering*, 137:64–69.
- [Wegst et al., 2015] Wegst, U. G. K., Bai, H., Saiz, E., Tomsia, A. P., and Ritchie, R. O. (2015). Bioinspired structural materials. *Nature materials*, 14(February):23–36.
- [Woehler, 1870] Woehler, A. (1870). Über die Festigkeitsversuche mit Eisen und Stahl. *Zeitschrift fuer Bauwesen*, 20:73–106.
- [Wu and Lo, 2002] Wu, Y. and Lo, Y. (2002). Surface protection for AA8090 aluminum alloy by diffusion bonding. *Theoretical and Applied Fracture Mechanics*, 38(1):71–79.
- [Wulff et al., 2007] Wulff, F., Tok, C., and Breach, C. (2007). Oxidation of Au4Al in gold ballbonds. *Materials Letters*, 61(2):452–456.
- [Xu et al., 2011a] Xu, H., Liu, C., Silberschmidt, V., Chen, Z., Wei, J., and Sivakumar, M. (2011a). Effect of bonding duration and substrate temperature in copper ball bonding on aluminium pads: A TEM study of interfacial evolution. *Microelectronics Reliability*, 51(1):113–118.
- [Xu et al., 2011b] Xu, H., Liu, C., Silberschmidt, V., Pramana, S., White, T., Chen, Z., and Acoff, V. (2011b). Behavior of aluminum oxide, intermetallics and voids in Cu–Al wire bonds. *Acta Materialia*, 59(14):5661–5673.
- [Xu et al., 2010] Xu, H., Liu, C., Silberschmidt, V. V., Pramana, S. S., White, T. J., Chen, Z., Sivakumar, M., and Acoff, V. L. (2010). A micromechanism study of thermosonic gold wire bonding on aluminum pad. *Journal of Applied Physics*, 108(11):1–8.
- [Yu et al., 2015] Yu, Q., Legros, M., and a.M. Minor (2015). In situ TEM nanomechanics. *MRS Bulletin*, 40(01):62–70.

- [Zhong et al., 2006] Zhong, Y., Xiao, F., Zhang, J., Shan, Y., Wang, W., and Yang, K. (2006). In situ TEM study of the effect of M/A films at grain boundaries on crack propagation in an ultra-fine acicular ferrite pipeline steel. *Acta Materialia*, 54(2):435–443.
- [Zimmermann et al., 2014] Zimmermann, M., Bretschneider, J., Kirchhoff, G., Stamm, U., Standfuss, J., and Brenner, B. (2014). Fatigue Behaviour of Laser Beam Welded Circular Weld Seams under Multi-Axial Loading. *Advanced Materials Research*, 891-892:1397–1402.
- [Zuruzi et al., 1999] Zuruzi, A., Li, H., and Dong, G. (1999). Effects of surface roughness on the diffusion bonding of Al alloy 6061 in air. *Materials Science and Engineering: A*, 270(2):244–248.

Alice Lassnig

Curriculum Vitæ

✉ alice.lassnig@univie.ac.at

Personal Information

Date of birth 13th September, 1986
Birthplace Poitiers, France
Nationality Austria and France
Marital status Single

Education

04/2011 – now PhD Candidate at the Faculty of Physics, Group of Physics of Nanostructured Materials, University of Vienna, Austria
Topic: “Fatigue investigations of miniaturized and bulk Al-Cu interfaces”
Advisors: Dr. Golta Khatibi & Prof. Michael Zehetbauer

09/2013 – Visiting PhD student at the University of California, Santa Barbara, USA at the
09/2014 Materials Department, Pollock Group
Advisor: Prof. Tresa M. Pollock

10/2005 – Diploma studies of Physics at the University of Vienna, Austria
02/2011 Diploma examination with distinction
Degree awarded: Mag. rer. nat.

02/2010 – Diploma thesis in cooperation with industrial partners Infineon Villach, Austria
02/2011 Title: "Beschleunigte Lebensdaueruntersuchung miniaturisierter Materialverbindungen (=Accelerated lifetime investigation of miniaturized material interconnects)"
Advisors: Dr. Golta Khatibi & Prof. Viktor Gröger.

09/2008 – Physics studies abroad at the Universidad Autónoma de Madrid, Spain
06/2009

09/1996 – High school (Akademisches Gymnasium Linz, Austria)
06/2004 final exam – Matura – with distinction

Prizes and Scholarships

2013 Marietta Blau scholarship awarded by the Austrian Federal Ministry of Science and Research for research year abroad at UCSB

2012 Merit-based scholarship for excellent studies in the academic year of 2010/2011

2011 Merit-based scholarship for excellent studies in the academic year of 2009/2010

2008/2009 Erasmus scholarship for studies abroad

2008/2009 Refund of enrollment fees by the company VOEST Alpine Linz for the academic year of 2008/2009 due to excellent engagement during the summer internship

Professional History

- 05/2011–
present University assistant at the University of Vienna, Austria
active in the group of Physics of Nanostructured Materials
Duties: research in the field of applied materials physics, project collaboration, teaching activities, publishing and writing PhD thesis
- 08/2008, Summer internships at voestalpine Linz, Austria
07/2007, internship duties depending on period of appointment: administration of juridical
08/2005, decisions via SAP, evaluation of ternary phase diagrams in the research department,
07/2003 assistance at the secretary office

List of Publications

- 7 Lassnig, A., Torbet, C., Pollock, T., Khatibi, G., Zehetbauer, M. (2015) High cycle fatigue investigations of bulk Al-Cu diffusion bonds. Manuscript under preparation.
- 6 Lassnig, A., Pelzer, R., Gammer, C., Khatibi, G. (2015) Role of intermetallics on the mechanical fatigue behavior of Cu-Al ball bond interfaces. Journal of Alloys and Compounds. Article in Press
- 5 Lederer, M., Lassnig, A., Khatibi, G., Delshadmanesh, M. (2015) Reliability assessment of copper ball bonds by combination of simulation and accelerated mechanical testing. 16th International Thermal, Mechanical and Multi-Physics Simulation and Experiments in Microelectronics and Microsystems, EuroSimE 2012.
- 4 Lassnig, A., Trasischker, W., Khatibi, G., Weiss, B., Pelzer, R., Nelhiebel, M. (2013) Accelerated lifetime estimation of thermosonic Cu ball bonds on Al metallization. Microelectronic Engineering. Accepted
- 3 Pelzer, R., Nelhiebel, M., Zink, R., Wöhlert, S., Lassnig, A., Khatibi, G. High temperature storage reliability investigation of the Al-Cu wire bond interface. Microelectronics Reliability, 52(9-10), 1966-1970.
- 2 Lassnig, A., Pelzer, R., Khatibi, G., Weiss, B., Nelhiebel, M. (2012). Accelerated lifetime measurements of Cu-Al ball bonded interconnects. 2012 13th International Thermal, Mechanical and Multi-Physics Simulation and Experiments in Microelectronics and Microsystems, EuroSimE 2012.
- 1 Trasischker, W., Lassnig, A., Khatibi, G., Weiss, B., Nelhiebel, M., Pelzer, R. (2011). Lifetime of thermosonic copper ball bonds on aluminum metallization pads. 2011 IEEE International Interconnect Technology Conference and 2011 Materials for Advanced Metallization, IITC/MAM 2011.

Invention Disclosure

- 1 Pelzer, R., Nelhiebel, M., Khatibi, G., Lassnig, A., Czerny, B. (2013), Invention Disclosure: Test method for nailhead wire bonds utilizing a macroscopic handle

Talks at international conferences

- 03/2015 Lassnig, A., Khatibi, G., Torbet, C., Pollock, T., Zehetbauer, M., High cycle fatigue properties of Al-Cu interfaces. 26th Colloquium on Fatigue Mechanisms in Brno, Czech Republic.
- 02/2014 Lassnig, A., Torbet, C., Khatibi, G., Zehetbauer, M., Pollock T., Role of Inter-metallics on Mechanical Properties of Al-Cu Interfaces.TMS Annual Meeting and Exhibition in San Diego, USA.
- 09/2013 Lassnig, A., Khatibi, G., Zehetbauer, M. Effect of intermetallic phases on mechanical properties of Al-Cu interfaces. European Congress and Exhibition on Advanced Materials and Processes (EUROMAT) 2013 in Sevilla, Spain.
- 04/2013 Lassnig, A., Khatibi, G., Weiss, B., Zehetbauer, M., Pelzer, R., Nelhiebel, M. Effect of Intermetallic Compound Formation on Crack Path Morphologies in Al-Cu Interfaces. 24th Colloquium on Fatigue Mechanisms in Freiberg, Germany.
- 10/2012 Pelzer, R., Nelhiebel, M., Zink, R., Woehlert, S., Lassnig, A., Khatibi, G. High temperature storage reliability investigation of the Al-Cu bond interface. 23rd European Symposium on Reliability of Electron Devices, Failure Physics and Analysis in Cagliari, Italy.
- 04/2012 Lassnig, A., Khatibi, G., Weiss, B., Zehetbauer, M., Pelzer, R., Nelhiebel, M. Influence of high temperature storage on lifetime of Cu-Al interconnects. 23rd Colloquium on Fatigue Mechanisms in Poitiers, France.

Poster presentations at international conferences

- 04/2012 Lassnig, A., Pelzer, R., Khatibi, G., Weiss, B., Nelhiebel M., Zehetbauer, M. Accelerated lifetime measurements of Cu-Al ball bonded interconnects. 13th EuroSimE Conference in Cascais, Portugal.
- 05/2011 Lassnig, A., Trasischker, W., Khatibi G., Weiss, B., Nelhiebel M., Pelzer, R. Lifetime of thermosonic copper ball bonds on aluminum metallization pads. 14th IITC Conference in Dresden, Germany.

Teaching and Mentoring Experience

- 2012/2013 and 2014/2015 Physics laboratory I and II – for physics diploma students in their second year
- 2007/2008 and 2010/2011 Tutorial for women in physics

Language skills

- German native
- French native
- English fluent
- Spanish proficient

